The effects of atmosphere conditions on gamma-ray astronomy

Aye, Klaus-Michael

The Effects of Atmosphere Conditions on Gamma-Ray Astronomy

by

Klaus-Michael Aye

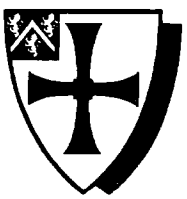

Submitted in conformity with the requirements
for the degree of Doctor of Philosophy

Department of Physics
University of Durham
South Road
Durham. UK.

Abstract

The High Energetic Stereoscopic System (H.E.S.S.) experiment is an array of imaging atmospheric Cherenkov (IAC) telescopes of the next generation, with enlarged mirrors and advanced detector electronics compared to its predecessors. As a member of the international H.E.S.S. collaboration, the Durham γ-ray astronomy group took over the responsibility for design, construction and commisioning of calibration systems for the H.E.S.S. telescopes and atmospheric monitoring devices.

The atmosphere is an essential part of the detector system for the IAC technique, monitoring of the atmosphere's parameter is therefore important for energy calibration of the detector and variability studies of γ-ray sources to distinguish between detector and source fluctuations. A weatherstation, several infrared radiometers and an infrared LIDAR system have been installed to provide constant monitoring of all relevant parameters. This thesis reports about the work performed for the design and commissioning of the calibration module. Furthermore, the technicalities of the LIDAR system and the IR radiometer, their use in terms of γ-ray astronomy, especially studies about the variability of zenith angle dependencies and the correlation with other atmospheric parameters and telescope trigger rates are discussed.

Acknowledgements

Many people have supported me in all kinds of ways during my studies over the last four years. I first have to thank my supervisors Dr. Paula M. Chadwick and Dr. T. J. L. McComb for their endless support and trust in my abilities, my thesis has basically been proofread by these two kind people, a service that not every Ph.D. student receives like that. I also have to thank my supervisors for letting me go my own directions in many ways, a freedom again not shared by many fellow Ph.D. students at any university. Generelly I am very happy to have touched down in this little group of friendly scientists that created a very nice working environment for me, even if I had a hard time to proof that Germans do have a sense of humour. Thank you again for four years in my life that I certainly will not forget.

What follows is a list of fellows I want to thank especially: Dr. John Osborne for sharing his deep insights in all matters of atmosphere and simulations. The same is true for Dr. Sam Nolan, who in parallel taught me one thing or two about english humor which was most appreciated as well. Dr. Joy McKenny I want to thank for her endless amount of friendlyness and all the time she spends on giving a hand to help others. And for showing me that even in the most evil looking wrong-doing somewhere inside one might find some good intentions that maybe just went the wrong way. Aristeidis Noutsos was always eager to discuss some scientific news so I am very thankful to have spent a lot of time inside and outside the office with him, celebrating 'sound sample' days and other important things. This appreciation we shared with our office mate — the third big G — Ian Latham, who I thank very much for his helpful hands and insights into north-east politics and language. Dr. Michael Daniel should not be forgotten as probably the man who knows more about my thesis than me, always on the brink to de-construct any ideas I had concerning atmospheric stuff, and thereby with his constructive criticism often helping me on the right path. My thanks also go to Christos Hadjichristidis, who was always there to give me lifts to and from Cafe Nero and have a lot of nice chats in there. Cafe Nero, a nice coffee place in Durham, has in a way contributed a lot to the advance of my thesis, so I am thankful for its existence. And last but not least Julie, because without seeing her eyes, I never would have touched down in Durham.

This thesis has been made possible by the provision of the facilities of the Physics Department at the University of Durham and the research studentship of the University of Durham.

Dedication

To my parents, whose everlasting trust and support in my abilities have made all this possible. Thanks for letting me follow my own ways ...

Declaration

The material contained within this thesis has not previously been submitted for a degree at the University of Durham or any other university. The research reported within this thesis has been conducted by the author unless indicated otherwise.

Copyright Notice

Contents

Introduction

In the recent years γ-ray astronomy has been established as a new astronomical window into the sky and in particular an useful tool to observe high energy phenomena in the universe. This has been achieved by combining the mere 'counting' experiments of classical high energy cosmic-ray detectors with the traditional imaging approach of observational astronomy. This successful combination gave not only birth to a new breed of astronomers, coming from high energy experiments, but also for the first time it provided clues about the origins of this high energy radiation.

The High Energetic Stereoscopic System (H.E.S.S.) experiment can be considered as the logical and consequent evolution of its direct predecessor, the High Energy Gamma-Ray Astrophysics experiment HEGRA on La Palma. HEGRA demonstrated first the superior efficiency of the stereoscopic technique for the observation of air showers by using an array of imaging Cherenkov telescopes. HEGRA in turn naturally was motivated by many earlier successful γ-ray experiments among which the Durham Mark experiments were pioneering.

As the atmosphere is a crucial part of the detector in γ-ray astronomy, careful monitoring of its parameters is needed for

- interpreting any time dependencies in the observed data and
- calibrating the camera to translate the observed Cherenkov light to the energy of the primary γ-ray photon.

To develop hardware tools for calibration purposes and atmospheric monitoring defines the tasks of the University of Durham's γ-ray astronomy group as a member of the international H.E.S.S. collaboration.

This thesis shall describe the author's involvement in hardware development for the calibration of the high-speed camera of H.E.S.S., the evaluation and commissioning of weather monitoring devices including software development for introduction

of these devices into the main data-acquisiton system of H.E.S.S.. Considerable effort has been spent on creating a software framework for the monitoring devices that can be used effortlessly by collaborators.

In the first chapters I would like to review the basics of the physics needed to follow this thesis. Chapter 1 first gives a brief introduction into the historical development of this new source of astronomical information, followed by a quick overview of potential astronomical sources of this radiation.

Chapter 2 reviews the technique of imaging atmospheric Cherenkov astronomy and lists the most important experiments of the past, followed by a more detailed chapter 3 concerning the H.E.S.S. experiment.

After these introductional chapters, preparational work towards the calibration module for the first H.E.S.S. telescope is described in chapter 4.

This is followed by a summarizing chapter 5, listing all atmospheric monitoring devices the Durham group has installed at the H.E.S.S. observatory site in Namibia, including studies of the zenith angle variability of IR zenith angle dependencies measured with a scanning radiometer.

Chapter 6 then goes into detail of the LIDAR system that has been installed at the observatory, followed by the chapter 7 which shows finally how the data of our monitoring can be used to learn something about the correlations of observational parameters.

Concluding I will discuss the outcomes of this thesis with an outlook into the future.

Chapter 1

Cosmic Rays

In this chapter the nature of cosmic rays and the basic underlying physics of the sources will be discussed. This review is, of its nature, brief and merely provides the reader with a glance of the whole field in order to see this work in context. The structure of this introductory chapter is a very practical one. I will give first a short historical overview of the beginnings of gamma-ray astronomy. Section 1.2 then talks about the special case of cosmic radiation as the source of these γ-rays, followed by sections on what physical processes can create γ-rays, in what kind of astronomical sources these processes can occur, and how these γ-rays can be absorbed again on their way to the observer.

Interested readers are directed to the works of Longair [1992, 1994], overviews of γ-ray-sources and related physics have often been inspired by the book of Weekes [2003]. An excellent summary of the early history of γ-ray astronomy can be found in the review of Weekes [1988]. Further references to other important works are contained within the review.

1.1 History

The concept of γ-ray-astronomy was first raised in the 1958 seminal paper of Morrison [1958]. Firstly only envisioned as a means to explain the nature of energetic radio sources, the combination of high-energy electrons and intense magnetic fields not only postulated synchrotron emission but also high-energy protons, high energy neutral π mesons, and γ-rays. One year later, Cocconi [1960] suggested the existence of TeV γ-rays from the Crab Nebula, together with the hypothesis that these could be observed by ground-based air shower detectors. Throughout the 1960s and

into the 1970s then, a number of atmospheric Cherenkov telescopes and air shower arrays operated at various sites around the world. But despite initial high hopes of easy successes, it had inherent difficulties. For the case of ground based TeV γ-ray astronomy, unlike in experimental astrophysics at other regions of the electromagnetic spectrum it is rather convoluted in the sense that the primary photon is never captured by any detector. By using the indirect observation technique of atmospheric showers, it is impossible, unlike at all other wavelengths used in astronomy (even in X-ray astronomy), to deflect and concentrate the primaries to increase the signal-to-noise ratio and thereby the sensitivity towards the very small flux of γ-rays. [1]

Additionally, the detection of γ-rays has to be achieved against a generally overwhelming background of hadronic cascades with a flux factor 1000 larger, so it becomes apparent that beam concentration is particularly important as the background will always scale with the detector area in this case. These inherent difficulties of γ-ray astronomy caused on the one hand a long delay in the initial rapid success that had been predicted and on the other hand led eventually to the situation that γ-ray astronomy became a highly active field for the application of new statistical theories and methods; many conferences in the early times of γ-ray astronomy were dominated by discussions about the statistical significances of 'detected' γ-ray signals. It then had been realized early on that if TeV γ-ray astronomy is to be viable and generate a catalogue of astronomical objects that have been confirmed statistically with high significance, then it has to be capable of rejecting this unwanted hadronic background at 'some remarkably high level of efficiency, while simultanously retaining a majority of the genuine γ-ray events' [Fegan, 1997].

After an, albeit statistically not thoroughly convincing, detection of the Crab Nebula in the 1960s, the 1970s SAS-2 and COS-B satellite experiments made the first significant high-energy gamma-ray detections in the energy range of 35 MeV to 5 GeV, detecting a diffuse γ-ray flux concentrated in the galactic plane and an isotropic extragalactic gamma-radiation. In 1979, the Crimean Observatory reported evidence for VHE γ-ray emission from Cygnus X-3 using the atmospheric technique [Neshpor et al., 1979]. By 1985 it was generally acknowledged that ground-based γ-ray astronomy had entered into an exciting period of discovery (see [Ong, 1998] and references therein). This was followed by some time where earlier detections could not

[1] At energies above 100 MeV for example, the strongest known source, the Vela pulsar, emits a flux of only 1 photon per minute in satellite telescopes flown to date [Weekes, 2003].

be reproduced, but eventually in the 1990s the situation changed again, and solid source detections emerged (see section 1.8); among them the most useful detection was the Crab Nebula, that has been established as a steady standard candle source of γ-rays for the northern hemisphere.

The techniques of gamma-ray astronomy will be discussed in chapter 2; for now the nature and sources of cosmic rays are briefly described.

1.2 Cosmic radiation

Cosmic radiation (or *cosmic rays*, CR) reaches the earth nearly isotropically. Its average intensity is very constant in time, and its energy density of about 1 eV cm^{-3} is comparable to that in the galactic magnetic field, the cosmic background radiation, the starlight photons inside the galaxy or the turbulent gas motions of the interstellar medium. CR consist of several components in the following aproximate abundances:

- 85% protons,
- 14% α-particles,
- a few of heavy nucleons between Li and Fe,
- less than 1% leptons and
- ca. 0.1% γ-rays.

Following Murphy's law that the most interesting point in any collection of things shall be the one hardest to get a grip of, it is the last item of the list with its low percentage that is the most interesting from an astronomical point of view, because of the electrical neutrality of γ-rays and the ability to do astronomy with them.

When the so called 'primary' CR from outer space hits the earth's atmosphere, it reacts with the atmosphere's molecules and these interactions create the 'secondary' CR. The CR flux at the earth's surface is about 1000 particles $s^{-1}m^{-2}$. Most of the CR are moving relativistically, i.e. their energies are comparable to or larger than their masses, up to several 10^{20} eV.

The fundamental questions as yet inconclusively answered are the origin and acceleration mechanisms of the cosmic radiation. What seems to be certain, though, is that there is not a single source for the CR we receive on earth but a mix of different astrophysical situations where very high energy cosmic rays can be generated.

Energy Range	Classification	Detection Technique
~0.5 – 5 MeV	Low Energy (LE)	Scintillation Detector (Satellite)
5 – 30 MeV	Medium Energy (ME)	Compton Telescope (Satellite)
0.03 – 30 GeV	High Energy (HE)	Spark Chamber (Satellite)
0.01 – 50 TeV	Very High Energy (VHE)	Atmospheric Cherenkov Detector (Ground)
0.05 – 0.1 PeV	Ultra High Energy (UHE)	Scintillation Detector Array (Ground)
> 0.1 PeV	Extremely High Energy (EHE)	Scintillation Detector Array (Ground)

Table 1.1: Table indicating the energy ranges of γ-rays and their different detection techniques.

Sources are located on all kinds of astronomical distance scales; from within our own solar system up to inside distant galaxies with a distance measured in terms of their red-shift; this distance is also often described as being on a *cosmological distance scale.*

1.3 Spectrum of gamma-rays

The term γ-ray is quite a generic term and generally describes photons with energies higher than those of X-rays that e.g. can be created in cathode ray tubes such as those used by Röntgen in 1895 for the discovery of X-rays. Early predictions put an upper limit to the energy of γ-rays around 100 MeV, but today we have evidence of γ-rays with an energy up to one million times higher. This makes the energy range of γ-rays as large as all other observed wavelengths of electromagnetic waves, but a subclassification automatically developed from the different detection technologies required for such a huge energy range. Some authors place the lowest energies of γ-rays to 100 keV, but many others prefer the more natural boundary of 511 keV as the rest mass energy of an electron, with some placing it even at 1.02 MeV, as this is the limit for production of an electron-positron pair (see later) from a γ-ray.

To simplify matters, a nomenclature was eventually introduced that put γ-rays into several classes as can be seen in table 1.1.

At energies up to the 'high energy' range, γ-rays do not enter the atmosphere to any great depth, as their energy is quickly dispersed in electromagnetic cascades at the outer boundaries of the atmosphere. Thus satellites are used for the observations in this energy range. At very high energies larger than $\sim$ 30 GeV the γ-rays penetrate deeper into the atmosphere, so that their cascades have sufficient energy to create an appreciable amount of Cherenkov radiation (see chapter 2); this light is used to infer the energies and trajectories of the primary particles that hit the atmosphere, which is the basis for this thesis. At even higher energies, beginning from the ultra high

energy range, the primaries have enough energy to initiate cascades low enough in the atmosphere that ground-based scintillation arrays can detect directly particles of the cascades to reconstruct the primary's energy and trajectory.

1.4 Thermal vs. Non-thermal radiation

The appearance of the spectra of measured electro-magnetic radiation can be subdivided into three classes:

- spectral lines at specific frequencies characteristic of the emitting substance, following the laws of atomic or nuclear physics[2],
- a broader distribution of frequencies that can be characterised by a temperature, therefore called *thermal radiation*,
- a power law, that indicates acceleration of the radiating charged particles by external forces.

1.4.1 Thermal radiation

The most prevalent radiation in the universe is the radiation due to the temperature of a substance, a continuum emission with its peak at an energy dependent only on the temperature T, therefore also described as thermal radiation. The higher the temperature, the more energetic the photons. The form of the spectrum is defined by the well-known equation found by Max Planck:

$$I_\nu = \frac{2h\nu^3}{c^2} \frac{1}{e^{h\nu/k_B T} - 1} \tag{1.1}$$

with

- I_ν the intensity per frequency of the radiation,
- h Planck's constant and c the speed of light,
- k_B Boltzmann's constant and
- T the temperature of the radiating object, e.g. a star, an accretion disk or a hot gas cloud.

[2]The galactic γ-ray line emission at 511 keV is a current object of observation by e.g. the INTEGRAL satellite, but line emission will not be explored further in this work.

For later comparison, this equation can be written in terms of the energy E of the photon by replacing $h\nu$ with E:

$$I_\nu = \frac{2E^3}{h^2c^2 \times exp\left(\frac{E}{k_B T}\right) - 1} \tag{1.2}$$

Thermal Bremsstrahlung

Blackbody radiation is mainly emitted when thermally emitting matter is optically thick; however, optically thin matter is also able to emit thermal radiation [Haswell, 2002]. A hot gas, for example, often has a density low enough to be optically thin, causing it to be transparent to its own radiation. As absorption also depends on the wavelength, this escape of radiation from a hot gas becomes easier at higher frequencies and energies of the light. At temperatures above 10^5 K, the atoms in the gas are ionised, and it consists of positive ions and the negative electron distribution [Charles and Seward, 1995, pp. 65]. The thermal energy is shared among these particles and is transferred rapidly from one particle to another through collisions. When the gas is in 'thermal equilibrium', it means that the average energy of all particles is the same and is determined only by one temperature.

Whenever a charged particle is accelerated it emits electromagnetic radiation. So, when the electrons in the gas pass close to a positive ion, their trajectory is changed by the electric forces between the particles. This acceleration causes the emission of the *free-free* radiation or *Bremsstrahlung* (German for 'braking radiation'), with *free-free* being analogous to the atomic physics of spectral lines, where electrons undergo transitions between bound and free states.

Electrons in thermal equilibrium follow a Maxwell distribution of velocities[3] which is well determined. The spectrum of this radiation falls off exponentially at high energies and is, as a thermal radiation, characterised by the temperature T with an intensity described as (after Charles and Seward, p. 66):

$$I(E,T) \propto G(E,T)\frac{n_e n_i Z^2}{\sqrt{k_B T} \times exp\left(\frac{E}{k_B T}\right)} \tag{1.3}$$

where $G(E,T)$ is the 'Gaunt factor', a slowly varying function with value increasing as E decreases, n_i and n_e are the ion and electron density respectively.

[3] after James Clerk Maxwell

1.4.2 Non-thermal radiation

When charged particles are accelerated and subsequently generate radiation via different effects (discussed in section 1.5), the resulting energy spectrum of this radiation has the shape of a power law. Because the underlying processes are not of a thermal nature based on equilibrium distributions that can be characterised by a temperature, but instead are specific acceleration mechanisms depending on the astrophysical situation, the emerging radiation has been named *non-thermal radiation.*

Power law spectra are always indicative of highly energetic phenomena, as a power law decline in flux over energy is much slower than the high energy decline in flux of thermal processes, resulting in many more high energy particles or photons respectively compared to the thermal case.

Proposed acceleration scenarios mostly incorporate shock fronts, first modeled thoroughly by Fermi in his first and second order diffusive shock acceleration mechanisms [Fermi, 1949]. These shock fronts are indeed per se a very regular phenomenon in the universe. Everytime two distinguishable media collide, mostly gas with different densities, a shock front develops because the particles of one medium travel at supersonic speeds in the frame of reference of the other medium due to the differences in density. Examples where shock fronts appear are every solar wind situation with a sudden change in emerging density, or nova and supernova shock waves hitting the interstellar medium.

Fermi realised that when the participating media are charged particles, even the tiniest magnetic inhomogeneity in the background magnetic field — an inhomogeneity that might also be initiated and amplified by feed-back dynamo mechanisms — can appear like a magnetic mirror to any charged particles crossing the shock front, trapping these particles for a time t by bouncing them back and forth across the shock front.

Every transit of the shock front is now connected with an increase of energy, so that trapped particles can gain a significant amount of energy, depending on the time the particles spend within the acceleration region, which in turn is determined by statistical considerations for the probability of escape from the acceleration region.

Let

- β be the average increase in energy of the cosmic ray particle per shock front transit,

- P the probability that the particle stays within the accelerating region after a transit,
- E_0 the initial energy,
- N_0 the initial number of particles within the accelerating region.

Then after k collisions, one would find that there are $N = N_0 P^k$ particles with energies $E = E_0 \beta^k$. Eliminating k, one can derive the following relation:

$$\frac{N}{N_0} = \left(\frac{E}{E_0}\right)^{lnP/ln\beta} \tag{1.4}$$

In fact this N is an $N(\geq E)$, since this is the number that reach energy E, and some of these may go on the reach higher energies. Thus, to get the differential changes, one can write:

$$dN(E) = const \times E^{-(lnP/ln\beta - 1)} dE \tag{1.5}$$

A more detailed analysis, shown in detail in Longair [1992] reveals that the logarithmic ratio of the location probability and the average energy increase can be fixed as

$$\frac{lnP}{ln\beta} = -1 \tag{1.6}$$

which leads us to

$$N(E)dE \propto E^{-2} dE \tag{1.7}$$

This, however, is only true for the case of a plane shock front and leads to an overestimation of γ-ray production. More recent work, reviewed in Kirk and Dendy [2001], discusses more realistic models of shock propagation that give a cosmic ray spectrum with a power law index much softer than -2. These non-thermal distributions of charged particles subsequently radiate 'non-thermally' via different effects; the most relevant for γ-ray-production will be discussed briefly in the next section.

1.5 Generation of Very High Energy γ-rays

The basic mechanism behind emission of very high energy (VHE) γ-rays is the acceleration of charged particles with an energy loss rate for these particles being either inversely proportional to their mass or even a power of the mass. This is why generally electrons and positrons are thought to be the dominant radiating species responsible for the different effects discussed in the following sections.

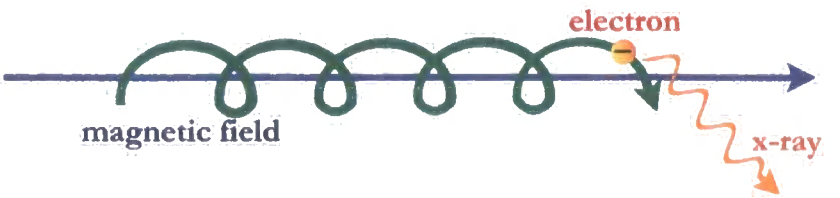

Figure 1.1: Synchrotron radiation, Image credit: NASA/CXC/SAO

1.5.1 Synchrotron Emission

When a charged particle with charge q, rest mass m_0 and energy E_p moves through a magnetic field B, and there is a non-zero component of its velocity vector $v_\perp$ perpendicular to the magnetic field, the Lorentz force will deflect the trajectory perpendicular to the current velocity and the magnetic field line, resulting in a spiral as shown in Figure 1.1.

As a result of this acceleration, the charged particle will emit electro-magnetic radiation as any accelerated charged particle. The radius of the projected circle in the plane perpendicular to the magnetic field line is known as the *Larmor* or *gyro-radius* and is given by

$$r_L = \frac{m_0 v_\perp}{|q|B}. \tag{1.8}$$

In the non-relativistic case the radiation thus produced is known as *cyclotron radiation*; in the relativistic case, however, the frequencies and intensities become very high due to the relativistic beaming effect, that forces the emitted radiation into a cone of angle $2\alpha \approx 2m_0c^2/E_p$ where c is the vacuum light speed.

The spectrum of synchrotron emission produced by a single electron for example is broad (see upper graph in Figure 1.2) with a cut-off frequency at

$$\nu_{max} = \frac{\gamma^2 e B_\perp}{2\pi m_e} \tag{1.9}$$

where γ is the relativistic Lorentz factor of the electron, e the electron charge, $B_\perp$ the magnetic field strength perpendicular to the velocity and m_e the electron mass. This equation is also valid for protons[4], though the higher proton mass shifts ν_{max}

[4]after exchanging e and m_e for the respective values of the proton obviously

down by a factor of approx. 2000.

The power radiated by a single electron is given by

$$P = \frac{\gamma^2 c \sigma_e B^2}{4\pi}, \tag{1.10}$$

where σ_e is the classical Thomson scattering cross-section. So, importantly, $P \propto B^2$ and $P \propto \gamma^2$.

In a distribution of electrons, these have many different velocities (= different speeds and orientations) with respect to the magnetic field, which yields many different ν_{max} for the whole distribution, e.g. a cloud of electrons in a hot plasma environment. The resulting spectrum constructed by many overlaid single electron spectra is shown in the lower graph of Figure 1.2.

The shape of that spectrum depends on the energy distribution of the electrons. If $N(E)\mathrm{d}E$ is the number density of electrons with energies between E and $E+\mathrm{d}E$, many sources of this non-thermal emission show a power-law distribution such as that modelled in eq. 1.7,

$$N(E)\mathrm{d}E = N_0 E^{-s}\mathrm{d}E \tag{1.11}$$

where s is known as the *particle exponent* and N_0 is a constant of normalization. As mentioned in section 1.4.2, $s = 2$ is the ideal case from Fermi's elegant statistical model, but in real astrophysical cases, s typically seems to lie between 2 and 3.

The flux emitted by this astronomical scenario at a particular frequency ν is determined by the number of electrons emitting at this frequency, $N(\nu)$, and the power P of eq. 1.10, emitted by each of these electrons. Therefore

$$F_\nu \propto P N(\nu)\ . \tag{1.12}$$

After transforming E from eq. 1.11 into ν, a lot more shuffling around (nicely shown in Haswell [2002]) and, most importantly, the assumption that all the power radiated by the electron has the frequency ν_{max}[5], it can be shown, that

$$F_\nu \propto \nu^{-(s-1)/2} \tag{1.13}$$

or, by introducing the well-known *power-law index* α, often more concisely written

[5]Most of the integrated flux comes indeed from this energy, if one compares it per energy interval; the absolute error made by this simplification depends on the magnitude of the magnetic fields involved.

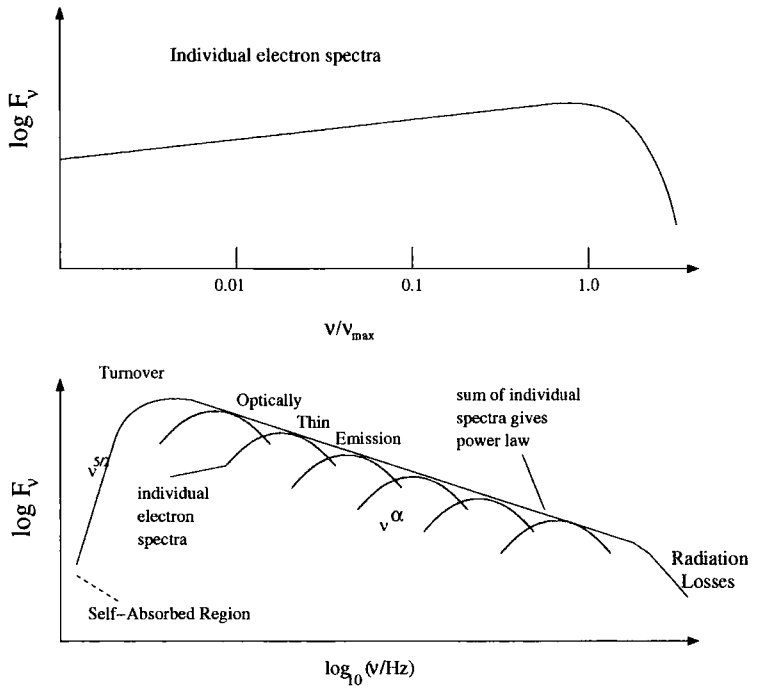

Figure 1.2: Schematic explanation of the power law synchrotron spectrum; both graphs have arbitrary but logarithmic flux units on the y-axis. Upper: spectrum of synchrotron emission from a single electron; the peak of the spectrum occurs at frequency ν_{max}. Lower: The observed synchrotron spectrum emission from a cloud of electrons is the sum of emission from many individual electrons. The low frequency region suffers from synchrotron self-absorption, the high frequency end from more efficient radiation losses of the electron population. See text for more details (Adapted/combined from Haswell [2002], Robson [1996]).

as $F_\nu \propto \nu^{-\alpha}$, where $\alpha = \frac{s-1}{2}$.

At low produced photon frequencies, the cross-section for absorption of these photons by the very electrons that have produced them via the synchrotron radiation becomes non-negligible, a process called *synchrotron self-absorption* (SSA). This causes the synchrotron emitting region to become optically thick at these low frequencies, resulting in a change of the spectral shape at low frequencies from $F_\nu \propto \nu^{-\alpha}$ to $F_\nu \propto \nu^{5/2}$ a feature known as a *low-frequency cutoff* with a *turnover* frequency (see lower graph in Figure 1.2).

1.5.2 Curvature radiation

Curvature radiation is a close relative of synchrotron radiation, with the electron no longer travelling along a straight magnetic field line, but following a very strong,

curved magnetic field such as is predicted to exist in the region of pulsars. Even the highest energy charged particles will follow these magnetic field lines very closely, as all deviations would be quickly dampened out via synchrotron radiation. As the electron's path is curved, it emits radiation, and the energy of this is proportional to $\gamma_e^3\omega$, with γ_e the Lorentz factor of the electrons and $\omega = \beta c/r$ the angular frequency of the electrons. The threshold magnetic field strength for this effect to occur is $> 10^8$ T.

1.5.3 Inverse Compton Effect

In terms of the underlying theory of quantum electrodynamics (QED), the *inverse Compton* (IC) effect is physically almost the same process as synchrotron radiation, namely an interaction between an electron and a (virtual) photon. The only difference is that in the case of synchrotron radiation the electron first reacts with a virtual photon, which is the carrier of the magnetic field, consequently radiating a real photon; whereas, in the case of the IC effect, a lower energy photon is upscattered to higher energies by an electron.

IC scattering, compared to normal scattering, happens when the photon has much smaller energies than the electron, measured by $\alpha = h\nu/(m_e c^2)$, the ratio of the photon energy to the electron's rest mass. In the rest frame of the relativistic electron, the low energy (E) photon has a much higher energy $E' = \gamma(E + p_l)$, where p_l is the longitudinal component of the photon's momentum (i.e. parallel to the electrons momentum in the lab frame). In the case of the head-on collision, $E' = 2\gamma E$, which gives an energy of $E'' = 2\gamma^2 E$ in the observer's frame. For $E' < 1$ MeV, the cross-section for this interaction is large enough for the IC scattering to become an efficient generator of VHE photons.

When the electrons have a power-law distribution of $N(E)\mathrm{d}E \propto E^{-\Gamma_e}$ and the soft photons an energy $h\nu$, the resulting γ-rays will either have characteristic energies of $(\gamma_e)^2 h\nu$ for the Thomson regime of Compton scattering or $\gamma_e h\nu$ for the Klein-Nishina regime. The governing cross-section regime is determined by α , as a small α leads to the mathematical reduction of the Klein-Nishina towards the Thomson cross-section. The resulting differential spectrum will be proportional to $E_\gamma^{-(\Gamma_e+1)/2}$.

1.5.4 Non-thermal Bremsstrahlung

The previously discussed Bremsstrahlung does not distinguish between an electron distribution of a thermal or non-thermal nature. Therefore, no matter what the energy distribution of electrons is, when this population interacts with a region rich in atomic or molecular material, Bremsstrahlung will deflect their trajectories and therefore produce electromagnetic radiation.

The complete quantum mechanical treatment of electron Bremsstrahlung by an atom is complex because of the effects of screening by the atomic electrons and the finite nuclear radius; however, the *average* cross-section is of the order

$$\sigma_b \approx 4\alpha Z^2 \frac{e^2}{m_e c^2} \tag{1.14}$$

where α is the fine structure constant[6] ($\approx 1/137$), and Z the charge of the nuclei in which field the electron is accelerated.

In the astrophysical case, one is interested in γ-ray production from a spectrum of cosmic electrons in a gas. If the gas density is ρ_g, then the production of γ-rays depends on ρ_g and the electron energy distribution. The γ-rays that result from Bremsstrahlung have energies of the same order as the incident electron so that if the electron population is characterized by a non-thermal power law spectrum with spectral index Γ_e, the resulting γ-ray-spectrum has an index $\Gamma_\gamma \approx \Gamma_e$ (after [Weekes, 2003, Appendix A]).

1.5.5 Gamma-Ray production via Pion decay

Some models exist that have populations of protons as the progenitors of VHE γ-rays [Aharonian and Atoyan, 1991]. When in these proton rich environments nucleon-antinucleon annihilations or inelastic collisions of cosmic ray hadrons with interstellar stationary hydrogen gas takes place, neutral pions can be produced. The threshold kinetic energy of the incident proton is 290 MeV and the most common interaction has the form:

$$p + p \rightarrow N + N + n_1(\pi^+ + \pi^-) + n_2(\pi^0) \tag{1.15}$$

where N is a proton or neutron and n_1 and n_2 are integer numbers. Below 1 GeV, $n_1 = n_2 = 1$; however, at high energies the cross section for π production is constant

[6] $\sqrt{\alpha}$ is the coupling constant of QED

Production of HE/VHE γ-rays

Interaction	Critical parameters	Characteristic E_γ	Differential spectrum
Compton scattering	$I_e, \rho_p h$	$\gamma_e^2 h\nu$(Thompson) $\gamma_e h\nu$(Klein-Nishina)	$E_\gamma^{-(\Gamma_e+1)/2}$
Bremsstrahlung	I_e, ρ_g	E_e	$E_\gamma^{-\Gamma_e}$
π^0 decay	I_p	70 MeV	$E^{-4/3(\Gamma_p-1/2)}$

Table 1.2: I_e and I_p are the power law distributions of electrons and protons respectively; ρ_g is the electron gas density; $h\nu$ the photon energy; Γ_e and Γ_p the spectral index of the energy distributions of the electron and proton populations respectively [after Weekes, 2003, Appendix A].

and equal to 27 millibarn. These pions may then decay into two γ-rays, with each having an energy of approx. 70 MeV as seen in the rest frame of the π_0.

If the cosmic rays have a power-law spectral distribution with index Γ_p, then at high energies the γ-ray spectral distribution will also be a power-law with (see also table 1.2).

$$\Gamma_\gamma = \frac{4}{3}\left(\Gamma_p - \frac{1}{2}\right). \tag{1.16}$$

As the energy decreases, the spectrum turns over with a peak at 70 MeV. It is this peak that is the characteristic feature of the p-p interaction and the signature of hadrons as the progenitors in cosmic γ-ray sources (after Weekes [2003, Appendix A]).

1.6 Theoretical Sources

Depending on the presumed source of γ-rays, different generation processes have been proposed. The following paragraphs describe the objects that have been under examination so far as potential sources of high energy γ-rays.

Supernova remnants (SNR)

When a shockwave of a SNR hits the inter-stellar medium (ISM), the Fermi shock accelerations ([Fermi, 1949], detailed discussion in [Drury et al., 1994]) increases the energy of particles in the ISM to very high values. This is done by scattering the particles back and forth on magnetic inhomogeneities in front of and behind the shock front. How exactly a particle is 'injected' into the coordinate system of the shock front, i.e. how exactly the particle is 'caught' by the shockwave, is

still unclear — and known as the 'injection problem' — but model calculations for the subsequent diffusive acceleration [Biermann, 1993] show energies up to 10^{15} eV attainable. Within our galaxy the SNRs are believed to be the main source of particles with these energies [Aharonian and the H.E.S.S. collaboration, 2004c].

It is convenient, thought not distinguishable in a definite way, to divide γ-ray observations of SNRs into two parts: plerions and shell-type SNRs. VHE observations of the Crab nebula and PSR 1706-44 plerions seem to indicate the connection of plerions with VHE γ-rays, as HE γ-rays have been linked successfully with shell-type SNRs like Kepler's supernova SN1604; however, neither set of observations have provided the means to tie uniquely the origin of the cosmic radiation with SNRs.

Plerions

Plerions are formed when a relativistic wind from a pulsar is confined by a more slowly expanding shell of the surrounding supernova remnant. The energy of the pulsar is dissipated via diffusive shock acceleration that generates a highly relativistic electron energy distribution. In the case of the Crab nebula, the photon emission occurs over a remarkably broad dynamic range, stretching from energies less than 10^{-4} eV to nearly 10^{14} eV. The lower part (up to 100 MeV) can be explained by synchrotron radiation within the nebula, indicating the presence of electrons with energies as high as around 1000 TeV. When these relativistic electrons diffuse from the shock front into the nebula, inevitably inverse Compton up-scattering of either the previously produced synchrotron photons (*Synchrotron Self Compton* effect (SSC)), microwave background radiation or thermal radiation from dust. These models, when applied to the most prominent γ-ray-source, describe the available data well, as shown in Hillas et al. [1998]. After electrons have achieved a power-law energy distribution due to this shock acceleration, Bremsstrahlung may also be a very important effect for gamma-ray production in these kind of sources, depending on the density of the medium behind the shockfront.

X-ray Binary systems

If one of the partners in a binary system is a compact object like a white dwarf, a neutron star or a black hole, it is possible for this compact star to *accrete* matter from its companion. During this accretion process (see Frank et al. [1992] for an excellent but challenging introduction into accretion physics), the matter gets heated, ionized

and accelerated. Depending on the structure of the accretion disk, a temperature profile develops in the radial direction, with the highest luminosity close to the surface of the accreting star, releasing the gravitational energy as thermal X-ray radiation. If the compact star has a strong magnetic field, the accreted matter is forced along trajectories that follow the magnetic field lines. In this way, ions can be accelerated to energies up to 10^{17} eV. When these ions now interact with the ISM surrounding the binary system, π^0-mesons are generated which decay into two high energy γ-rays. Another potential effect is the inverse Compton radiation, where the electrons accelerated by the magnetic fields can interact with the X-ray photons of the accretion disk to increase their energy even further.

Pulsars

It is generally accepted that pulsars are rapidly rotating compact neutron stars in a magnetosphere, the region of space around the pulsar, where the magnetic energy density is higher than the radiation energy density; magnetic field strengths around 10^8 T are predicted to dominate these regions. These magnetic fields carry plasma that reaches the speed of light at their particular radii due to their rotational velocity. At this radius, radiation is emitted tangentially from these regions in a focussed beam, similar to the hammer leaving its orbit tangentially in hammer throwing.

Pulsars are divided into two categories: rotation-powered and accretion-powered. The former are generally detectable at radio wavelengths and the latter at X-ray wavelengths. The emission process for these X-rays are generally of a thermal nature, and no such extreme thermal processes can generate γ-ray-fluxes like those being observed from other objects. However, jet acceleration processes in certain binary systems known as *microquasars* may be capable of producing non-thermal gamma radiation.

Rotation-powered pulsars are believed to be formed in supernova explosions when the cores of massive stars ($> 8M_\odot$) collapse due to conservation of angular momentum. The radiation luminosity is assumed to be proportional to the rotational energy loss, observed as a general gradual increase of the rotation period for all pulsars. But beyond the general properties, that the strong magnetic fields and the rotation play a significant role in production of the non-thermal radiation, no general agreement about the nature of pulsars or their radiation mechanisms exists. Curvature radiation is, however, a favourite candiate for part of the spectrum, when it can be shown, that the magnetic fields are strong enough ($> 10^8$ T).

The γ-ray-radiation is currently modeled by two different scenarios called the outer-gap and the polar-cap models respectively. Daugherty and Harding [1994] have shown that the region above the polar cap can reproduce the observed γ-ray light curves and spectra. A quantum electro-dynamic effect called 'magnetic pair production' produces cutoffs around a few GeV but some objects have shown cutoffs at lower energies.

The outergap model of Cheng et al. [1986] predicts that the γ-rays are produced near the light cylinder with radius $r_L = \frac{c}{\omega}$, and the cutoff is expected to result from energetic arguments, rather than from magnetic pair production.

Active Galactic Nuclei (AGN)

In the centres of active galaxies, of which radio- and Seyfert-galaxies are a sub-sample, super massive black holes are presumed to exist with masses of up to 10^8 solar masses. When these black holes accrete matter, the released gravitational energy — to put it very generally — is emitted in the form of jets with their direction parallel to the axis of the accretion disk. Within these jets charged particles are accelerated, presumably by shock acceleration. An AGN is now the standard term for a system of a black hole together with some kind of accretion disk that is most probably in time-varying states. These AGN are assumed to be sources of CR in the energy region of $10^{15...20}$ eV.

Galaxy clusters

Galaxies are bound together by gravitation to build very large objects called galaxy clusters, only outplayed by clusterisation of galaxy clusters, so called Hyper- or Superclusters, that define the so far largest known scales in the universe. It is assumed that at time of creation of the clusters a strong non-thermal component of relativistic particles was generated. These particles were then accelerated in the early phases, as well as at later events in the history of the cluster, and subsequently imprisoned in the turbulent inter-cluster medium. This prison sentence is assumed to exceed the life-time of the cluster, so that the energy spectrum of the particles inside the medium will be the same as the spectrum of the sources which generated the particles in the first place. Through supernovae inside the individual galaxies — which can sum up to 500 at any time inside a cluster — we now have a source of permanent energy input via the galaxy winds produced by the supernovae which are

as well confined to the inter-cluster medium. For the example of the Perseus-Cluster it is expected that inside the medium energies up to 10^{62} erg can be accummulated. More details can be found in [Völk, 1996].

1.7 Attenuation of Very High Energy γ-rays

The interactions of photons with matter are mainly described by three processes: photoelectric effect, Compton effect and pair production, with strong dependencies on the materials involved. The cross sections for photo- and Compton effect, however, only dominate at lower energies, in the keV regime and between several 100 keV up to a few MeV, respectively. Over 10 MeV energy, pair production is the dominant cross section.

1.7.1 Pair production through interactions with ambient media

As the spontaneous decay of a single photon into an electron/position pair is forbidden due to momentum conservation, an ambient medium is necessary to allow a single VHE γ-ray to decay.

For a 1 TeV photon the radiation length, the distance travelled by the photon after it has lost 1/e of its energy, corresponds to a column density of approx. 37 g cm^{-2} [Ong, 1998]. However, the intergalactic average density is approximately 1 hydrogen atom cm^{-3}, which amounts up to approx. 0.04 g cm^{-2} towards the centre of the galaxy (disregarding the increase in matter density near the centre). Also, the intragalactic matter densities are estimated to be even lower. This shows that a matter induced pair production becomes very unlikely during inter- and intragalactic travel. This becomes different in supernova remnant and accretion environments, where the gas densities could become high enough in the line of sight to the observer to attenuate a non-negligible amount of VHE γ-rays when the photon is getting close to a nucleus N:

$$\gamma + N \rightarrow N + e^+ + e^- \tag{1.17}$$

1.7.2 Photon-photon pair production

With the reverse electron-positrion annihilation,

$$\gamma + \gamma \rightarrow e^+ + e^- \tag{1.18}$$

	E_1 (eV)	E_2 (eV)
Microwave background	6×10^{-4}	4×10^{14}
Starlight	2	10^{11}
X-ray	10^3	10^8

Table 1.3: Threshold energies for photon-photon pair production. E_1 is the average energy of the photon field the VHE γ-ray is colliding with, E_2 is the respective threshold energy for the γ-ray (After Longair [1992]).

it becomes possible to lose photons without the presence of ambient matter. The threshold for this interaction is given by [Longair, 1992]:

$$E_2 = \frac{2m^2c^4}{E_1(1 - cos\theta)} \tag{1.19}$$

where E_1 and E_2 are the energies of the respective photons and θ the angle between their paths. From this one can deduce the threshold for a head-on collision to be $E_1E_2 \geq 0.26 \times 10^{12}$ eV. Table 1.3 lists the different thresholds for VHE photon-photon interaction depending on different kinds of photon fields.

The possibility of inferring the photon (energy) densities of intervening photon fields by observation of VHE γ-rays is an exciting new field for testing all kinds of astronomical models, starting from measuring the microwave background and its cosmological importance, the distribution of the infrared background, important for star formation, and measuring the strength of magnetic fields near neutron stars by photon-photon interaction with the virtual photons of the magnetic field lines (for $B_{NS} \geq 10^2$ T). The obvious prerequisite to enable these kind of studies is a more or less precise knowledge of the source spectrum. This is one of the main goals of the active research and will be made easier with the increased source statistics from the detection of more γ-ray-sources by the new generation of VHE γ-ray detectors, as these have on average a factor ten larger flux sensitivity compared to the main experiments of the 1990s.

1.8 Current Status of VHE γ-ray astronomy

Ong [2003] has given a good status overview for the state of early 2003. Facts from that summary shall be combined in this section with other recent results up to autumn 2004.

New instrumentation has enabled the community to steadily increase the source

count. HEGRA detected the first unidentified VHE source in the vicinity of the OB star association Cygnus OB2 [Aharonian et al., 2002] with an indicated extension that disfavours an exclusive pulsar or AGN origin of this radiation. Now H.E.S.S., for the first time, has discovered two sources in the area of the field of view of an imaging Cherenkov telescope, one of them being the second unidentified VHE source HESS J1303-631 [Beilicke and the H.E.S.S. collaboration, 2004]; this source as well seems to be extended (on the 0.2° level) and has serendipitously been discovered while observing another new confirmed VHE γ-ray source, the pulsar PSR 1259-63.

1.8.1 Reliable candidate sources

Table 1.4 gives an overview of the most trusted well-accepted VHE γ-ray sources as of December 2004. In the following some details of some of the trusted sources shall be given.

PKS2155-304

The AGN PKS 2155-304, first discovered by the Durham group [Chadwick et al., 1999], has been confirmed very strongly by the H.E.S.S. experiment [Aharonian et al., 2005]. H.E.S.S. claims a 45σ detection at energies greater than 160 GeV. Variability has been observed on timescales of months, days and hours, with a monthly averaged intensity above 300 Gev of 10 to 60% that of the Crab nebula (note the vastly greater distance of redshift $z = 0.117$ to PKS2155 compared to the galactic Crab nebula!)

SNR J1713.7-3946

The shell-type SNR J1713.7-3946, discovered by ROSAT in X-rays and later claimed to be detected in VHE γ-rays by the CANGAROO experiment, could also be confirmed by the H.E.S.S. group [Aharonian and the H.E.S.S. collaboration, 2004b]. The first ever γ-ray-image on arcminute scale could be achieved with this object by the H.E.S.S. group and the spectral analysis of the same observation indicates charged particle acceleration beyond 100 TeV, consistent with current ideas of particle acceleration of young SNR shocks.

Multiple detected sources

Name	Category	Reference
Crab nebula	pulsar nebulae (plerion)	[1]
Markarian 421	AGN	[2]
Markarian 501	AGN	[3]
H1426+428	AGN	[4]
1ES 1959+650	AGN	[5]
PKS 2155	AGN	[6]
Sagittarius A*	unclear	[7]
SNR J1713.7-3946	SNR	[8]

Table 1.4: Table of sources that have been claimed for detection by multiple experiments. References: [1] Masterson et al. [2005]; [2] Lemière and Hess Collaboration [2005]; [3] Aharonian et al. [1999]; [4] Horns et al. [2004]; [5] Krawczynski et al. [2004]; [6] Aharonian et al. [2005]; [7] Aharonian and the H.E.S.S. collaboration [2004c]; [8] Aharonian and the H.E.S.S. collaboration [2004b]

Mkn 421

Markarian 421 is the closest BL Lac object with a redshift of $z = 0.031$ and a well-established VHE γ-ray source in the northern hemisphere. H.E.S.S. observations at low zenith angles on average of 62° will achieve new constrains on the upper energy limits, once the H.E.S.S. systematics are better understood and trusted. The data showed a very high variability with detection levels ranging from approx. 6σ in a 2.12 hour data set to 95σ in a 11.5 hour data set, showing Mkn 421 in an active state.

Sagittarius A*

A point like source of VHE γ-rays coincident within $1'$ of Sgr A* is reported by the H.E.S.S. group and has been seen by two other groups before. The reported power law spectral index of around -2.2 and the flux above 165 Gev of $(1.82 \pm 0.22) \cdot 10^{-7}$ $m^{-2}s^{-1}$ differ substantially from recent results reported in particular by the CANGOROO collaboration (see [Aharonian and the H.E.S.S. collaboration, 2004c] and references therein). The galactic centre region harbours a great variety of potential sources of high-energy radiation including the supermassive black hole Sgr A*, which has been identified in X-rays and infrared. VHE emission from Sgr A* is presumably powered by the energy released in the accretion os stellar winds onto the black hole, although other theories like annihilation of dark matter and shock acceleration of electrons or even protons exist.

Probable sources

Name	Category	'H.E.S.S. status'
PSR 1259-63	binary radio pulsar	detected [1]
HESS J1303-631	unknown	detected [2]
Vela	pulsar	not detected [3]
PSR 1706-443	plerion	not, but by 2 other groups [3]

Table 1.5: Table of sources that have been claimed at least by one experiment with high statistics. References: [1] [Schlenker et al., 2005]; [2] [Beilicke and the H.E.S.S. collaboration, 2004]; [3] [Khélifi et al., 2005]

1.8.2 Probable sources

In addition to the sources shown in table 1.4, some sources have been detected by one experiment, or in some cases by several but with a null result from H.E.S.S.. Though this categorization in terms of H.E.S.S. detectability might seem bold, the author believes, that a non-detection of an instrument with a sensitivity of a magnitude higher than other current instruments can at least indicate a transient source behaviour.

1.9 Preview

After this chapter has introduced the general concepts and physics involved in the creation of VHE γ-rays, the next chapter shall describe the favourite detection technique for the VHE energy regime of γ-rays, the detection via the Cherenkov light of particles in extensive air showers, produced by the impact of a primary γ-ray in the atmosphere. After that, in chapter 3, I will describe the technical features of the H.E.S.S. experiment and how it solved the challenges posed by this particular detection technique.

Chapter 2

Atmospheric Cherenkov technique

In this chapter I will describe the general idea of the Imaging Atmospheric Cherenkov technique for detecting very high energy (VHE, energies between 10 GeV and around 100 TeV) gamma rays. I will show how particle showers develop through the atmosphere, describe parameters that are important for the astronomical observations and show which of these parameters are affected by the atmosphere. Many of the numbers, equations and graphs in this chapter are taken either from the excellent review papers on gamma-ray astronomy of Fegan [1997] and Ong [1998] or the book of Weekes [2003].

2.1 Extensive air showers

When a high-energy CR particle hits the atmosphere, it reacts with the nuclei via a cascade of interactions also known as an extensive airshower (EAS). These cascades produce avalanches of secondary particles via Bremsstrahlung and pair production, effectively described by the shower model of Heitler [1954]. Generally these showers have to be distinguished by the nature of the primary particle that collides with the atmosphere. Hence the two possible kinds of showers are called *hadronic* and *electro-magnetic* showers.

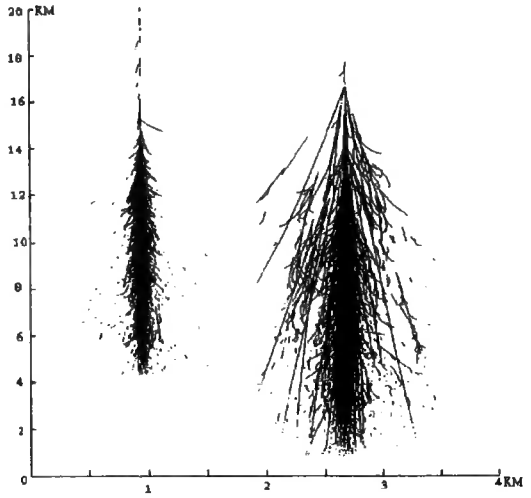

Figure 2.1: Monte Carlo simulation of the develoment of a 300 GeV γ-ray shower (left) and a 900 GeV hadron shower (right) in the atmosphere. Note the more compact nature of the γ-ray shower. The horizontal scale has been exaggerated by a large factor for clarity of illustration (after Kertzman and Sembroski [1994], taken from Fegan [1997]).

2.1.1 Electro-magnetic shower

If the primary particle is a gamma-ray with an energy higher than 1.022 MeV, the limit for the pair production effect, it will create e^+e^- pairs in the neighbourhood of the electrical field of a nucleus for absorption of the overabundant momentum of the photon. The efficiency of momentum absorption depends on the structure of this electric field and is therefore a parameter dependent on the material the photon is colliding with; generally, for the limit of pair production to be of higher probability than Compton scattering, the energy of the photon needs to be higher than several MeV (e.g. 5 MeV for photon scattering in lead). These electrons and positrons can now both ionise atmospheric ions and also create new photons via Bremsstrahlung.

The mean free path length for ionisation is similar to the mean free path length for Bremsstrahlung[1], with a total mean free path length or radiation length x_0 of 37 g cm^{-2} for a 1 TeV gamma-ray [Ong, 1998]. Considering that the atmosphere's column density from outer space to sea level can be approximated to 1000 g cm^{-2}, the total mean free path corresponds to $\sim$ 26 radiation lengths. Because of the comparable radiation lengths of these competing processes, the cascade does not go on forever as not all of the energy goes back into creation of new e^+e^- pairs but

[1]due to the similarity of the process from the viewpoint of quantum electrodynamics (QED)

is spent on ionisation. The number of secondary particles in the shower increases exponentially until the energies of the leptons reduce to the critical energy E_c at which the energy-loss for ionisation is larger than for Bremsstrahlung ($\sim$ 84 MeV for an electron in air). At this point the maximum development of the shower is reached and subsequently the shower dies off exponentially again by ionisation losses.

A simple calculation of the height of the shower maximum x_{max} can be deduced from a few straight forward assumptions. Firstly, in the ultra-relativistic limit the radiation lengths (or better interaction length in this case) for pair production of a photon and the Bremsstrahlung radiation length of an electron/positron are similar and both of exponential character. Therefore, considering only Bremsstrahlung and pair production as determining forces for the shower development, it is possible to say that at a certain point in the shower development the probability of these processes taking place is 1/2 at the distance x, which is given by

$$exp\,(-x/x_0) = \frac{1}{2} \tag{2.1}$$

with x_0 being this similar radiation length for both processes. Using this one can define an interaction length L like

$$L = x_0 \ln 2. \tag{2.2}$$

Furthermore assuming — on average — a symmetric energy sharing between the secondary particles, after the distance of nL interaction lengths, 2^n particles have been created, so that the energy E_0 of a primary particle has now been shared between the particles as

$$\langle E \rangle = \frac{E_0}{2^n} \tag{2.3}$$

where $\langle E \rangle$ is the average energy of an secondary particle.

The shower maximum is reached when this average energy reaches a critical energy E_c, below which the dominant loss process for the electrons is ionisation rather than Bremsstrahlung. This leads to the number of particles at the shower maximum to be

$$2^{n_{max}} = \frac{E_0}{E_c}, \tag{2.4}$$

with n_{max} the number of generations it took the cascade to reach the critical energy. After solving for n_{max} and subsequent replacements using eq. 2.2 and $n_{max}L = x_{max}$ this can be written in terms of the maximum shower height in units of the previously

mentioned similar radiation length of both shower processes:

$$\frac{x_{max}}{x_0} = ln\,\frac{E_0}{E_c} \propto ln\,E_0. \tag{2.5}$$

More sophisticated methods of this simple shower model include the ionisation losses and yield a value of approx. 10 km for the height of the shower maximum of a 1 TeV γ-ray shower.

This model calculation indicates that the numbers of secondary particles can be related to the energy of the primary particle. The amount of Cherenkov light created by this core cylinder is then a measure of the primary energy, and the resolution of this determination yields an error up to 30–40% for a single telescope, due to the main uncertainty of the core location (a close low energy event looks similar to a distant high energy event). The stereoscopic technique (see section 2.5) can reduce this uncertainty down to 10–15%.

The energy of the primary particle determines the depth of the shower development into the atmosphere, known as the shower depth. Provided the primary has enough energy, the secondary particles (or even the primary, if its energy is high enough) can reach the earth's surface and can then be registered with particle counters as they are used in high energy experiments. If their energy is not quite high enough to reach the ground, one can observe the airshower via the Cherenkov effect (see section 2.2).

2.1.2 Hadronic shower

Unfortunately outweighing the gamma-ray showers by a factor of 1000:1, so called *hadronic showers* are produced by the hadronic[2] components of the cosmic radiation; despite their well-understood composition, these showers are nowadays historically still being described as cosmic-ray showers, even though gamma-ray showers are the only 'ray'-like showers within the cosmic radiation.

Because the incoming hadron will react with the nuclei of the atmosphere via the strong nuclear force, the resulting number of possible secondary particles per reaction is much higher, as the production of the pions $\pi^{\pm}$ and π^0 and kaons is possible. Because of the larger amount of secondary particles per reaction, and because the decay into pions tends to produces larger scattering angles than the pair production,

[2]Hadrons are particles composed of quarks, i.e. nucleons and mesons, with *hadron* being Greek for 'heavy'

a larger amount of transverse momentum can be transferred to the secondaries, resulting in a greater spread of the shower cascade through the atmosphere. This difference in the shower development compared to the more concentrated electromagnetic showers (compare in Figure 2.1) is a major factor that, in connection with the physics of the Cherenkov light, leads to the main features that enable the separation of γ-ray- and hadron showers in the imaging Cherenkov technique.

2.2 The Cherenkov effect

When a charged particle moves with a speed higher than the speed of light in the medium through which it is travelling, Cherenkov light is emitted. This effect is comparable to the sonic boom effect, where an object travels through a medium at a higher speed than the sound speed in this medium. In this case, a shockwave is created by the object, noticeable by its loud noise, the trans-sonic boom. The Cherenkov light flash in this picture could therefore be called a trans-light flash, with the light being an reaction of the electrons of the atmospheric particles to the electric field of the relativistically passing charges.

The first condition to be fulfilled for generation of Cherenkov light is that the particles of the shower have a speed

$$v_p > c_m = \frac{c}{n(\lambda)} \tag{2.6}$$

with v_p being the speed of the particle, c_m the reduced speed of light inside a medium and n the index of refraction of the medium.

This can be written in terms of the minimum energy of a relativistically moving particle required for the generation of Cherenkov light:

$$E_{min} = \frac{mc^2}{\sqrt{1-\beta_{min}^2}} \text{ with } \beta_{min} = \frac{1}{n(\lambda)}. \tag{2.7}$$

Particles with $\beta < n^{-1}(\lambda)$ cannot emit Cherenkov light at wavelength λ. This for example results in an energy threshold of more than 35 MeV for electron or positrons and about 8 GeV for muons at 10 km altitude [Bernlöhr, 2000] , the altitude at which the maximum of Cherenkov light production is expected, following the results of Monte-Carlo simulations.

But equation 2.7 describes emission at the limit of $\Theta_c = 0°$. The emission angle

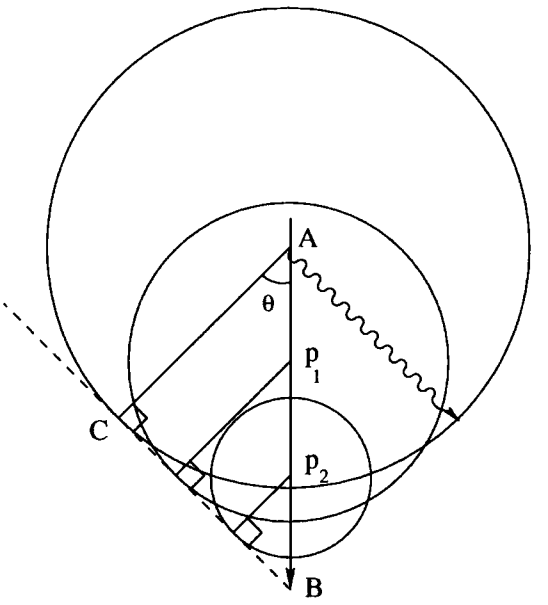

Figure 2.2: Huygens construction illustrating the coherence and emission angle for Cherenkov light. At particle velocities beyond the lightspeed in the medium, the wavefronts from arbitrary points p_i along the track AB combine to form a plane wave front BC. This coherence takes place when the particle's travel time from A to B is equal to that of the light from A to C. See text for the calculation of the emission angle Θ [taken from Daniel, 2002].

is determined by

$$cos\,(\Theta_c) = \frac{1}{n\beta} \text{ with } \beta = \frac{v}{c}. \tag{2.8}$$

This corresponds in the limit $\beta = 1$ and for $n = 1 + \eta$ with $\eta \ll 1$ to

$$\Theta_c \approx \sqrt{2\eta}\ . \tag{2.9}$$

On sea level for example, Θ_{max} is approx. 1.4°. Via the index of refraction, this process is tightly bound to the atmospheric profile. As the density changes, n is changing,

$$\eta(h) = \eta_0 exp\left(-\frac{h}{H_0}\right)\ , \tag{2.10}$$

where $\eta_0 = n - 1$ at ground level and H_0 the scale height for an exponential atmosphere.

As eq. 2.8 shows, the refractive index also affects the angle of emission relative to the trajectory of the particle (see Figure 2.2) , another important parameter in

the atmospheric Cherenkov technique. The emission angle determines the photon-density per area of the Cherenkov light on the ground. As mentioned, at sea level it is approx. 1.4°, but this angle decreases with increasing altitude due to the decreasing refractive index, resulting in a 'focusing' effect with most of the Cherenkov light arriving on the ground within a circular light pool with a radius of approx. 125 m. Within this radius, the number of Cherenkov photons emitted is proportional to the energy of the primary gamma ray.

As the refractive index is very close to unity, the difference in speed of the particles and the emitted Cherenkov light is not very big, so it almost catches up with it during the bulk of light production, which is the reason why the Cherenkov pulse only has a length of a few nanoseconds. However, still the light emitted from the higher elevations will reach the ground last.

The number of Cherenkov photons emitted per unit path length in the wavelength range $\lambda_1 \ldots \lambda_2$ is described by [Bernlöhr, 2000]:

$$\frac{dN}{dx} = 2\pi\alpha z^2 \int_{\lambda_1}^{\lambda_2} \left(1 - \frac{1}{(\beta n(\lambda))^2} \frac{1}{\lambda^2} d\lambda\right). \tag{2.11}$$

with α being the fine structure constant ($\approx 137^{-1}$) and z the charge of the transient particle.

As one can see, n affects the number of Cherenkov photons emitted. This is one of the primary reasons why monitoring of atmospheric parameters and determination of the kind of prevailing profiles at the site of observation is so important.

The energy of the primary particle determines how deep the shower will develop into the atmosphere, i.e. how many generations of new particles will be created and through this, the amount of Cherenkov light produced, with of course additional dependency on the atmospheric profile.

2.3 Imaging principle

Just like big optical telescopes, a Cherenkov telescope consists of a mirror, which focuses the incident light, and a light detector, the camera, that is positioned at the focal point of the mirror (see more detail for the case of the H.E.S.S. experiment in section 3.2). As it was shown in section 2.1.1, the number of particles is highest at the shower maximum. Therefore the bulk of the light, approx. 50% of all the Cherenkov light from the shower, comes from a cylinder of length 4 km and a radius

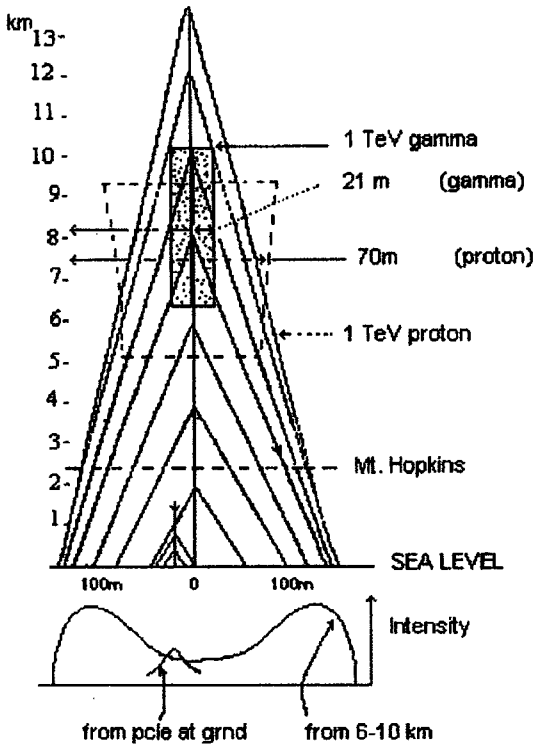

Figure 2.3: Geometric model of emission of Cherenkov radiation for γ-ray and hadron showers. The stippled region encloses the main emission region for production of Cherenkov light from γ-ray showers. Around the illustrated median altitude of 8.1 km this corresponds to 50%. The intensity profiles on the ground reflect the peaking in the Cherenkov lateral distribution for γ-ray showers at distances close to 126 m from the centre of the light pool (after Hillas [1996], taken from Fegan [1997]).

of 21 m centered on the shower core [Weekes, 2003], as shown in Figure 2.3. The light from this region alone is already a good measure of the total energy, and is best measured at a distance of $\sim$100 m, because of the higher detail the shower development is recorded, when the physical image gets elongated in the camera due to its distance to the shower core. The angular spread of this light (as described by the Molière radius) will have a half-width of $\sim$0.2°, predominantly caused by the Coulomb scattering during the shower development, and not by the Cherenkov angle as one might have assumed.

The other 50% of light comes in roughly equal shares from shower particles at elevations between the height of the first interaction down to the shower maximum at approx. 10 km, and the so-called *local component* of the shower, the particles

radiating below an elevation of about 6 km, the region under the central maximum cylinder. It is this last 25% of the light that is subject to the largest fluctuations, as it is created by the few surviving particles from the exponential shower decay following the shower maximum. But this is also the region where the light is subject to the largest attenuation caused by the atmosphere. Therefore, although in strict mathematical order only a secondary effect, the state of the atmosphere has direct influence on approx. 25% of the light received on the ground and is therefore a non-negligible effect for the estimation of the energy of the primary particle.

The camera in the focal plane of the telecope for the detection of the Cherenkov photons is currently mostly built of photo-multiplier tubes (PMTs). The profile created by this image is known as the longitudinal profile of the shower. It describes the development of the shower with the height over ground. The lateral development is imaged by the IACT in a similar way. The resulting characteristic light distribution in the camera, can be approximated to a first order as an ellipse. The quantitative parameters needed to describe the morphology of this image are called Hillas-parameter [Hillas, 1996], named after the inventor Michael Hillas (see Figure 2.4).

These parameters enable distinction between γ-ray showers and the 1000 times more frequent hadronic showers, as the shower development in the atmosphere is different for hadronic showers; these differences in the shower development are identified by a different image morphology in the camera, described by the the Hillas parameters in an analytical way.

2.3.1 Shower image parameter definitons

Moments are based on the ADC counts in each pixel, together with the particular pixel coordinate. The zeroth-order moment, e.g. is simply the sum of all pixel signals that are non-zero after filtering and cleaning of the camera picture (e.g. as currently used in H.E.S.S.: 10 ADC counts to define a pixel that is part of the image, and 5 ADC counts to define a 'boundary' pixel). The first-order moments then describe the position of the image in the focal plane of the camera and the second-order moments the extent of this image.

For example, when tube positions are given in coordinates x and y, measured in degrees, and n is the number of digital counts in a tube after gain calibration,

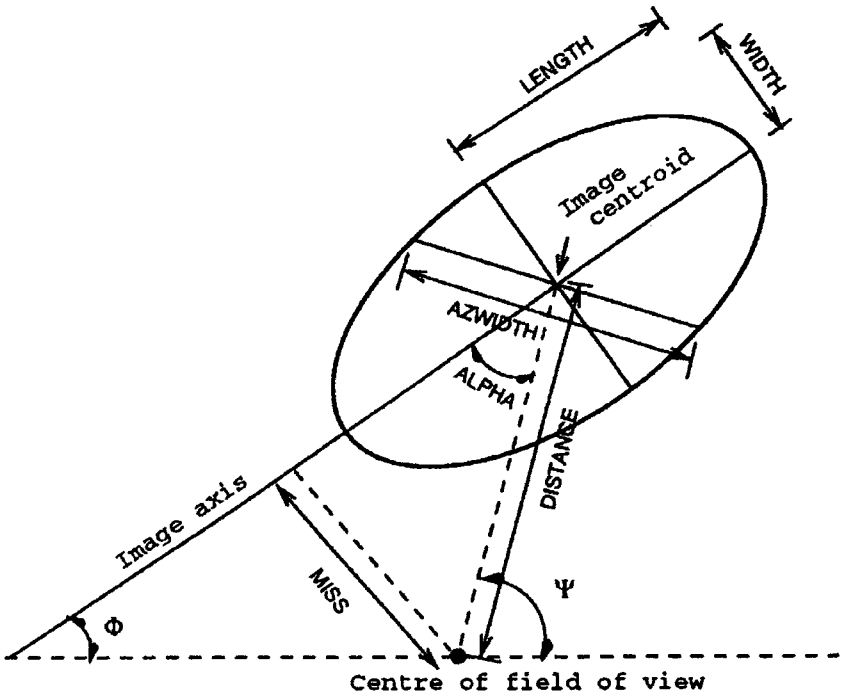

Figure 2.4: Shower image parameters based on a moment analysis. The image is approximated by an ellipse where the semi-major and semi-minor axes reflect the length and width parameters and represent the 'shape' of the captured image. The alpha, miss and azwidth parameters relate to the 'orientation' or 'pointing' of the image. The distance parameter is a measure of the image centroid from the centre of the camera field of view (see also section 2.3.1) [after Fegan, 1997]).

pedestal subtraction and image cleaning, one can define a first order moment like:

$$\langle (x;y) \rangle = \frac{\sum n_i (x_i;y_i)}{\sum n_i} \tag{2.12}$$

and an example for a second-order moment, that describes the image spread, can then be defined like

$$\sigma_{(x;y)^2} = \langle (x;y)^2 \rangle - \langle (x;y) \rangle^2 \tag{2.13}$$

with $(x;y)$ meaning, that the equation is to be used either for x or y. If one then defines

$$d = \sigma_{y^2} - \sigma_{x^2} \text{ and } s = \sqrt{d^2 + 4\,(\sigma_{xy})^2} \tag{2.14}$$

the length parameter, for example, could be described as

$$length = \sqrt{\frac{\sigma_{x^2} + \sigma_{y^2} + s}{2}} \,. \tag{2.15}$$

The following is a list of the Hillas parameters, taken from Fegan [1997]; for all other moment calculations the interested reader is referred to this review as well.

2.3.2 Image parameters

Size The total integrated light content of the shower.

Width The rms spread of light along the minor axis of the image, a measure of the lateral development of the cascade.

Length The rms spread of light along the major axis of the image, a measure of the vertical development of the cascade.

Miss The perpendicular distance between the major axis of the image and the centre of the field of view of the camera, a measure of the shower orientation.

Distance The distance from the centroid of the image to the centre of the field of view of the camera.

Azwidth The rms spread of light perpendicular to the line connecting the centroid of the image to the centre of the field of view. This is a measure of both the size and the orientation of the image.

Frac 2 The degree of light concentration as determined from the ratio of the two largest tube signals to the sum of all signals, sometimes referred to as *concentration* or *conc.*

Asym A measure of how asymmetric the image is, γ-ray images should have tails which preferentially point away from the source position.

Alpha A derived parameter $\alpha = \sin^{-1}$ (miss/distance), the angle between the major axis of the image and the radius drawn from the centre of the camera through the centre of the image.

2.3.3 Triggering Cherenkov telescopes

The Cherenkov telescope has to trigger on the Cherenkov photons produced by an EAS amidst the noise produced by background noise from photons of the night sky background (NSB). But Cherenkov light has certain attributes that greatly facilitate the detection:

1. the Cherenkov pulse is fast, approx. 5 ns full width half maximum (FWHM),
2. the angular size of the beam of Cherenkov light is limited to about 1°,
3. and the Cherenkov light peaks at short wavelengths in the blue/UV compared to the NSB peaking at long wavelengths.

To exploit the first and third point, one is using fast PMTs with a sensitivity maximising at the wavelengths of the Cherenkov light peak, as shown in Figure 4.2.

Typically, the three main conditions for triggering a readout of the telescope can be described as

- a minimum number of pixels of the camera (within geometrical restrictions),
- exhibiting a signal larger than a pre-set threshold,
- within a short time, the trigger window;

this threshold is usually set to a few photoelectrons, because a single photon (mostly from NSB) already creates two to four photoelectrons, when it hits the photocathode of a PMT (with a quantum efficiency of ~20%).

When triggered, the PMT signals are digitised with an Analogue to Digital Converter (ADC) and read out (transported to a storage system), resulting in a dead-time ranging from a few 10 μs to a few 10 ms, depending on the design of the data acquisition system (see e.g. the details for the H.E.S.S. trigger system in Funk et al. [2005] and in section 3.5).

A scaling factor can be defined for the Cherenkov photon yield, y_γ, in the following way:

$$y_\gamma \equiv \frac{\rho_\gamma}{E} \ , \tag{2.16}$$

where ρ_γ is the density of Cherenkov light on the ground in photons/m^2 and E the energy of the primary gamma ray. For wavelengths between 300 and 550 nm, y_γ is approx. 0.033 photons m^{-2} GeV^{-1} at 25 GeV [Ong, 1998]. It increases smoothly

to approx. 0.065 photons m^{-2} GeV^{-1} at 1 TeV. The Cherenkov yield also increases with increasing height due to the decreasing atmospheric absorption, which is why experiments at greater heights above sea level have a lower energy threshold. This is also the main motivation for the new proposal of an IACT array at 5 km height in Chile [Aharonian et al., 2001].

The flux of NSB photons varies greatly with location, on good quality sites it is typically 2 x 10^{12} photons/(m^2×second×steradian) for wavelengths between 300 and 600 nm [Mirzoyan and Lorenz, 1994]. For example, for a telescope with a field of view of 1 degree and a trigger window of 10 ns, the density of NSB photons would be ~ 5 photons m^{-2}. This is much less then the expected value of ~ 65 photons m^{-2} for a 1 TeV gamma ray. So, for this case, a 1 m^2 mirror area would be sufficient to detect 1 TeV showers above the NSB noise; at lower energies though, the Cherenvov signal would quickly fall below a detectable signal (with this mirror), as the following discussion shall show.

The photo-electron Cherenkov signal S, generated by a PMT, can be described as

$$S = \rho_\gamma A\epsilon = y_\gamma E A\epsilon \ , \tag{2.17}$$

where A is the mirror area of the Cherenkov telescope and ϵ the collection efficiency of the system, i.e. the fraction of Cherenkov light that hits the mirror area and eventually creates a photo-electron in a PMT. This factor combines the quantum efficiency of the PMT, the reflectivity of the mirrors and the fraction of light eventually collected by the PMT. For current Cherenkov telescopes, this factor is ~ 0.10.

The noise level N can be expressed in terms of Poisson noise of a background signal S as

$$N = \sqrt{S} = \sqrt{\phi_B \Omega A \epsilon t} \ , \tag{2.18}$$

where ϕ_B is the background photon flux in photons/(m^2s sr), Ω the solid angle subtended by a PMT and t the electronic trigger formation time, the time window in which incoming events are considered as a relevant signal.

Using equations 2.17 and 2.18, one can easily define the required signal-to-noise ratio for the quality of a potential signal detection as

$$S/N = y_\gamma E \sqrt{\frac{A\epsilon}{\phi_B \Omega t}} \ . \tag{2.19}$$

If one defines the energy threshold of an Cherenkov telescope as the minimum energy for which the signal-to-noise is sufficient to trigger the telescope adequately, this threshold energy E_{th} is inversely proportional to S/N, given by

$$E_{th} \propto \frac{1}{y_\gamma}\sqrt{\phi_B \Omega t / A\epsilon} \tag{2.20}$$

This simple approach neglects the wavelength dependence of Cherenkov light and night sky background production and collection. In reality, air shower simulations take into account these integrations, apart from the dependence of Cherenkov light production, as the aforementioned $\eta = n-1$ changes by only 5% over the wavelength range of 300 to 600 nm, the range typically covered by PMTs. Instead, a wavelength-independent n is used, obtained at an effective wavelength [Bernlöhr, 2000].

For a signal to be identified as coming from other than an extreme fluctuation in the background light noise, it became standard for the value of S to be ≥ 5 times N, depending on the configuration of the detector electronics [Weekes, 2003]. As one can see from the two previous equations, to increase the mirror area has a good effect on both the energy threshold and the S/N ratio.

2.4 Effective collection area

Since the radius of the Cherenkov light pool on the ground is ~120 m, the potential shower detection area amounts to $\sim 5 \times 10^4 \mathrm{m}^2$. This is obviously huge by the standards of astronomical detectors, and enables efficient observations in the TeV regime despite the strongly reduced flux compared to the MeV regime of satellite detectors, which have a comparably tiny collection area of at most a square meter. This large area is independent of the mirror collection area, that only determines the minimum γ-ray energy that can be detected as shown before; however, the effective collection area instead is dependent on the energy of the primary particle, and more importantly, on the zenith angle of the observation due to different column depths travelled by the shower. These dependencies make it necessary for a viable energy calibration to create look-up tables from simulations for a number of zenith angles and as a function of energy of the primary, making the analysis process more difficult. Also this emphasizes the importance of atmospheric monitoring again, as a wrong assumption of the atmosphere's transmission leads to a biased effective collection area and subsequently larger errors in energy and flux calculations.

2.5 Stereoscopy

Stereoscopic observations, with telescopes separated by distances of the same order as the lateral spread of the light from the shower, improve significantly the background rejection, energy resolution and the angular resolution of the atmospheric Cherenkonv technique. Multiple images of the same shower offer many advantages, such as (after [Weekes, 2003])

- reduced energy threshold by using coincidence (hardware) trigger schemes between the different telescopes,
- improved hadron discrimination from multiple image characterization,
- elimination of local muon background (as muon events are concentrated on a radius smaller than the average separation of two telescopes in an array),
- location of the shower axis, which improves the energy determination, as the main unknown for a single telescope is the core location; a close low energy event looks similar to a distant high energy event,
- determination of the shower maximum,
- and better angular resolution.

2.6 Experiments

Table 2.1 shows an overview of a selection of the most important γ-ray experiments of the past and future. The Whipple experiment first discovered clearly the Crab nebula as a source of TeV γ-rays and is, after almost 50 years of operation and several system upgrades, still an important experiment today. HEGRA was the pioneer in stereoscopic observations as they are done today with fully independent telescopes of equivalent specifications[3]. The H.E.S.S. experiment is the first of the new generation IACT experiments to be fully operational since January, 2004. This new generation is usually defined by significantly larger mirror areas and superior camera electronics (see next chapter for a more detailed overview of the H.E.S.S. experiment). VERITAS and CANGAROO-III are the main other experiments following the approach of stereoscopic large mirror area IACT systems.

[3]The Durham Mark VI had experimented with stereoscopic techniques to suppress background events, but with 2 subsequent detector generations, creating a shift of sensitivity between different detectors

Existing and planned ACT observatories.

Experiment	Location	Elevation (km)	Collectors	Mirror area (m^2)	Pixels/ camera	Energy (GeV)
Whipple	Arizona, USA	2.3	1	75	467	250
HEGRA	La Palma, Spain	2.2	6	9	271	500
HESS Phase 1	Gamsberg, Namibia	1.8	4	100	960	50
VERITAS-4	Arizona, USA	1.5	4	100	499	50
CANGAROO-III	Woomera, Australia	0.2	4	75	577	50

Table 2.1: After [Weekes, 2003]. References for the experiments: [Whipple Cawley et al., 1990], [HEGRA Collaboration et al., 1999], [H.E.S.S. Hinton, 2004], [VERITAS Weekes et al., 2002], [CANGAROO-III Kubo et al., 2004]

Chapter 3

The H.E.S.S. experiment

In this chapter I will give an overview of the H.E.S.S. experiment and its main instruments, the Cherenkov telescopes. Apart from a short overview section at the beginning, each section is dedicated to the description of one of the main elements of the H.E.S.S. Cherenkov telescope. Much of this chapter and detailed figures of specifications and graphical display have been taken from several publications of the H.E.S.S. collaboration as referenced. The last section briefly describes the auxilliary elements of the H.E.S.S. system, many of which are topics of this thesis, therefore links are given to the relevant chapters at that point.

3.1 Overview

The High Energy Stereoscopic System (H.E.S.S.) consists of four 12 m diameter imaging Cherenkov telescopes, placed in the corners of a square of side 120 m; the system is located in the Khomas Highland region of Namibia, 1.8 km above sea level (23°16′18″ S, 16°30′00″ E, see map in Figure 3.1), approx. one hour car drive from Namibia's capital Windhoek on the Farm Goellschau. The H.E.S.S. telescopes provide very good angular resolution and background rejection capability resulting in a sensitivity of ∼10 mCrab with an energy threshold of around 100 GeV. The current development stage *Phase 1* has been fully operational since January 2004, with an official inauguration on the 28th of September, 2004.

Figure 3.1: The H.E.S.S.-observatory is located near the Gamsberg on Farm Goellschau.

Figure 3.2: Two fully operational (with cameras) H.E.S.S. Cherenkov telescopes (Source: private photograph)

3.2 Mount and dish

The mount and dish are steel structures designed for high rigidity (Figure 3.3). They have an altitude-azimuth mounting with a computer-controlled drive system that rotates on a 15 m diameter rail to enable standard astronomical observations.

It takes between one and three minutes to slew the telescope from the parking position to a sky object. Both azimuth and elevation are driven by friction drives acting on auxiliary drive rails, providing a positioning speed of 100°/min. Encoders on both axes give 10" digital resolution and with additional analogue encoder outputs for monitoring, the resolution is improved by another factor of 2 to 3.

The steel structure weighs 60 tonnes and has a height of 17 m; it was designed by SBP in Stuttgart, Germany, and fabricated by NEC in Windhoek, Namibia, based on production drawings from SCE, Windhoek. The protective red paint of the structure has been manufactured especially for H.E.S.S. as a result of a mini research project to find the best compromise between reflection at night and absorption during the day. A black colour would be best to avoid stray light reflections from the structure into the camera at night, but would heat up the structure too much during the day. A white coloured paint would have the opposite effects, with the red colour being the best compromise. A small optical guide telescope is attached as well to the telescope dish.

3.3 Mirror

The mirror of a H.E.S.S. telescope is composed of 380 round facets of 60 cm diameter (see Figure 3.2); the facets are ground from a glass blank, aluminized and quartz coated, with reflectivities in the 80% to 90% range, and were manufactured by companies in the Czech Republic and in Armenia; their production took about three years and after delivery every mirror is checked in the laboratory for its reflectivity.

The facets are located on a spherically shaped optical support structure with the same radius of curvature as the focal length of the facets (Design of Davies and Cotton [1957]), forming a dish with

- 107 m^2 mirror area,
- 15 m focal length and
- a f/d relation (the *focal ratio*) of 1.2.

Figure 3.3: View of the dish steel structure. Note the size compared to the ~2 m high electronic container at the base of the telescope (the white box).

Figure 3.4: Setting up the camera with 960 pixels in the lab at Laboratoire Leprince-Ringuet (LLR), Ecole polytechnique, Palaiseau, France.

This special arrangement has, for the case of γ-ray-astronomy, major advantages over a classical single-piece mirror used in optical telescopes:

- The weight is much less than a 12 m ground mirror; due to that, it was possible to use a multi-piece steel structure as telescope mount instead of a full steel telescope mount that would have been much more expensive for a 12 m diameter mirror to achieve pointing stability without bending effects[1].

- Not only does the structure cost less but also the total cost of 380 mirror facets is much less than that of a a single-piece mirror.

- The Davies-Cotton design has facet mirrors which are spherical and identical, facilitating fabrication at a reasonable cost and making alignment easy. It also has smaller off-axis aberrations than a parabolic reflector so that it has good image quality out to a few degrees from the optic axis. Its one limitation, that the surface is not isochronous, means that over the reflector a photon arrival time spread of approx. 6 ns is introduced into the light pulse, between photons striking the edge of the reflector and those striking the centre. Paraboloidal mirrors are superior in the time domain, but suffer from an increasingly (towards the edge) detrimental off-axis aberration.

The obvious disadvantage of less optical precision compared to a one-piece mirror does not matter in our case, as the maximal theoretical angular resolution is determined by the pixel size of the PMT and the Davies-Cotton design easily provides a better-than-needed optical precision (see below).

To allow remote alignment of the mirrors, each mirror is equipped with two alignment motors, called actuators (see Figure 3.9), that provide a 'per-actuator' precision of a few microns. The alignment procedure [Cornils et al., 2003] uses the image of a star on the closed lid of the photo-multiplier-tube (PMT) camera, viewed by a CCD camera at the centre of the dish. Due to the good quality of both the mirrors and the alignment system, the on-axis point spread function is significantly better than initially specified [Krawczynski and the H.E.S.S. collaboration, 1999], with a measured spot width of 0.02° (see Figure 3.5).

The imaging quality is stable over the elevation range from 30° to the Zenith, the most common observational range for IACTs. This quality decreases at lower elevations due to weight of the camera of approx. 960 kg which acts on the steel

[1] 12 m is the current scale of the world's largest one piece mirror telescopes.

structure as a massive lever, being attached via long steel masts at the focal point at 15 m.

The point spread function varies with distance θ (in degr.) to the optical axis as

$$r_{80} = \sqrt{0.42^2 + (0.71\theta)^2} \ [mrad]; \tag{3.1}$$

r_{80} is the circle containing 80% of the light of a point source at the height of the shower maximum. Over most of the field of view, light is well contained within a single pixel.

The telescope pointing was verified using the images of stars on the camera lid [Gillessen et al., 2003]. Without any corrections, star images were centred on the camera lid with a rms error of 28". Using a 12-parameter model to correct for misalignments of the telescopes axes etc., a pointing precision of 8" rms is reached. Finally, using the guide telescope attached to the dish for further corrections, the pointing can be good to 2.5" rms. H.E.S.S. should therefore be able to locate gamma ray sources to a few arc-seconds [Gillessen et al., 2003].

3.4 The cameras

The main characteristics of the PMT cameras of the H.E.S.S. telescopes [Vincent et al., 2003] are:

- 0.16° (29 mm) pixel size,
- 5° field of view (ten times the moon's apparent diameter),
- 960 PMT pixels[2] per telescope, covering an area of about 1.4-1.6 m diameter (depending on the angle of measurement, see Figure 3.4).

The complete electronics for signal processing, triggering, and digitization is contained in the camera body; only a power cable and a few optical fibers connect to the camera.

For ease of maintenance, the camera features a modular construction. Groups of 16 PMTs together with the associated electronics for signal processing form so-called *drawers* (see Figure 3.11), 60 of which are inserted from the front into the camera body, and have backplane connectors for power, a readout bus, and trigger

[2]The term *pixel* normally relates to the PMT tube, the high voltage electronics and the connected stabilising electronics.

lines. The rear section of the camera contains crates with a PCI bus for readout, a custom crate for the final stages of the trigger, and the power supplies. In total, the circuitry in the camera dissipates almost 5 kW of electrical power and almost 100 computer-controlled fans serve to control the air flow inside the camera.

3.4.1 The acquisition channels

The camera uses Photonis XP2960 PMTs, with the following specifications:

- amplification over 8 stages (=dynodes),
- borosilicate windows,
- a gain of 2×10^5.

In front of all PMTs is a matrix of light-gathering Winston cones to improve the collection efficiency of Cherenkov light(see Figure 3.6). The PMTs are individually equipped with DC-DC converters to supply a regulated high voltage to the dynodes; for best linearity, the last four of the eight dynodes are actively stabilized.

Each drawer is composed of two acquisition cards, each reading the data from 8 PMTs [Aharonian and the H.E.S.S. collaboration, 2004a]. Each pixel has three main information channels, one trigger channel and two acquisition channels with different gains (see Figure 3.7). The *high-gain* (HG) channel is used to detect signal charges up to 200 photo-electrons (p.e., see also eq. 2.17); the *low-gain* (LG) channel is used to detect charges in the range between 15 to 1600 p.e.

The key element in the signal recording of the H.E.S.S. cameras is the Analogue Ring Sampler (ARS) ASIC, initially developed for the ANTARES experiment [Haller and Wooley, 1993]. The sampling of the PMT signal is performed at a rate of 1 GHz with the analogue voltage levels being stored in a ring buffer consisting of 128 capacitor cells, essentially serving to delay the signal acquisition until a trigger decision is reached.

Following a trigger signal, the sampling is stopped, the capacitor cells of the ARS are read out and digitised with an Analogue to Digital Converter (ADC) with a conversion factor V_{ADC} of 1.22 mV/(ADC count). For normal observation, only 16 cells are used for this conversion into charge equivalent ADC counts. To determine the correct timing offsets for the read-out of the ARSs, a special read-out mode provides the full time profile buffered in the ARS. Figure 3.8 gives an example of data from this *sample mode* run with airshower events, where the time profile of

a Cherenkov event can be seen. This detailed read-out is only done in this mode to determine the timing offsets for the correct read-out after triggering, whereas in the normal read-out mode (*charge-mode*), the 16 samples are integrated to give two ADC values per pixel, one each for HG and LG.

The high-gain channel is sensitive enough to detect single photo-electons and the amplifications are set so, that the number of ADC counts between the pedestal — the mean ADC value recorded in absence of any Cherenkov light — and the signal from a single p.e. is ≈80 for a PMT gain of 2 x 10^5. This has been chosen such that the single p.e. peak can be clearly distinguished at the normal pixel operating high voltage (HV).

3.4.2 Calibration parameters

For a standard Cherenkov analysis using Hillas parameters, the signal amplitude is the essential image building parameter. Also, the camera trigger scheme uses the amplitude to decide if a Cherenkov event has been detected or not. This amplitude is the charge in p.e. induced by this light on the PMT. The elaborate calibration procedures that have been developed for the H.E.S.S. cameras provide the required conversion coefficients from ADC counts to corrected photo-electrons.

For each triggered event, ADC counts are measured in both data channels of the acquisition card, ADC^{HG} for the high-gain channel and ADC^{LG} for the low-gain channel. The calculations to be done to receive an amplitude measured in p.e. for both channels, are:

$$A^{HG} = \frac{ADC^{HG} - P^{HG}}{\gamma_e^{ADC}} \times FF \tag{3.2}$$

$$A^{LG} = \frac{ADC^{LG} - P^{LG}}{\gamma_e^{ADC}} \times \frac{HG}{LG} \times FF \tag{3.3}$$

where

- P^{HG} and P^{LG} are the ADC value of the base-line for the high-gain and low-gain channels respectively, commonly called the *pedestal* values,
- γ_e^{ADC} is the gain of the HG channel in ADC counts per photo-electron,
- HG/LG is the amplification ratio between the two acquisition channels and
- FF is the flat-field coefficient.

The flat-field coefficient corrects for different optical and quantum efficiencies between pixels within a camera (see chapter 4).

For the image analysis and the trigger decision, both A^{HG} and A^{LG} are used to provide a single amplitude per pixel. Provided that both gain channels function properly, the HG value alone is used up to $\approx$ 150 p.e. and the LG value beyond $\approx$ 200 p.e. For intermediate values, one calculates a weighted average of the HG and LG values with a photo-electron amplitude given by:

$$A = (1 - \epsilon) \times A^{HG} + \epsilon \times A^{LG} \tag{3.4}$$

where $\epsilon \approx (A^{HG} - 150)/(200 - 150)$.

To summarize, the calibration procedure must provide pedestal positions for both channels, the high-gain value γ_e^{ADC} and the ratio of the HG to the LG. As the flat-fielding coefficients do not depend on the electronics, but on optical and quantum efficiencies, they are calculated per pixel and not per amplification channel.

3.4.3 Pedestal values

The *pedestal position* (or pedestal value) is defined as the mean ADC value recorded in the absence of any Cherenkov light. Part of this pedestal is a so called *dark* pedestal value, where electronic noise creates a Gaussian ADC distribution whose mean is the pedestal position.

These dark pedestal values, measured with the camera lid closed, have a dependence on camera temperature, which varies between 20°C and 40°C depending on the season and the weather, with the typical variation during one observation run of 28 minutes time being of the order of 1°C. Because this drift can result in shifts in the ADC counts as large as -50 counts/degree [Aharonian and the H.E.S.S. collaboration, 2004a], pedestal positions for observation runs are being determined approximately every minute to achieve the required precision of $\ll$ 1 p.e. As a shower image contains typically only 20 pixels, real triggered events are used to measure pedestals with pixels containing Cherenkov light being rejected for this calculation (see section 3.5). Additionally, during observations, the pixels are illuminated by night-sky background (NSB) photons, greatly increasing the width of the possible pedestal values. In normal operation, there is over 1 p.e. of NSB per readout window. But due to the capacitive coupling of the PMT signals to the ARS and a cancelling effect between the photoelectron pulses from the NSB and an electronic overshoot

of opposite polarity [see Aharonian and the H.E.S.S. collaboration, 2004a, section 4.2], the pedestal position remains constant in the usual NSB range in Namibia. The shape of the pedestal distributions though are widened according to the rate of NSB in the camera.

3.5 The multi-level trigger

First one could distinguish mainly between a local telescope trigger and a system coincidence trigger with the requirement of two or three telescopes triggering within a certain time. But on closer inspection, the telescope trigger can be split up in a physical and a logical part, summing up to three levels of trigger control overall.

First, the pixel comparators generate a pixel trigger signal, if the pixel amplitude exceeds a *pixel threshold* value; the length of this signal corresponds to the length of time the input signal exceeds the threshold. The camera trigger is formed by a multiplicity coincidence within overlapping *sectors*, each containing 64 pixels (in a 8×8 pixel group); the trigger occurs if the signals in M pixels within a sector (*sector threshold*) exceeds the pixel threshold within a certain time. The time-window for the multiplicity is dictated by the minimum integrated charge over a programmable threshold. For a typical PMT pulse shape the effective trigger window is (1.3±0.14) ns. This narrow gate is possible, because the PMTs are calibrated for the same gain and then sorted within the camera by the high-voltage they need to achieve this gain. This sorting minimises the time dispersion introduced by different PMT transit times, with the effect that this narrow multiplicity gate guarantees maximum NSB suppression.

The sector and pixel thresholds are programmable and have been thoroughly tested to find the most efficient setup of the trigger logics (see Funk et al. [2005]). Currently, normal operation of H.E.S.S. is using a sector threshold of a 2.5 pixel coincidence with a 4 photoelectron pixel threshold; this configuration is stored, amongst many other configurational details, in the H.E.S.S. database, an SQL database for storage of monitoring and configuration details of observation and calibration runs.

The third level trigger is a central trigger system (CTS) controlling electronic delays and implementing a coincidence logic within the four telescopes of H.E.S.S. phase 1. In the standard setup of the telescope system, the CTS combines the trigger information of all participating telescopes and generates a *system trigger* if the minimum number of telescopes (typically two) report a local trigger within a

time-window of 10–100 ns duration. Only system trigger data are eventually read out.

The telescopes use a buffer where they can store data from a local trigger, so that readiness to take new data can be achieved while generating the full event data, because no system trigger might occur, in which case, readiness has to be attained as fast as possible. When a local telescope trigger occurs, the telescope immediately starts to read-out the data, which takes about 270 μs; but to keep dead-times low, this read-out can be interrupted with a reset signal during the first 10 μs, if no system trigger arrives within approx. 5 μs (another 5 μs as safety margin).

As the telescope is ready to take data again, before the full read-out and transfer of data is completed, it can happen that a new local trigger occurs and is sent away to the CTS, before full event data generation is completed. Because this telescope would not be able to read-out this new event in case a system trigger is generated, any telescope trigger information provides the current read-out status as well (in form of a *busy* or *active* flag), in which case the CTS will not send a read-out but a *count* command, should a system trigger occur while a telescope has announced that it is busy. This way the dead-times can be accurately measured to deduce a true rate from the mere data-acquistion rate.

This system allows the imposition of arbitrary telescope configurations in the trigger, and the operation of the telescopes either as a single four-telescope system, or as subsystems, up to four individual telescopes pointed at different objects .

3.6 Additional elements

A number of auxiliary instruments are used to monitor telescope performance and atmospheric quality (discussed in detail in the following chapters). At the centre of each dish, a LED pulser provides for flat-fielding of the cameras [Aye et al., 2003]. Until recently, on the first telescope in operation, a laser pulser system was installed, which is described in detail in chapter 4. This system has been replaced now by a LED pulser system.

Another LED pulser installed in the camera delivers single photoelectrons to each PMT for gain calibration. For atmospheric monitoring, each telescope is equipped with an infrared radiometer operating between 8 and 14 μm to detect atmospheric water vapour along the line of sight (discussed in detail in chapter 5). There is also a LIDAR system, to detect clouds and characterize aerosol scattering, and a weather

station on site, that will be discussed in detail in chapter 6.

Also on site is the ROTSE 3c telescope [ROTSE]. This is a 0.45 m diameter optical telescope, primarily designed for the optical identification of gamma ray bursts; some time is available to H.E.S.S. for the optical monitoring of gamma ray sources.

3.7 Data acquisition (DAQ)

The H.E.S.S. DAQ system [Borgmeier et al., 2003] is built as a distributed computing system[3] running simultaneously on multiple nodes of a linux cluster installed on the observatory site. The H.E.S.S. cameras have their own computers onboard and are connected via optical fibre cables to the main computer system in the control building.

Online monitoring devices are considered as a constant incoming data stream. When an observation run is taken, a run-number is created and run-related monitoring is created as a time-restricted split-off copy of that constant incoming stream. That way it is possible to obtain run-related data while having uninterrupted 24 hour monitoring data as daily recorded runs. This procedure enables standard analysis software schemes that are based on run-number ordering, while still having the wealth of data of 24 hour atmospheric monitoring that can be analysed separately to obtain e.g. repeating weather patterns.

[3] using the industry standard CORBA

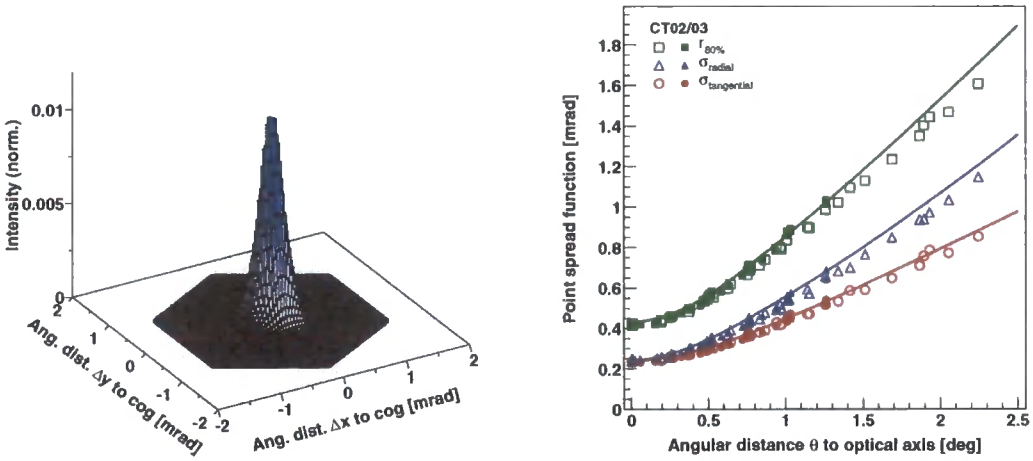

Figure 3.5: Left: The on-axis point-spread function (PSF) of CT3 (the first telescope) compared with the pixel size (hexagon). Right: the behaviour of the PSF off-axis for telescopes CT2 & CT3; solid lines show Monte-Carlo predictions [taken from Hinton, 2004].

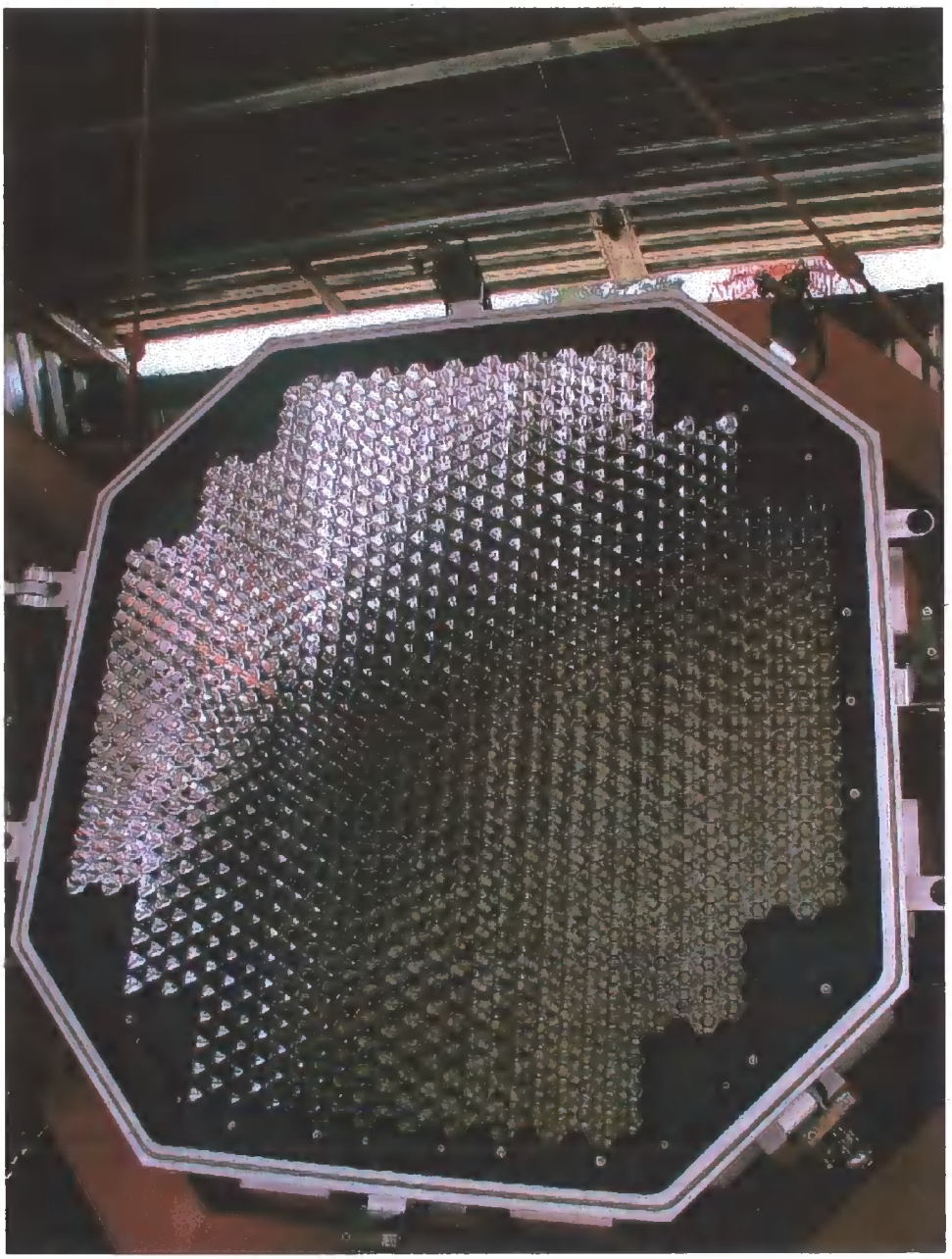

Figure 3.6: The front of the camera with its lid open, showing the PMTs and the Winston cones [taken from Hinton, 2004]. If one looks closely, one can see the surface of the PMTs in between the shiny aluminium Winston cones.

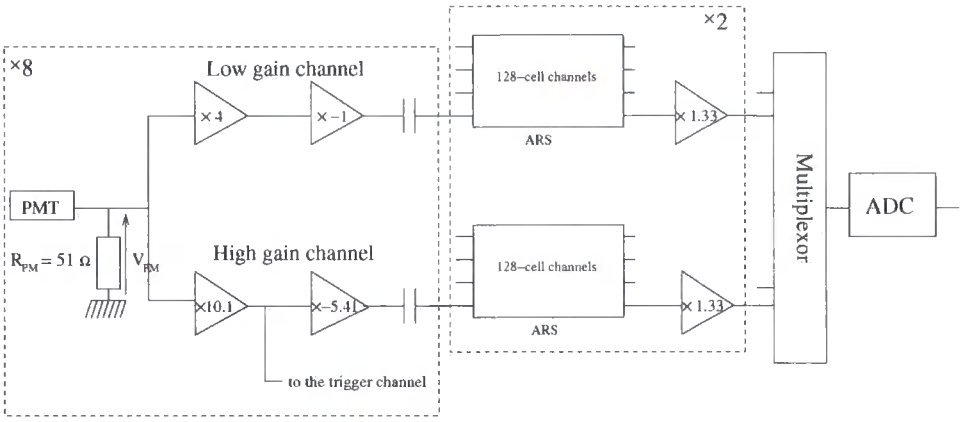

Figure 3.7: Schematic illustration of the electronics of one acquistion card for 8 PMTs [taken from Aharonian and the H.E.S.S. collaboration, 2004a, calibration paper].

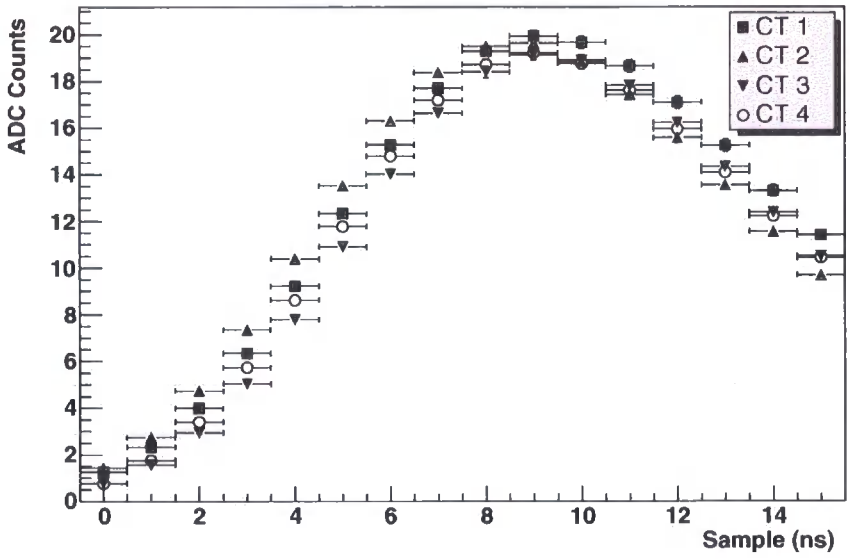

Figure 3.8: Mean signal samples over high-gain channels for the four operating cameras for air-shower events [taken from Aharonian and the H.E.S.S. collaboration, 2004a, calibration paper].

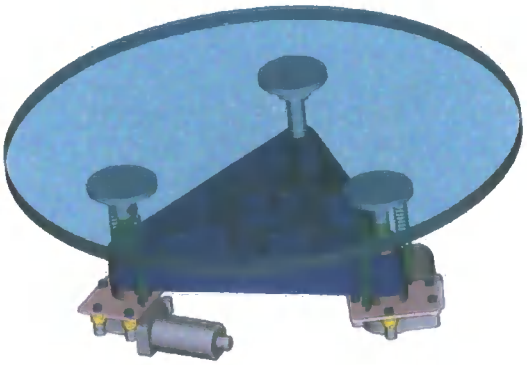

Figure 3.9: One mirror actuator module for precise positioning of the single mirror elements of one Cherenkov telescope. The motors for the actuators were originally designed for use on motor vehicle windows.

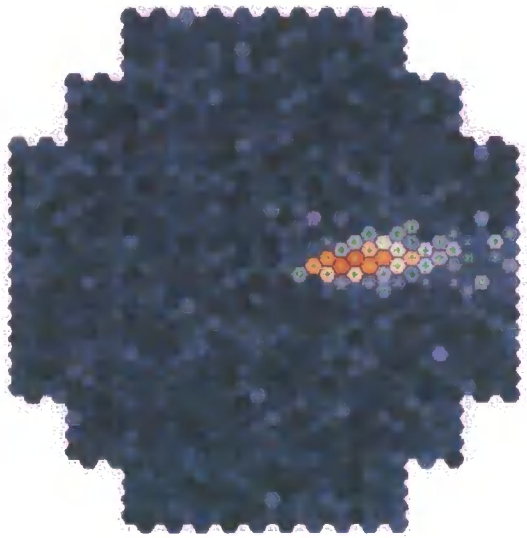

Figure 3.10: A gamma-ray event seen in a 'picture' taken by a H.E.S.S. camera.

Figure 3.11: One drawer containing 16 pixels. 60 of these drawers are used to build one H.E.S.S. camera.

Chapter 4

Flat-fielding unit

This chapter will discuss the first flat-fielding unit that was built for the first operating H.E.S.S. telescope. After an introduction, I will describe the general setup in section 4.2. This is followed by a short section 4.3 describing some of the hardware used. Section 4.4 describes the process for finding the best fibre cable for our purpose. Then I will talk about the two possible layouts of the proposed system that we considered, with a more simpler solution sketched out in section 4.5 and a more sophisticated possibility described in section 4.6. The last section 4.7 talks about the possible modes of usage of the flat-fielding system.

4.1 Introduction

For a reliable extraction of Hillas parameters (as mentioned in section 2.3) from a camera image based on raw PMT data it is essential to calibrate accurately the PMTs and the electronic response of the system. To achieve this, elaborate calibration procedures have been developed that are well described in the H.E.S.S. publication about the calibration of the H.E.S.S. cameras [Aharonian and the H.E.S.S. collaboration, 2004a]) and have been briefly summarised in section 3.4.2. Two independent calibration schemes are available and are in good agreement.

Though, despite the best efforts to calibrate the electronic chain (summarized in section 3.4 and 3.4.2), different PMT photocathode efficiencies and different Winston cone light collection efficiencies produce inhomogeneities in the camera, resulting in a slightly different PMT response to a uniform illumination [Bernlöhr et al., 2003]. It is obvious that for a correct operation of trigger criteria and for the following analysis, these differences have to be dealt with. In other words, the image of the

camera should be as 'real' or correct as possible. To have the image as real as possible all 'eyes' of the cameras, the pixels, have to 'see' the same, meaning the electronic gain of all pixels have to be corrected for these differences, a process known as *flat-fielding*, resulting in the aforementioned (section 3.4.2) flatfield coefficients.

Several major facts must be taken into account to build a flat-fielding device that recreates an event for the camera that resembles an event produced by a cosmic particle:

- the pulse length of the Cherenkov light is about 3–5 ns,
- significant amount of light from the Cherenkov light spectrum starts at about 200 nm and goes up to 700 nm with its maximum around 400 nm, depending on the energy of the primary particle (see Fig. 4.1),
- the PMTs Photonis XP2960 [Photonis, 2003] used by H.E.S.S., start to be sensitive at about 250 nm, but their peak of sensitivity is around 400 nm (see Fig. 4.2),
- the telescope mirrors have a reflectivity over 70% at 300 nm, increasing to mostly over 80% at 400 nm (see Fig. 4.3).

These factors determine that for testing the camera's response appropriately a very short signal with a relatively broad spectrum maximizing around 400 nm is required. One standard approach to these requirements is to use a pulsed UV-laser to energise a piece of scintillator. The scintillation light is then diffused to produce a homogenous light field for illumination of the camera. This solution has been used on many gamma-ray telescopes, e.g. the HEGRA telescope system or the Durham Mark VI telescope (see e.g. Aharonian et al. [1999, section 2]).

One may wonder now why we need to take into account the time profile of the Cherenkov light for adjusting the electronic gains. While it is obvious, that light of different wavelengths results in different photo-electron probabilities, why must the camera be tested with a pulse of approximately the same width as the real events?

Firstly, with a light-flash as short as the real event we are able to test the whole read-out chain of the telescope. Were the probing light flash to be very slow compared to the real events, then we would never 'stretch' the read-out electronics to high frequency values where we really need to test the reliability of the read-out chain, and any electronic device working well at a signal bandwidth of 1 MHz might not be working as well at hundreds of MHz.

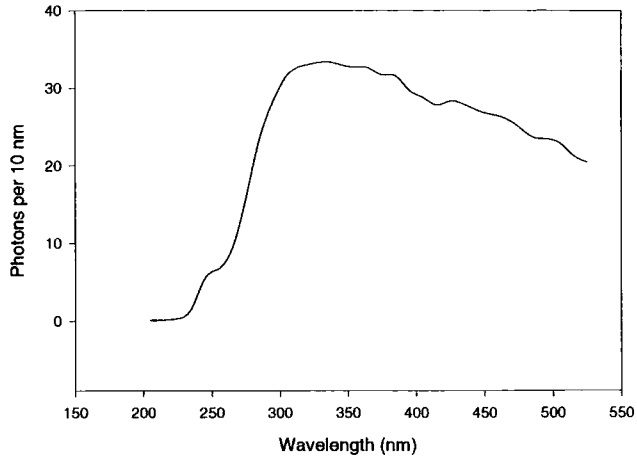

Figure 4.1: The Cherenkov spectrum of 1 TeV γ-rays at a height of 1800 m above sea level (height of the H.E.S.S. observatory), from Monte-Carlo simulations

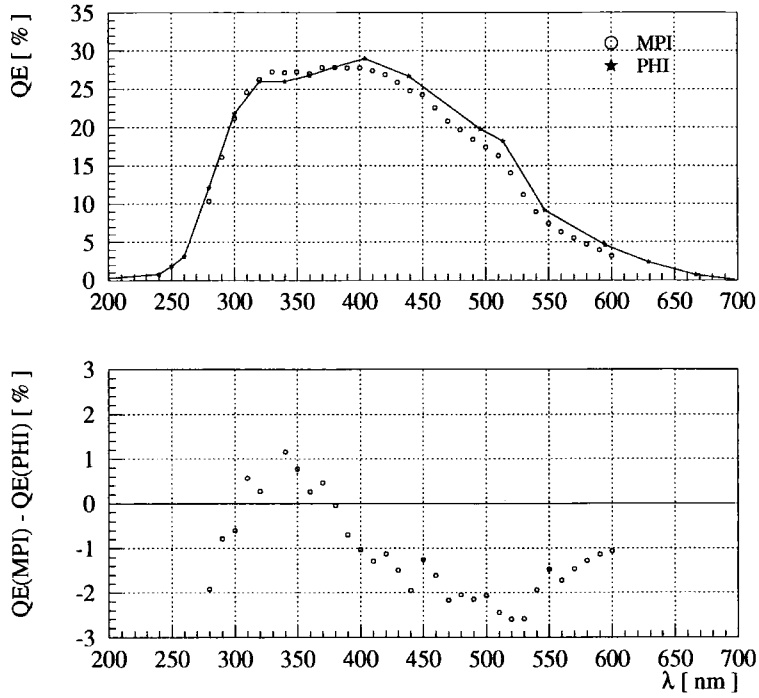

Figure 4.2: The quantum efficiency of the H.E.S.S. photomultiplier Photonis XP2960, averaged over four units, measured by the MPI Heidelberg and compared with data from Photonis (PHI in the plot)[Koch and Kohnle, 2001].

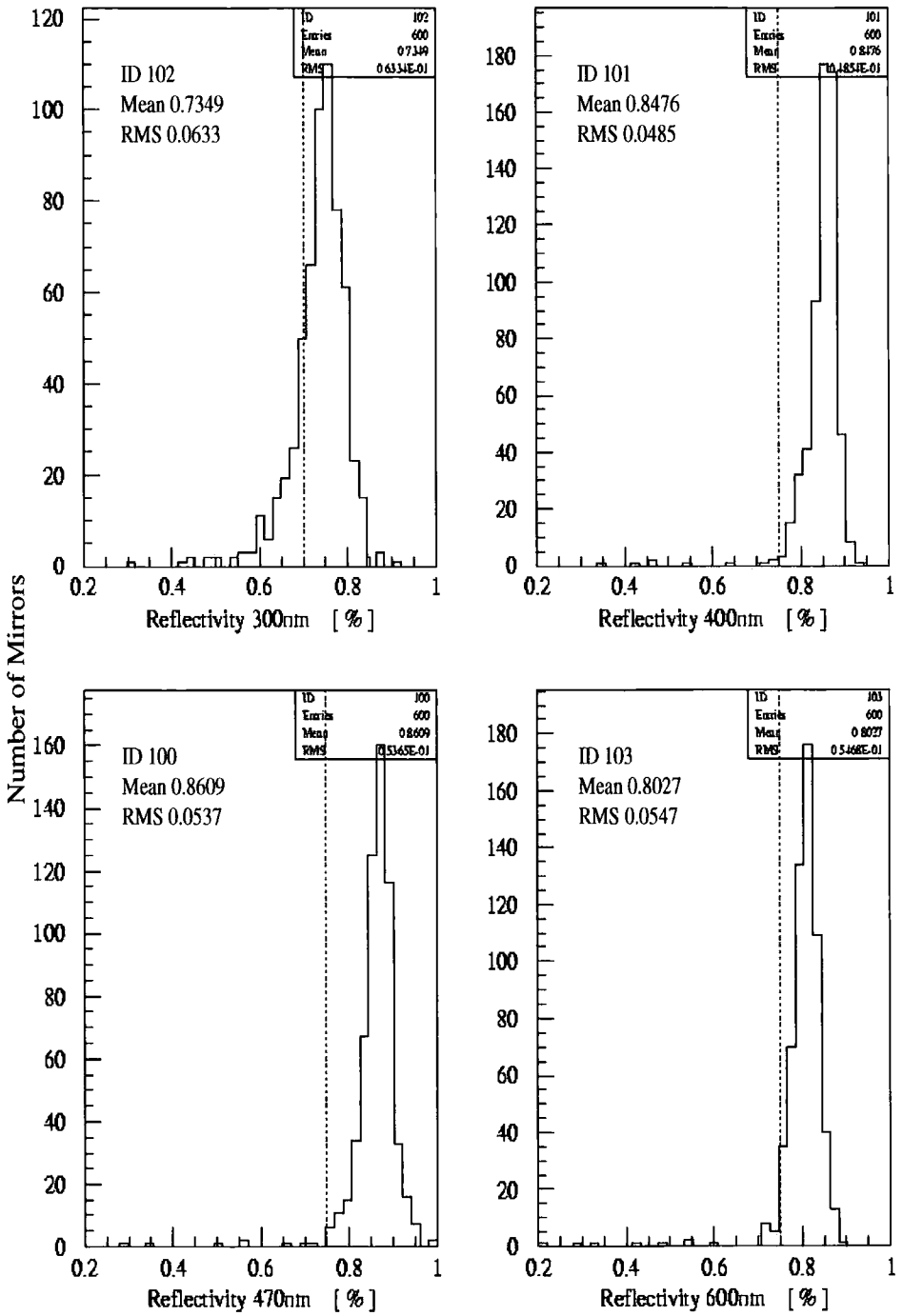

Figure 4.3: Reflectivity of the H.E.S.S. mirrors of the manufacturer Compas as measured by a collaborator in Heidelberg [Rowell et al., 2000]. The histograms have 600 measurement entries, the y-Axis shows the number of mirrors with the respective reflectivity.

Secondly, the adjustment of the electronic gain of a PMT during operation can only easily be managed via the high-voltage (HV) level. This should be done at the signal bandwidths of real events, because every PMT behaves differently to a change in HV. So, if a flat-fielding were to be performed at small signal bandwidths, the camera might not be 'flat' at the bandwidths of real events.

4.2 General setup

Generally, a flat-fielding setup can be separated into the following sub-units in order to optimize each step in the production of the flat-fielding light (see also Fig. 4.4):

- The light-source, a UV-laser with very short pulse capabilities to simulate the time profile of real cosmic-ray events and a duty-cycle as high as possible to allow testing the read-out chain with a repetition rate as high as possible.
- A piece of scintillator, energised by the UV-laser; the scintillator flash is wavelength-shifted and spread compared with the narrow-band laser pulse, to simulate the Cherenkov spectrum.
- A set of remote-controlled filter-wheels with colour and intensity filters to provide a choice of wavelength and intensity for flat-fielding data runs.
- A diode in the optical path for self-monitoring of intensity and pulse-form of the flat-fielding light.
- A diffuser to illuminate the camera as uniformly as possible.

Now with a large dish such as those of the H.E.S.S. telescopes, for ease of maintenance it seems to be a good approach to have the main devices like the UV-laser that need regular maintenance on the ground instead of mounting them into the dish of the telescope illuminating the camera directly. Additionally, it is advisable to keep the laser with its high voltage system in a dry closed cabin rather than exposed to the elements on the dish. Therefore the additional, and unfortunately complicating, element of the flat-fielding unit is a fibre-optic cable (hereafter fibre) to transport the light to the dish where the light will be projected onto the camera.

The optical fibre is a complicating element for two reasons. Firstly, the light it must transport is in a wavelength region where the attenuation in fibres is very high and rarely known even by the manufacturer, as most fibre-optic devices are

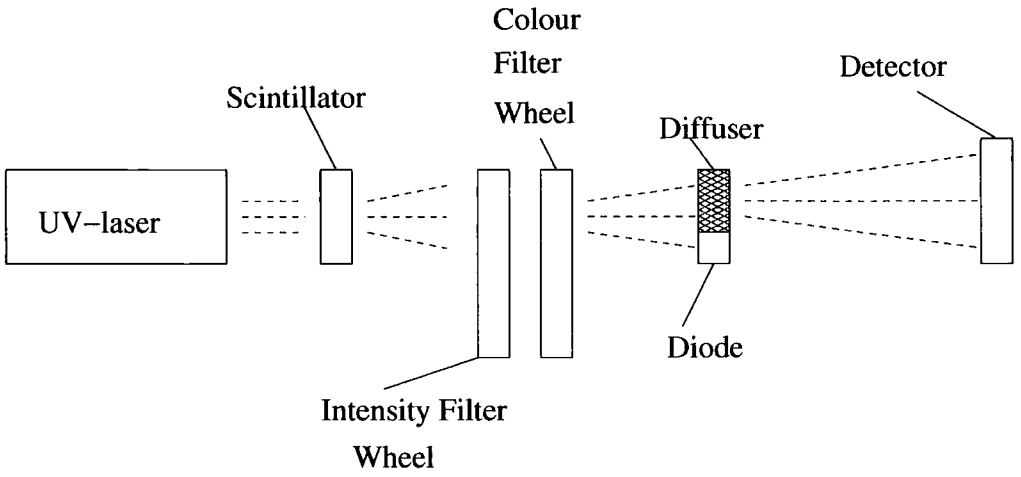

Figure 4.4: General setup of a flat-fielding system.

produced for the telecommunication industry where infrared light is used. Secondly, the pulse broadening which inevitably happens in a fibre due to modal distortion, is in direct opposition to the requirement for a short-pulsed flat-field light. These two facts were less important in previous experiments because the fibres were shorter because the size of the telescopes was smaller than the H.E.S.S. telescopes. Now, due to the bigger telescopes, we have two points in the 'flat-fielding chain' where the situation demands more scrutiny:

- Compared to older experiments, the increased focal length of 15 m means we need more light at the centre of the dish for a comparable illumination of the camera due to the r^{-2} loss of photon flux.
- The bigger telescopes result in a bigger distance for the fibre from an accompanying electronic hut to the dish centre, meaning that the light attenuation and pulse spreading due to the fibre become crucial factors. In previous experiments these distances were several metres (e. g. $\sim$8 m at the Durham Mark VI telescope); now the cable length between the dish centre and the electronic hut is $\sim$50 m.

Therefore a significant amount of research had to be invested into determination of the best choice of fibre in terms of light attenuation and pulse broadening. This will be discussed in detail in section 4.4.

In the following sections I will describe the different parts of our flat-fielding solutions, possible design layouts that have been considered and the eventual solution

that has been constructed and installed on the first operational H.E.S.S. telescope.

4.3 Hardware

4.3.1 UV-laser

The light source chosen is a high power pulsed N_2-Laser model VSL-337ND-S from Laser Science, Inc.^{TM}[Spectra Physics, 2001] with the following specifications (taken from the manufacturer's manual):

- Wavelength: 337.1 nm
- Spectral bandwidth: .1 nm
- Repetition rate: Internally triggered 0-30 Hz, externally 0-60 Hz
- Pulse width (FWHM): < 4 ns
- Pulse energy: > 300 μJ
- Pulse to pulse energy stability @ 10 Hz: $< 3.5\%$, standard deviation as a percent of mean
- Peak power: > 75 kW
- Average Power: > 7.2 mW @ 30 Hz

Although there were lasers on the market at the time of choosing with shorter pulse lengths, this laser is the best compromise in terms of size, maintenance requirements and cost.

4.3.2 Scintillator

The UV light of the laser now illuminates an organic scintillator that reemits the exciting incoming light shifted and spreaded in wavelength. After comparison of several types, the scintillator chosen was the 'Premium Plastic Scintillator' BC-418 from Bicron Organics [Bicron Organics, 2003] with following specifications:

- Refractive Index: 1.58
- Rise Time: 0.5 ns
- Decay Time: 1.4 ns

- Pulse Width(FWHM): 1.2 ns
- Wavelength of max. Emission λ_{max}(see Fig. 4.5): 391 nm.

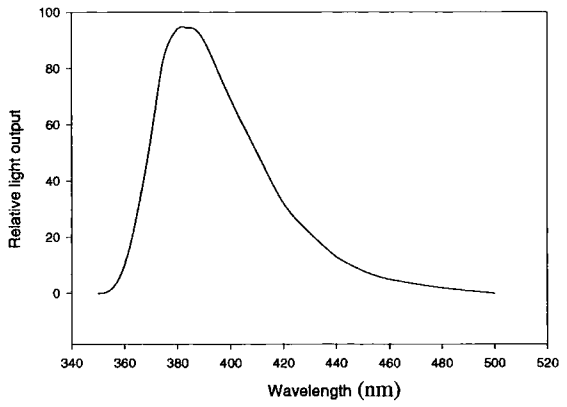

Figure 4.5: Spectrum of plastic scintillator BC-418 from Bicron

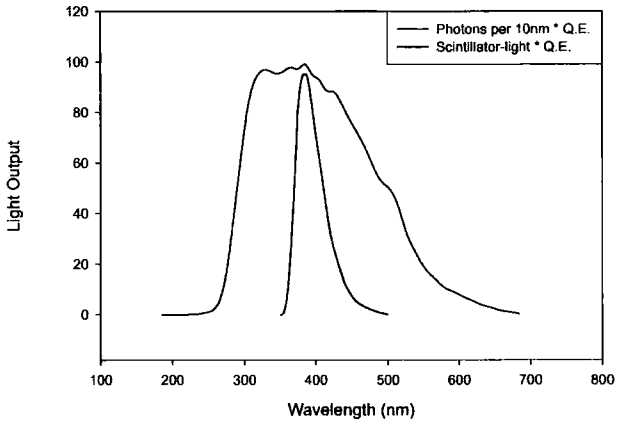

Figure 4.6: Comparison of Cherenkov spectrum with scintillator after folding with PMT quantum efficiency; Y-axis is scaled in arbitrary units

From these specifications a pulse width of about 5 ns from the scintillator could be expected if it were illuminated directly with the UV-laser. Our comparison tests were concerned with the timing, the overall light output and the position of λ_{max} of different scintillators and this particular one from a new production line of the

manfacturer was in all these parameters better than one used in previous Durham experiments.

It is important for the following discussion to notice that the emergent scintillation flash is spherical in its geometry. This represents an important complicating factor for the situation in which one wants to introduce that spherical light flash into a fibre-optical cable. This will be discussed in more detail in section 4.4.

Fig. 4.6 shows the Cherenkov spectrum from Fig. 4.1 folded with the quantum efficiency of Fig. 4.2, compared with the spectrum of the scintillator from Fig. 4.5 folded with the same quantum efficiency. As one can see, the covered integral area of the scintillator spectrum is much smaller; however, the peak sensitivity of the PMTs is covered. So far, there is no scintillator known which could cover a much broader range of wavelengths while maintaining a short enough de-excitation time of a few nanoseconds.

4.4 Choice of fibre

In transporting a relatively short light pulse with a fibre, two issues must be addressed:

- The attenuation in the fibre at the wavelengths of our interest (Fig. 4.6) is much higher than in the windows of low attenution around 0.8, 1.05 and 1.4 micron where the more usual communications applications work (see Fig. 4.7).
- Due to distortion, the pulse broadening is quite significant after any distance ≥ 20 m.

4.4.1 Fibre basics

Materials

Essentially, there are three varieties of optical fibres available today. All three varieties are constructed of either glass, plastic, or a combination of glass and plastic. The three varieties are:

- Plastic core and cladding
- Glass core with plastic cladding (often called PCS fiber, plastic-clad silica)
- Glass core and glass cladding (often called SCS, silica-clad-silica)

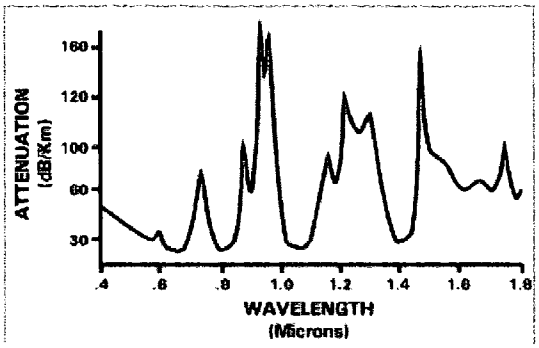

Figure 4.7: Typical attenuation in fibres

Plastic fibres have several advantages over glass fibres. First, plastic fibres are more flexible and consequently more rugged than glass. They are easy to install, can better withstand stress and are less expensive[1]. Also their numerical apertures (see below) and diameters can be made larger than those of glass fibres, which makes them an efficient light collector in the case of an incoherent spherical light source. These factors make plastic fibres an ideal candidate for installation on a telescope where the fibre is exposed to mechanical stress and the elements. The disadvantage of plastic fibres is their high attenuation characteristic; they do not propagate light as efficiently as glass. Consequently, plastic fibres are limited to relatively short runs.

Fibers with glass cores exhibit low attenuation characteristics. However, PCS fibres are slightly worse than SCS fibres. SCS fibres have the best propagation characteristics and they are easier to terminate than PCS fibres. Unfortunately, SCS cables are the least rugged. Also, when being exposed to UV radiation of the sun, these fibres are more susceptible to an increase of attenuation, caused by UV degradation.

Total reflection

The important effect inside fibres is the total internal reflection of light produced by the difference in spectral indices between the core and the cladding of a fibre. Following Snell's law for refraction, $n_1 sin\theta_1 = n_2 sin\theta_2$, with n_1 and n_2 the refractive indices of two media and θ_1 and θ_2 the incident and outgoing angles of light being

[1] and weigh approximately 60% less than glass, but not an issue in our case.

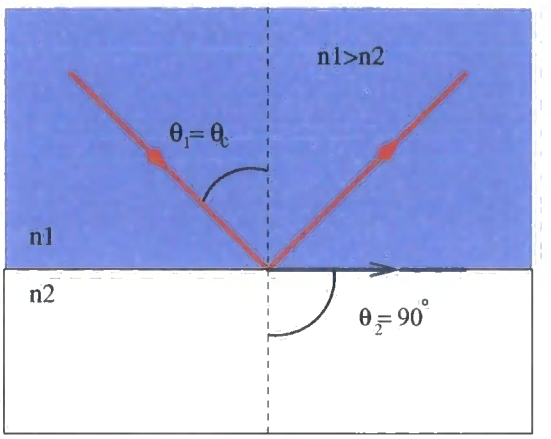

Figure 4.8: At incident angles greater than the critical angle $\theta_1 = \theta_c$ the refraction angle θ_2 would become greater than 90°and total reflection occurs.

refracted at the interface of these two media. Total reflection occurs at this interface when the sine for the refracted beam would have to become greater than unity to fulfil Snell's law. Therefore the critical angle of incidence θ_c for total reflection to occur is 90° for θ_2 (see Fig. 4.8), resulting in

$$sin\theta_c = \frac{n_2}{n_1}. \tag{4.1}$$

On the other hand this equation also determines the *angle of acceptance* for any light introduced into the fibre. When the incident angle is larger then the *cut-off angle* — which is $(90° - \theta_c)$ as one can derive from Fig. 4.11 — then the light is refracted into the cladding instead of being reflected back into the fibre's core. This important parameter for fibres is called *numerical aperture* of the fibre and can be written as

$$NA = \sqrt{n_1^2 - n_2^2}. \tag{4.2}$$

provided the fibre's tip is surrounded by air. Typical values of NA lie around 0.2, which corresponds to angles of acceptance around 8° for a silica glass (SiO_2) fibre with a core refractive index of 1.5. Plastic fibres however often show much greater angles of acceptance, up to 50° and more, due to their generally larger numerical apertures.

From eq. 4.1 one can see that the refractive index of the cladding has to be smaller than the index of the core to provide total internal refraction for light travelling through the fibre. Indices often found in fibres are around 1.45 for the cladding and

1.5 for the core of an silica glass fibre. However, there are two ways how to provide the required change in refractive index.

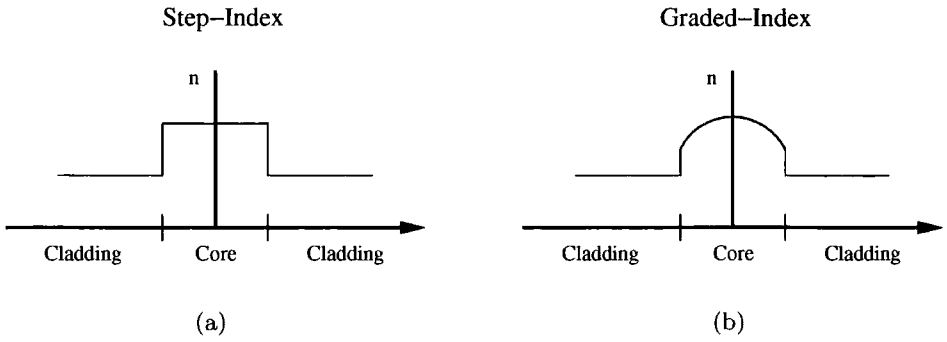

Figure 4.9: The change of the refractive index follows a step function in step-index fibres whereas it changes smoothly in graded-index fibres.

Step-index fibres have a core with uniform index of refraction right up to the cladding interface, where the index changes in a step-like fashion (see Fig. 4.9(a)). The core of a graded-index fibre (Fig. 4.9(b)) has an index of refraction that radially decreases continuously in a parabolic way from the centre to the cladding interface. As a result, the light travels faster at the edge of the core than in the centre [Photonics] which suppresses the pulse spreading described in the next paragraph significantly and changes the travelled optical path like shown in Fig. 4.10. This effect can e.g. increase the bandwidth of a fibre in communication applications from around 20 MHz to 1 GHz.

Pulse spreading or distortion

Basically two effects cause a light pulse spreading inside a multi-mode fibre, intra-modal and inter-modal distortion[2]. The intra-modal distortion is caused by differences in the travel time of modes due to their different wavelengths. Therefore this describes a dispersion effect, which might have been important here as a scintillator flash with a certain bandwidth in wavelengths is to be transported (Fig. 4.5). However, measurements with different colour filters showed that this effect is negligible over the modal distortion; e.g. over a fibre of 100 m length differences in pulse widths

[2]These effects are often imprecisely called dispersion. However, dispersion is a wavelength-dependent process, therefore only the intra-modal effect is a true dispersion, unnecessarily often called *chromatic dispersion*

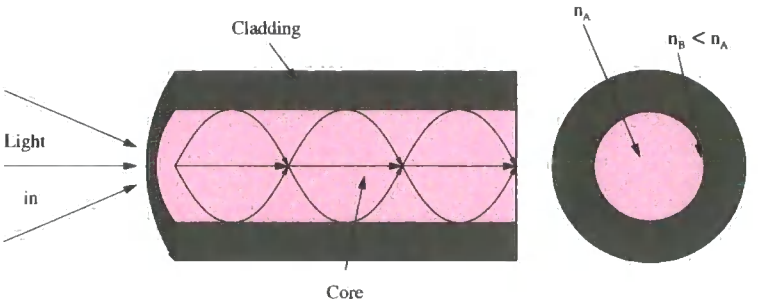

Figure 4.10: Optical path and refractive index layout in graded-index fibres. The refractive index decreases continuously from the centre towards the cladding interface.

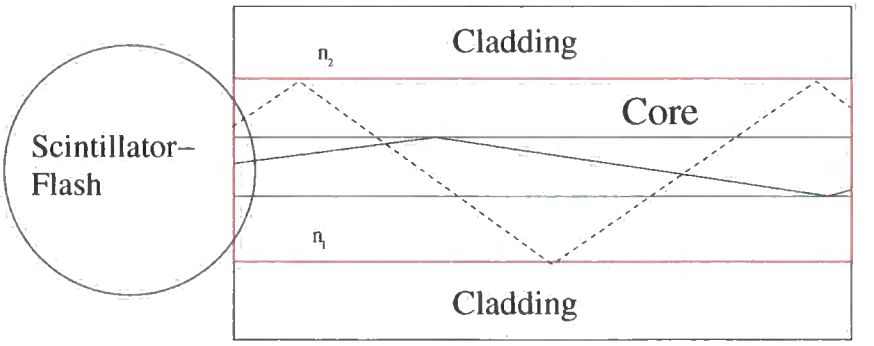

Figure 4.11: The spherical scintillator flash is captured by the optical fibre. Sketched are two optical fibres with two different core radii in red and green. Total reflection occurs due to the difference of refraction indices $n_1 > n_2$ between core and cladding. The optical path length is longer in the case of the red fibre; however, less light can be introduced into the green fibre due to its smaller radius.

between red, green and blue pulses were never greater than 1 ns, whereas from fibre to fibre these differences can be many nanoseconds due to modal distortion, depending on the length of the tested fibre.

Modal distortion is a purely geometrical effect of different optical path lengths for the modes of light due to different entrance angles and resulting differences in the group velocities of the modes[3]. As shown in Fig. 4.11, the larger the incidence angle of the wavefront to the fibre axis, the larger the overall distance the light has to travel to reach the end. This effect can be compensated for by the use of graded-index fibres where the group velocity is higher near to the cladding compared to the axis of the fibre due to the reduced refraction index (see Fig. 4.9(b) and Fig. 4.10).

[3] *Modes* are the different solutions to the wave equation

Multimode vs. Singlemode

Singlemode fibres are mostly used when coherent light e.g. from a laser is to be introduced into a fibre. This light is emitted in a single mode and can be focused so that it can be introduced into very small diameter fibres. These fibres have a very small numerical aperture and very small pulse distortion.

Multimode fibres are used when the light source is incoherent like LED emission. They allow more light to be introduced into the fibre, but have the disadvantage of modal distortion. These fibres would be chosen here for the transport of scintillator light due to its incoherent nature.

Attenuation

The main reasons for light attenuation in a fibre are absorption and scattering. Attenuation is measured in dB/km as

$$AT = \frac{10\,log\left(\frac{P_{in}}{P_{out}}\right)}{L(km)} \tag{4.3}$$

In modern fibres, although the absorption and scattering due to impurities or OH^- ions have been reduced very much due to improved manufacturing processes, one cannot escape the Rayleigh scattering proportional to λ^{-4} which poses the biggest problem here considering that either the UV-laser light or the scintillator flash at around 400 nm has to be guided through a fibre.

There are also losses due to bending effects, both on a micro- and macroscopic scale. The microbending loss is caused by tiny imperfections in the surface of the fibre of the dimension of several wavelengths which produce perturbations in the electro-magnetic field. Bending of the fibre on larger scales, either due to an imperfect spooling process or due to mechanical bending of the fibre during usage, causes light to be lost into the cladding at the next interaction with the cladding/core interface because its angle of incidence has become smaller than θ_c. However, these losses are negligible compared to the loss due to Rayleigh scattering in the UV.

Now taking into account the problem of coupling enough light into the fibre, the light throughput and pulse width of the light pulse are competing. As mentioned before, the scintillator flash is spherical in its nature and therefore coupling light from this flash into a thin fibre is not easy. A bigger numerical aperture or simply a bigger diameter makes it easier to couple more light into the fibre, but as the

dispersion is mainly modal in character, one experiences also a broader pulse in this case.

4.4.2 The testbed

The setup for testing the fibres changed in several details over time, striving to increase the light output. The target intensity to achieve was that it should be possible to saturate the PMTs in the telescope camera in order to have sufficient dynamic range remote-controllable by optical density filters. By comparing the distance between PMT and diffuser in our setup with the distance between camera and centre of the dish of the telescope we were able to estimate the amount of light we had to create in our setup to achieve this target intensity on the telescope. One possibility that had been considered is to use a professional UV-laser coupling

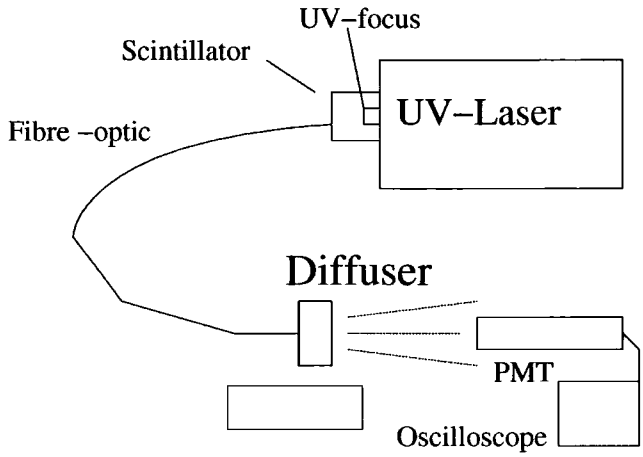

Figure 4.12: Setup for testing of fibre sample

system for the introduction of the laser light directly into a special UV fibre. But the only fibre giving a reasonable amount of light was far too sensitive to mechanical forces to be able to install this fibre on a telescope mount embedded in cable chains moving up and down as the telescope follows a source. It should be stated that even in so called UV fibres attenuation is still very high due to unavoidable Rayleigh scattering, and any impact is amplified towards shorter wavelengths due to the scattering dependence on λ^{-4}.

Another reason for placing the scintillator in front of the fibre in terms of the light path instead of behind it was the maintainability of the whole system. With the scintillator next to the laser in the electronic hut at the telescope's base it

is much easier to exchange it in case of problems compared to the case when it would have been placed in a box in the centre of dish of the telescope. The final design eventually exhibited a regularly required maintenance task concerning the scintillator, that supported this decision.

The schematics in Fig. 4.12 show the UV-light focused by a special designed UV-focussing unit. This was only installed in the later stage of testing. Before that the scintillator was illuminated directly with the laser. Some holes were drilled carefully into the scintillator to place the end of the fibre closer to the maximum of the scintillation flash. The drilling has to be done quite slowly and carefully as the scintillator material tends to melt quickly under the mechanical heat of the drilling and would therefore develep opaque zones around the hole reducing the efficiency of light coupling from the scintillator material to the fibre. The position of the maximum of the scintillation has been determined by eye while energizing the scintillator with UV-pulses.

With the fibre to be tested while placed inside the scintillator hole, the hole was filled up with an optical coupling gel[4] via an injection needle to increase the coupling efficiency. The fibre is then guided to a diffuser which illuminates a H.E.S.S. PMT, the signal from which is then monitored.

It had been realised that the pieces of scintillator used at the beginning of testing were too big (several centimeters) which resulted in significant absorption inside the scintillator. The manufacturer of the scintillator states in its product detail document [Bicron Organics, 2003] that samples smaller than one centimeter in diameter should not show a significant self-absorption. Eventually it was realized that the light-coupling into the fibre could be maximized by placing a piece of scintillator only the size of a few millimeters on top of the fibre tip embedded in a drop of optical gel.

With this method of using a splinter of a scintillator the target amount of light could be achieved, however at the cost of two drawbacks. Firstly, the efficiency of light output of the small pieces of scintillator decreases significantly after several thousand shots. This is due to the focused UV-light of the laser burning the scintillator material. Secondly, the placement of a piece of millimeter-sized scintillator can not be done very reliably. After exchanging the scintillator, it is possible that the piece does not lie directly in front of the end of the fibre, so that the light input is reduced enourmously. Therefore a splinter of scintillator was replaced carefully

[4]Manufacturer: Dow-Corning, catalogue number: Q2-3067

each observing period.

4.4.3 Results

The first priority of our tests was the overall light throughput of the whole system — to be able to saturate the camera — with the pulse broadening as a second quality criterion. This obviously is based on the fact that even with a broadened pulse, flat-fielding of the camera can be achieved, but a short pulse is of no use when it is too weak to be detected by the camera.

In the beginning of the testing phase several different fibre brands were tested. This sample was put together from testing samples from companies and fibres formerly used with the Durham Mark VI experiment. As the decision was not yet made about the eventual setup and which fibre lengths were going to be needed, no efforts were made to cut fibre samples to exactly the same lengths as this more cost-effective in case long fibres were needed. For the final setup however, this situation was not at all restrictive because differences in the attenuation, light coupling, timing or eventual the handling properties of the different fibres were always large enough to easily achieve a 'ranking' within the sample. To demonstrate this, two tested fibres that have been sorted out early due to their lack of light throughput were a 30 m long piece with a 750 micron diameter from the manufacturer OMC which had surprisingly much less light throughput than a 100 m piece of a 50 micron diameter fibre from Brandrex. The term *throughput* should be considered here as a combination of the coupling efficiency and the light attenuation inside the fibre.

Due to the experimental nature of unknown coupling efficiency with a fibre loosely attached inside a hole in a scintillator, all judgement about the light throughput was done on a comparative basis with no consideration to absolute values but with the precaution of keeping as many parameters unchanged as possible like:

- warm-up time for the PMT,
- freshness of the optical gel used for coupling between fibre and scintillator hole,
- width of laser shutter opening,
- distance of the other end of the fibre to diffuser,
- distance of diffuser to PMT.

	'UV ' fibre 600 micron	Plastic fibre 1 mm
Length (m)	20	18.5
Amplitude (mV)	$336 \pm 34\%(smp) \pm 7\%(pss)$	$774 \pm 4.6\%(smp) \pm 5\%(pss)$
Pulsewidth (ns)	8.0 ± 0.4	7.4 ± 0.7
Attenuation (dB/km)	236 ± 24	215 ± 80

Table 4.1: Comparison of main parameters of two candidate fibres. The first error in the amplitude is the error between repeated measurements of 500 laser pulses each (smp=sample). The second error is the error between this 500 pulses, resulting from the PMT photon statistics (pss=poisson)

Sometimes, especially for attenuation measurements, additional neutral density filters were used between the diffuser and the PMT to increase the dynamic range of the testing bed. Despite the care that had been taken to keep the whole setup stable, detaching and attaching the fibre again to the scintillator often yielded an uncertainty in the resulting light output of a factor of about 2, as measured via the PMT amplitude. Nevertheless, our aim was to reach the required magnitude of light to make the flat-fielding feasible, which meant that this uncertainty did not prevent the efficacy of our tests. In table 4.1 the comparison of the first two candidate fibres are shown. One could see now a possible trade-off between either better light throughput or a shorter pulse. The attenuation is not very different, but as you can see the uncertainty is large due to the imprecise coupling method. Taking into account the very high mechanical sensitivity of the UV-fibre it was easy to decide for the plastic fibre on this occasion.

In the final decision for a fibre the required length was known (50 m) so that a direct comparison of the properties of the fibre candidates was possible. As mentioned before, first it was decided to go for the plastic fibre, but then a new 100 micron diameter fibre with a multimode graded refractive index (MGI) from BFI Optilas was tested and found to provide a much better pulse width (see table 4.2). Another promising candidate, a new UV-enhanced fibre, had to be rejected due to the lengthening of the pulse to 14 ns after a length of 50 m and a very much greater delicacy in terms of ruggedness of this fibre. Now the only problem was the light throughput

50 m lengths of	Pulsewidth(FWHM)(ns)
graded-index fibre 100 micron core	6.4 ± 0.7
plastic step-index fibre with 1 mm core	9.6 ± 0.5

Table 4.2: Comparison of pulse width of favoured fibre candidates

of the new BFI graded-index fibre, which was much less than the throughput from the 1 mm fibre, most probably just due to its much smaller diameter and therefore greatly reduced light collecting ability. Then it was discovered that a splinter of a scintillator would give about ten times more light than before, so that this problem could be overcome.

So as the best fibre for our application, the 100 μm multimode graded index fibre has been chosen, which has a reasonable light throughput and a good pulsewidth of (6.4 ± 0.7) ns after 50 m. This good timing is caused by the graded index of the fibre that prevents the modal distortion which is the main cause of the pulse broadening in step index fibres.

4.5 'Simple' Design Layout

The quickest way in terms of further required research (therefore 'Simple') to establish a working calibration system was to set up a laser in the telescope base unit (hereafter TBU) and guide the light through 50m of fibre to the dish centre unit (hereafter DCU).

4.5.1 Telescope Base Unit (TBU)

In the simple design layout, the TBU consists of (see Fig. 4.13):

- the laser, connected to the fibres that are guiding the light to the DCU,
- the controllers of the two filter wheels,
- the Com-Server, a device to convert Ethernet socket signals to RS232-signals for communication with the filterwheel-controllers and the laser-trigger module,
- the laser-trigger module consisting firstly of an electronic device that converts the RS232-signals from the Com-Server to TTL trigger signals for the TTL-input of the laser, and secondly of an TTL-Optical-TTL converter.

Although the laser already has an opto-isolated trigger input we have included an TTL-Optical-TTL converter between the trigger module and the TTL trigger input of the laser to have a pure optical trigger line and we convert this only inside the laser box to the required electrical TTL pulse for the purpose of minimising electrical

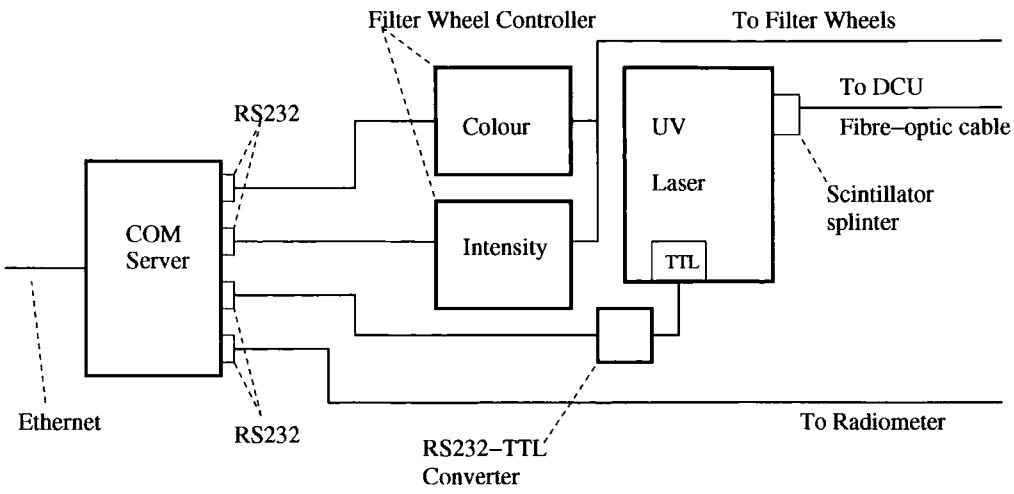

Figure 4.13: Schematics of the telescope base unit (TBU) as setup in the electronic container hut at the first telescope of H.E.S.S. phase 1

noise. This noise is created by the electrical cable carrying the TTL trigger pulse to the laser, because the cables act like antennas, especially if one uses the laser in the pulsed mode. The digitiser to process data from the monitoring diode would also be placed in the electronic hut, but is not installed so far due to higher priorities for installation of the other atmospheric monitoring devices described later in this thesis.

4.5.2 Dish Centre Unit (DCU)

The DCU contains the following devices (see Fig. 4.14):

- light output fibre optics,
- two filter wheels, one with different colour filters and one with neutral density filters to control the illuminating intensity; both filters are steered by a wire connection to the filter wheel controllers in the TBU, that are in turn controlled via the Ethernet Com-Server,
- a monitoring diode, placed so that it can see the outcoming light from the diffuser without producing a shadow on the camera,
- an amplifier unit for the diode signal before it is sent down to the electronics hut at the base of the telescope using RG58 coax cable.

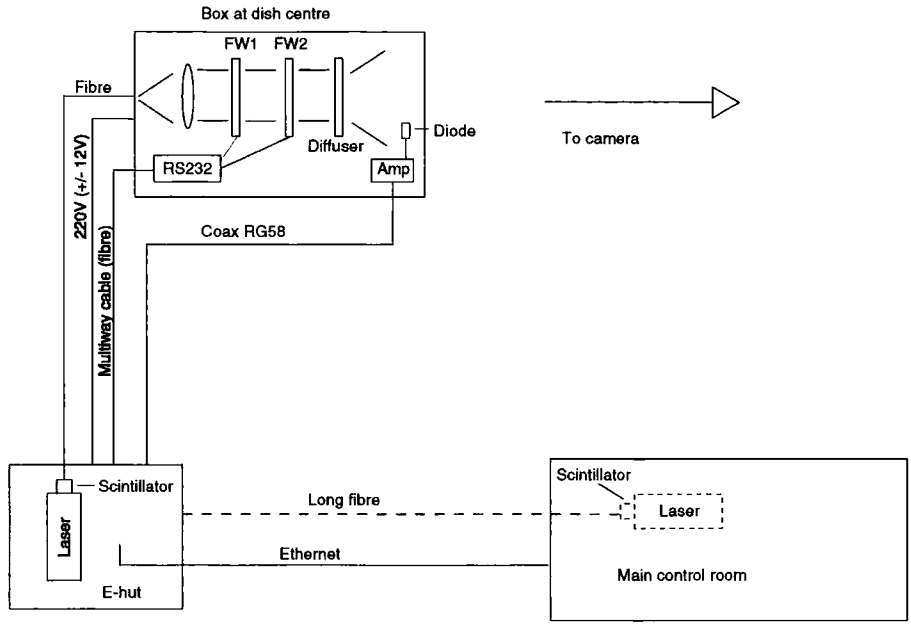

Figure 4.14: Schematics of the Dish-Centre-Unit (DCU) as built into the dish of the first telescope of H.E.S.S. phase 1

4.6 Single Laser Design Layout

Instead of having one laser at the base of each telescope, a second design layout was considered, where one laser would be installed in the main control room or some other central point and the laser flash guided via fibre to the four telescopes of Phase 1. The advantages of this solution would have been:

- much easier comparison of the state of each camera without having to take into account potential differences between four lasers due to ageing or other circumstances,
- reduction of purchasing costs (one laser instead of four), maintenance costs and time,
- fewer shielding problems.

One disadvantage of this solution would have been that the pulse length would inevitably be lengthened compared to the solution where the laser is at the telescope base. This is mainly due to the modal distortion inside the fibre as described earlier.

Preliminary measurements with a 300m long graded-index fibre were made. The pulse had a very low amplitude due to the simple coupling method used, which is basically placing the end of the fibre into a hole on the scintillator's surface which itself is attached to the laser box and therefore directly illuminated by the UV laser beam. As the detaching and attaching of the fibre to the scintillator yielded the aformentioned uncertainty of about 2 in the resulting amplitude, a clearly visible pulse could not be achieved reliably. Considering these uncertainties, the pulse width appeared to be about 12–13 ns after 300 m of fibre. In addition, the rise time of this pulse is degraded so much that this solution was rejected as we need a short rise time to be able to test the trigger ability of the camera.

One might have distinguished two possible arrangements for the one-laser solution:

- At a central point one may couple the laser light directly into the fibre (after splitting it up into four similar beams for the complete Phase 1), and guide the light to the dish centre to illuminate the piece of scintillator there, or

- illuminate the scintillator directly with the laser at the place of the laser, collect and couple the light into the fibre, and guide it to the dish centre.

The obvious difference is the wavelengths of the light which have to be guided through the fibre and the way of coupling the light. Because the scintillator light flash is spherical, it is much more difficult to collect much light and couple this into the fibre compared to collecting and coupling the parallel laser light. However, it is difficult to locate an appropriate fibre to guide the UV laser light directly through a large distance. Either the fibre's attenuation is very high in the UV-range or it has to be a very special UV-fibre which is both expensive and, in the case of fibre samples we tested, prone to damage. UV-transmissive multimode graded-index fibres exist and are claimed to have extremely small modal dispersion. However, a customized production run would be needed for our requirements of length and protection of the fibre, because standard applications only use short unprotected samples of these UV-fibres. We therefore used the 100 micron BFI Optilas multimode graded-index fibre, which is very flexible and therefore easy to handle. The MGI-fibre has the best timing of all fibres tested, but unfortunately too high an attenuation in the UV as tested with a UV-focussing system to introduce the laser light into the fibre; only marginal throughput could be achieved.

4.7 Modes of usage

During observations, there are two ways in which one can make use of a flat-fielding system which, as so often, have their full advantage only in combination. First, flat-fielding runs can be executed before and preferably after the night possibly with one extra run in the middle in order to monitor any changes in the gains of the camera pixels. However, as pedestals are determined by pixels not used in the image, roughly every minute, only the Winston cone and quantum efficiency differences are currently effectively monitored by the flatfielding. As these values do not change quickly over time, flatfielding runs are currently being undertaken every two days on average. To reduce the background of air-showers, the required pixel multiplicity for the camera trigger is increased to >9 pixels. Figure 4.15 shows the currently active flatfield coefficients used for the H.E.S.S. telescope CT2. In table 4.3 statistics of flatfielding values over the camera and over the period of one lunar cycle are shown.

Telescope	FF camera rms	FF average time rms
CT 1	10%	0.8%
CT 2	11%	0.9%
CT 3	13%	0.8%
CT 4	9%	1.0%

Table 4.3: Summary of the rms values for the flatfield coefficients as determined in January 200; the mean values are by definition 1. The middle column shows the rms over the camera for the merged flatfield coefficients of the lunar cycle, indicating the conformity of the camera. The third column shows the camera-averaged rms between each flatfield coefficient determination, indicating the good temporal stability over one lunar cycle (after Aharonian and the H.E.S.S. collaboration [2004a]).

For commissioning our system, initially software was written to control the filterwheels and the laser with a simple text-based interface via their Internet sockets provided by the Ethernet-RS232 converter. This then had to be connected later on to the DAQ-system where operators can pick the required parameters from a database and start a flat-fielding run without knowing any details about the system.

4.7.1 On-the-fly flatfielding

The Durham group has good experience with using a flat-field system 'on-the-fly', meaning that observation runs would be interspersed with randomised flatfield triggers to maximize the coverage of monitoring and to have a means to follow the

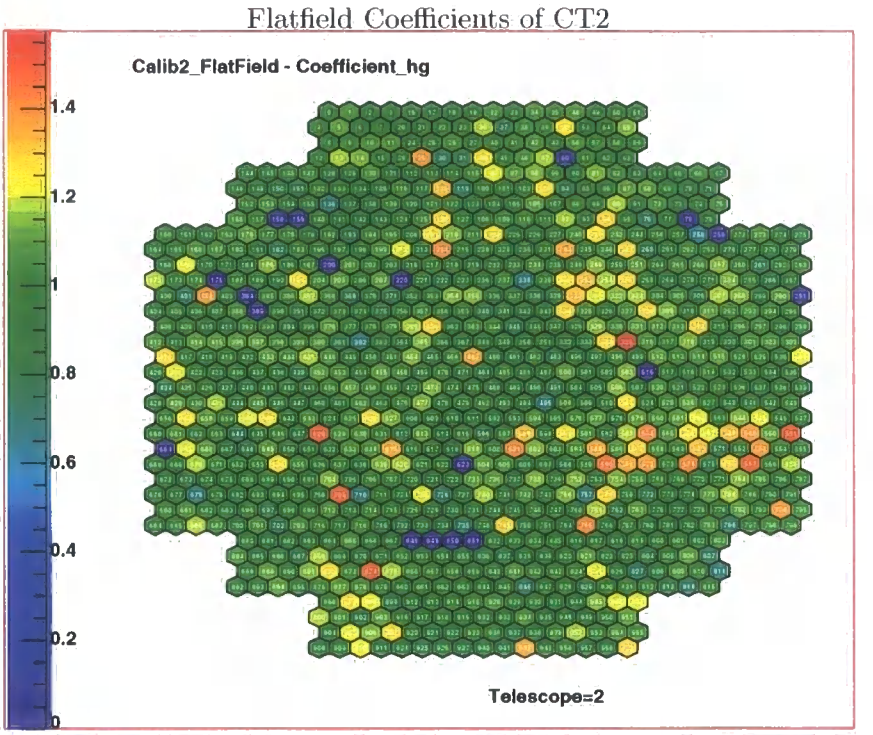

Figure 4.15: Current flatfield coefficients for the H.E.S.S. telescope CT2; the colour scale indicates the value of the coefficient, by design it is distributed around 1. The pixels with a violet colour reporting a flatfield coefficient at or around zero are broken or show an unlocked ARS, those pixels are automatically excluded from analysis.

temperature-dependent pedestals of the camera. Because in the H.E.S.S. system, pedestals are determined every minute, the need for continuous flatfielding is currently not highest priority. At the time of production of this flat-fielding system, the H.E.S.S. camera did not yet have the possibility of being externally triggered via an incoming electrical signal. For 'on-the-fly'-flatfielding this signal would be produced by the same trigger that signalled the light source to give out a pulse. This external trigger impulse for the camera is required to distinguish 'on-the-fly' flatfielding events from real data. The camera's data acqusition software would then flag these events as 'external'.

4.8 LED flatfielding

At the time of the setup of the second H.E.S.S. telescope, the development of short time pulsable UV LEDs had progressed enough to design a system based on this

new technology. Using a specially designed micro-electronic pulser board, the pulse width of these LEDs was finally comparable with those achieved with a system based on a short pulsed UV-laser; as the laser hardware is never used in the dish, those pulses are always widened by the required light guide, a disadvantage that is of no concern for light-weight small UV LEDs.

The other advantage is less required maintenance, because the weekly exchange of scintillator splinters is not necessary with this setup; furthermore the costs of the UV LEDS are much lower than for a short pulsed UV nitrogen laser. A detailed description is given in Aye et al. [2003]. After the LED system had been successfully tested on the following telescopes, the laser system on the first H.E.S.S. telescope was replaced by a LED based flat-fielding system as well.

Figure 4.16 shows flat-field coefficients determined by both the here described laser system and the new LED system. The figure indicates a wider distribution for the laser-determined coefficients. This is believed to be caused by the intrinsically greater pulse-to-pulse variations of the laser system due to the high voltage power supply.

4.9 Summary

This chapter has motivated and shown the development of the first flat-fielding device for the first operating H.E.S.S. telescope. It has been shown how known technologies as the short pulsed nitrogen UV laser have been combined with products of recent fibre-optic developments to meet the then new challenge of transporting this calibration light efficiently over a larger distance to setup a working flat-fielding system. Two designs for flat-fielding all four telescopes of H.E.S.S. Phase 1 have been considered; the simpler, but higher in costs and maintenance solution had to be chosen due to technical constraints. Eventually, technological developments in the area of UV LEDs overtook the design specifications of this laser based system and made it obsolete. But at the time careful considerations at all points of the system made it possible to have the light throughput efficient enough to be able to saturate the camera, thereby enabling us to test the H.E.S.S. cameras over its whole dynamic range of 10 to 200 photo-electrons [Aharonian and the H.E.S.S. collaboration, 2004a, section 7] controlled by the intensity filters.

The next chapters can be regarded as a second part of this thesis, as the focus will change now to atmospheric monitoring with the next chapter 5 outlining the

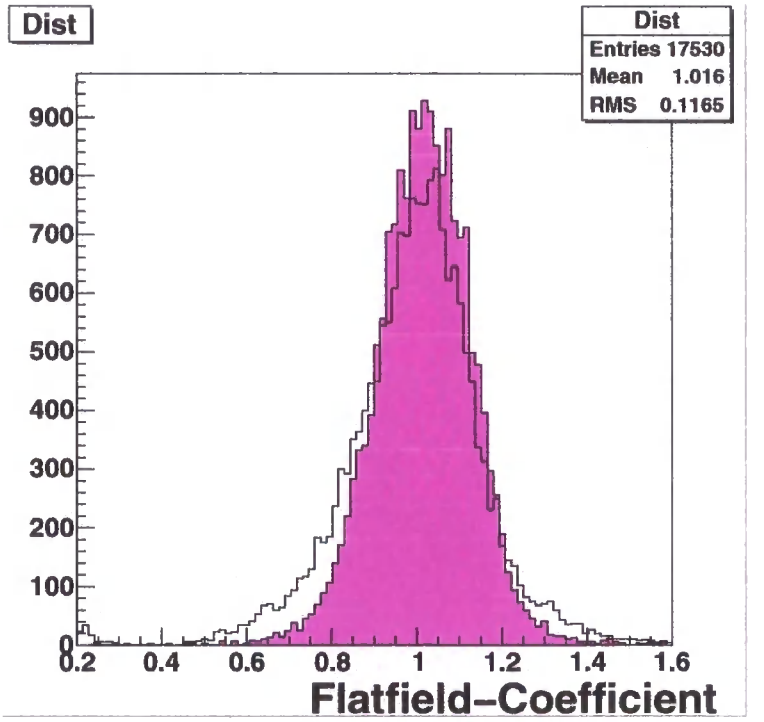

Figure 4.16: Comparison of the distributions of flat-field coefficients taken with both the laser-based (non-coloured histogram) and LED-based system (pink coloured); distributions are normalised (from S. Nolan [priv. comm.])

armada of monitoring devices in operation. This is followed by chapter 6 addressing in detail the LIDAR that is in use on the H.E.S.S. site in Namibia and chapter 7 that shows results of combined application of the monitoring devices.

Chapter 5

Atmospheric monitoring

This chapter will discuss the different atmospheric monitoring devices intstalled at the H.E.S.S. observatory in Namibia, how they work and what they are being used for. Some data from our weatherstation and different radiometers are shown. The Ceilometer will be discussed at length in chapter 6 and correlation studies with monitoring and telescope data can be found in chapter 7. The excellent books of W. Michael Farmer [Farmer, 2001a,b] should be acknowledged, that in great detail describe every aspect of attenuation effects in the atmosphere for remote sensing scientists. Some facts and tools of his books applied to the attenuation of Cherenkov photons are either mentioned here or used later on in the following chapters.

5.1 Motivation

As the atmosphere is the essential part of the detector in the imaging atmospheric Cherenkov technique, monitoring any changes in observable quantities becomes a crucial tool for determining the quality of data. The absorption of Cherenkov light depends on the wavelength, but due to its production by the atmosphere it changes as well with about every independent variable of the atmosphere itself, these being height, temperature, relative humidity and pressure. On top of this, aerosols contribute a non-negligible amount of scattering via Mie-scattering, this of course to be judged by the wavelength range of interest for Cherenkov astronomy (see Figure 5.1).

The main causes of extinction of Cherenkov light are absorption and Rayleigh scattering by molecules, and Mie scattering by aerosols. The H.E.S.S. photomultipliers and mirrors are sensitive to light between 250 and 700 nm. In this range the only light-*absorbing* molecule is ozone, but the most significant loss of Cherenkov

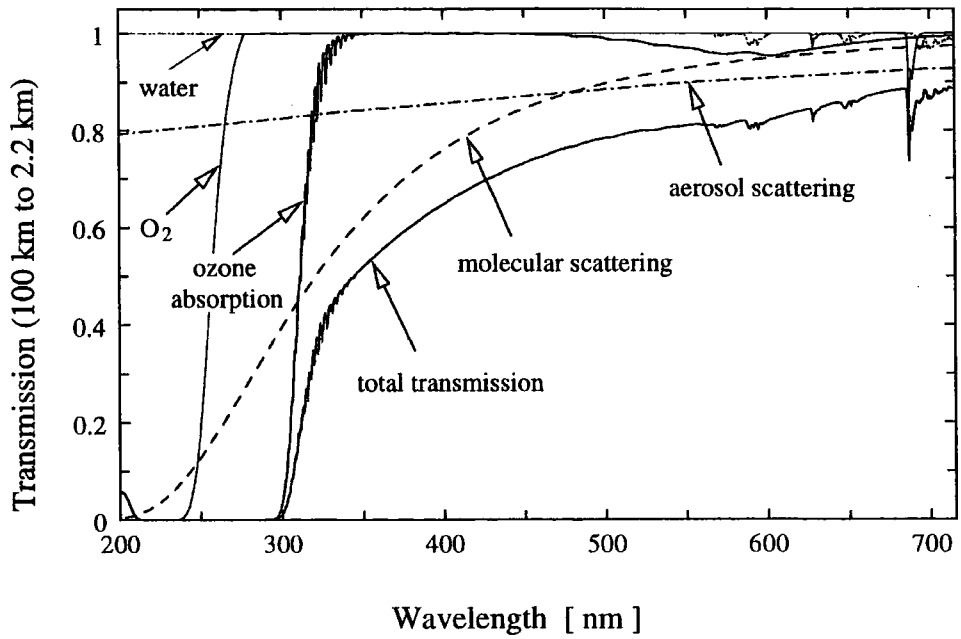

Figure 5.1: Sources of absorption in the wavelength range of interest for Cherenkov astronomy (taken from [Bernlöhr, 2000]).

light in the case of a 'clear' sky is caused by Rayleigh *scattering* off all atmospheric molecules dominant at lower wavelengths due to its λ^{-4} dependence, and Mie scattering on aerosols which becomes dominant above approximately 400 nm [Bernlöhr, 2000]. This dominance makes a strong case to put effort in providing a detection mechanism for aerosols to understand any changes in trigger rates and spectral indices deduced from flux measurements.

5.1.1 Software framework

A considerable effort has been undertaken by the author to create a software framework for analysis of data from all monitoring devices, building upon basic code structures and definitions of the collaboration. This provides members of the collaboration with an easy way to display and analyse all available atmospheric monitoring data without knowing the details of the hardware. This software has also been used by the author to create a publicly available website[1] to display summaries of all available atmospheric data of the past for all devices in operation. Information

[1] http://www.dur.ac.uk/klaus-michael.aye/atmo-monitoring.html. Should the website not be reachable, please get in touch with the Durham Gamma-Ray group.

Air temperature (°Celsius)
Relative Humidity (%)
Atmospheric Pressure (hPa)
Wind Speed (m/s)
Wind Direction (°)
Rainfall (mm)

Table 5.1: Available weather-station data.

about hardware changes/upgrades are also announced on this website. Examples of the graphics on this website can be seen in figures 5.2 and 5.3.

5.2 The weatherstation

A UK Meteorogical Office approved weatherstation from Campbell Scientific [2003] has been installed at the H.E.S.S. site. It provides the usual meteorological records (see table 5.1) and is being read out 24 hours a day. Its data acquisition is integrated in the standard DAQ scheme of our observatory and therefore produces, during online-analysis, helpful guidelines for potential reconsideration of observational programs and enables, during off-line analysis, efficient cross-checking of atmospheric conditions and camera data. E.g. an upper limit on relative humidity is applied for operation of the high voltage electronics of the H.E.S.S. cameras, because of the increased danger of humidity-induced electrical breakdown of the camera. The weather data are especially important for providing input values for atmospheric models used by software packages like MODTRAN to calculate the transmission properties of the atmosphere in combination with radiometer and LIDAR ("*LI*ght *D*etection *A*nd *R*anging") data.

To measure relative humidity is important for another reason, as it measures the proximity of the air towards water saturation. The closer the air is to saturation, the higher the probability of water globules being created, that in turn could attract dust and thereby build up larger aerosol particles with a higher attenuation of Cherenkov light. However, it is not clear at present stage, if the driving parameter for this aerosol globule creation is the relative humidity measuring the proximity to saturation, or the absolute humidity measuring the absolute water vapour content of the air. Therefore, to provide another parameter for correlation studies, absolute humidity is being calculated during analysis with the following relationships. The screen level saturation water vapour pressure p_s, measured in hPa, depends on

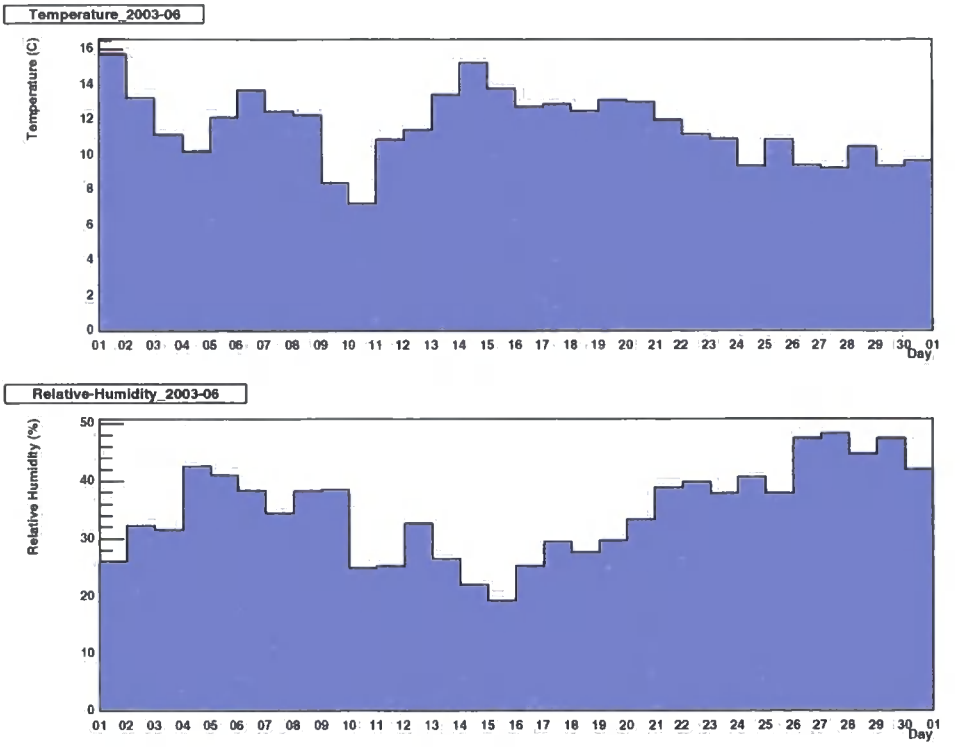

Figure 5.2: Monthly summary of temperatures and relative humidity for June, 2003. Values are daily averages for a bin width of one day.

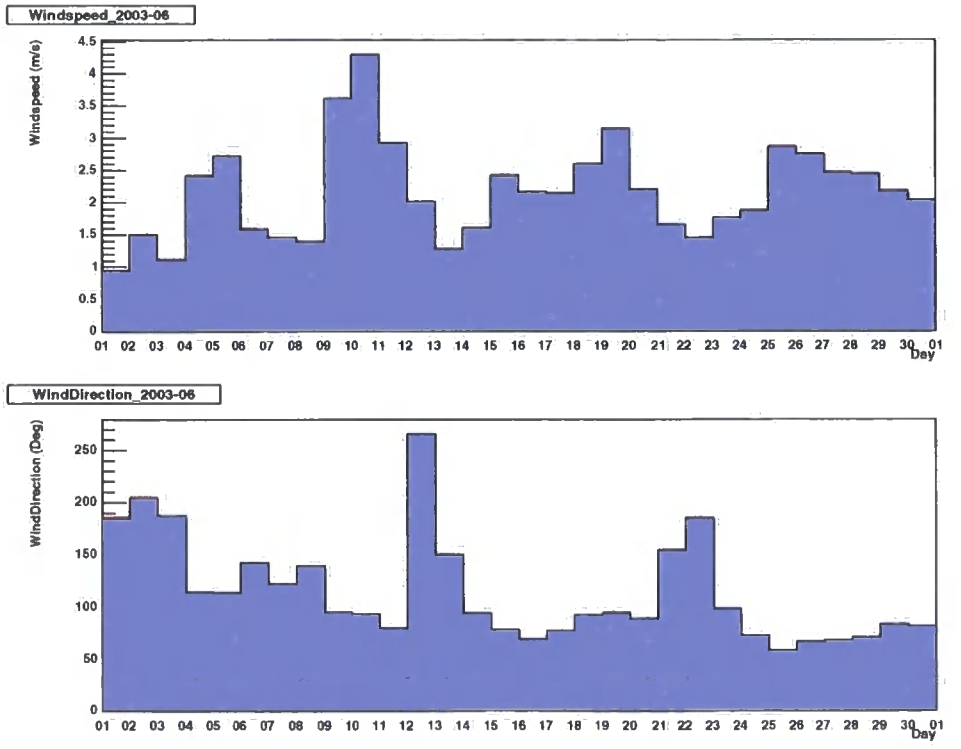

Figure 5.3: Monthly summary of windspeed and wind-direction for June, 2003. Data is binned by day (24 hours), values are the daily averages.

temperature as

$$p_s = 2.504 \times 10^9 \exp\left(-\frac{5417\text{K}}{T}\right) \text{ hPa} \tag{5.1}$$

where T is the temperature of the screen level air in Kelvin. Using this, relative humidity (rH) can be converted to the partial water vapour pressure as one of possible measures for absolute humidity p_w [hPa] via:

$$p_w = 0.01 \times rH \times p_s = 0.01 \times rH \times 2.504 \times 10^9 exp\left(-\frac{5417}{T}\right) \tag{5.2}$$

with the factor 0.01 resulting from the fact, that relative humidity is usually measured in percent of the ratio of partial water vapour pressure to saturation water vapour pressure.

Naturally, using this screen level values will not be a very good indicator for the development of aerosols throughout the atmospheric profile, but this is the best one can do to without having data from radiosonde measurements on site (see the discussion chapter 8).

5.3 The radiometer

The Heitronics KT19.82A Mark II is a radiometer designed for measuring the infrared radiation in the transmission window between 8 and 14μm [Heitronics, 2003]. The working principle of this infrared radiation pyrometer uses optical modulation of thermal radiation intercepted by an infrared detector.

In general, this is accomplished by an optical chopper made by mechanical blades driven by an electric motor. These blades periodically interrupt the incident radiation from the measured target to the detector. During each interruption the detector is exposed to an internal blackbody reference source having a defined temperature. Infrared detectors of the pyroelectric type must be operated with the 'chopped radiation' method because they respond to radiation differences and not to absolute radiation intensities. The detector intercepts infrared radiation emitted by the measured target and, at the same time, radiation emitted by the detector enclosure. During the short chopping cycles, in the millisecond range, the temperature of the pyrometer's housing does not change. The bias is thus eliminated and substituted by the reference signal, which can be easily measured or controlled within the specified reference accuracy over the operational ambient temperature range. Thus, the 'chopped radiation' method eliminates thermal drift and automatically provides a

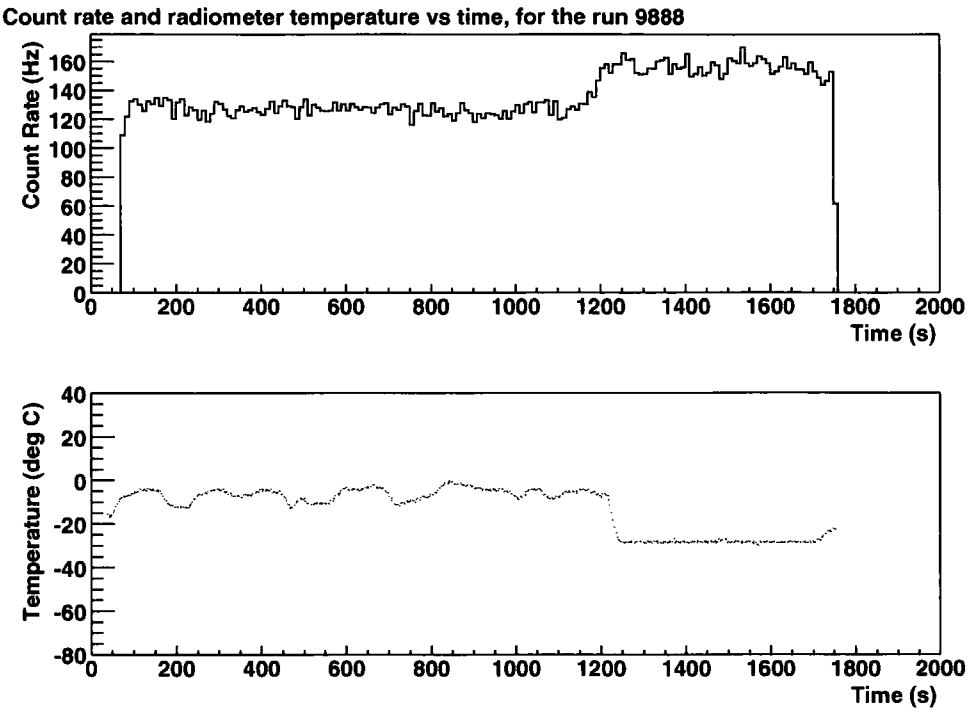

Figure 5.4: Correlation between telescope count rate and radiometer temperature due to Cherenkov light absorption by cloud [Gallou, 2004].

modulated signal with a precisely defined frequency.

The radiometer is used to measure the infrared radiation from the sky in its field of view of 2.9°. By fitting the observed flux between 8 and 14 micron to a blackbody spectrum, the radiometer then estimates the 'radiative' temperature of the sky as the temperature that creates the best fitting Planck spectrum. It has been shown [Buckley et al., 1999] that the measured sky temperature is very sensitive to the presence of clouds and water vapour which is crucial for determining the cause of a variation in the count rate of an IACT. Although clouds are not significantly warmer than the surrounding atmosphere, they are more effective emitters of blackbody radiation than the atmosphere in this wavelength range. If there are no clouds, the temperature still can vary from night to night due to relative humidity and temperature changes which may induce ice crystallisation on aerosols and therefore change the scattering phase function of Mie scattering (see chapter 6 for more about scattering phase functions).

All four telescopes of H.E.S.S Phase 1 have been operational since January 2004 and on each of them a radiometer is installed paraxially to provide an immediate

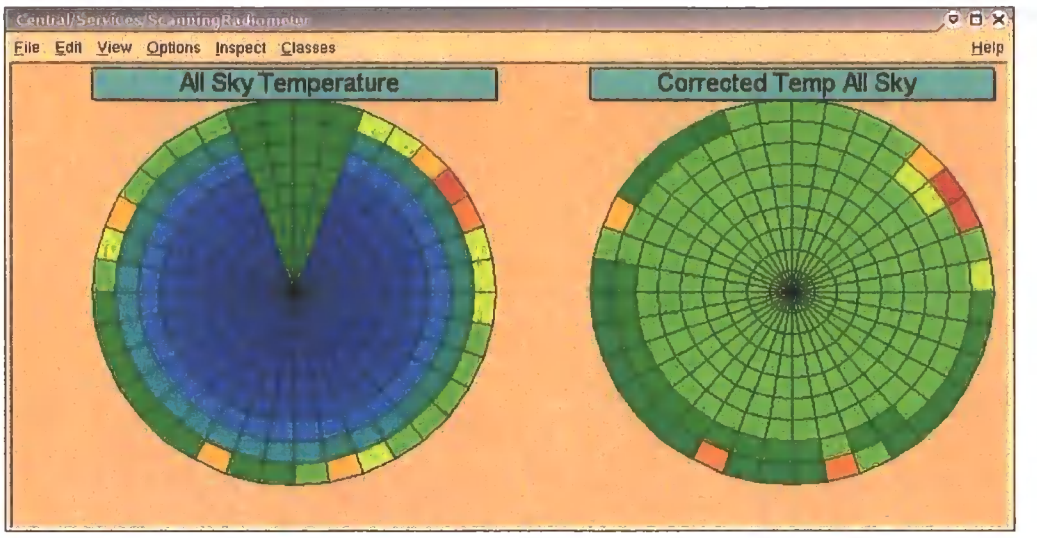

Figure 5.5: Graphic of the online-monitoring data from the scanning radiometer, embedded in the H.E.S.S.DAQ software. Each ring of this polar diagramm corresponds to one zenith angle bin, covering the azimuth angles. The 4 empty sectors on top are due to an instrumental dead zone, caused by the design of the pan-and-tilt unit. The left plot shows the raw read-out temperature, while the right plot has been corrected by a 1/cos-fit over the elevation (or zenith angle, respectively; see text for more detail). At low elevation (outer circles) landscape objects enter the field of view, which explains the higher IR temperatures at some places in the outer circles.

means of cloud detection in the field of view of the camera. Figure 5.4 shows the detection of the clearance of the sky after a period of high cloud. Furthermore, a scanning radiometer is installed to give the shift crew an immediate overview of the sky for any presence of clouds or approaching weather fronts (see Figure 5.5). Because of the importance of zenith angle dependencies for the energy calibration in the imaging Cherenkov technique, zenith angle variation studies of the IR flux have been performed using the online monitoring data of the scanning radiometer (see section 5.4).

In addition to detecting clouds, the radiometer data could theoretically be used to determine the amount of water vapour contained in a cloud-free atmosphere. This quantity determines among others the transmissivity of the atmosphere for Cherenkov light, but this measurement is not trivial. The temperature measured by the radiometer depends on several parameters: the temperature and water vapour profile of the atmosphere, the observing zenith angle, and the material of the window used to protect the instrument from the weather. Semi-empirical models like

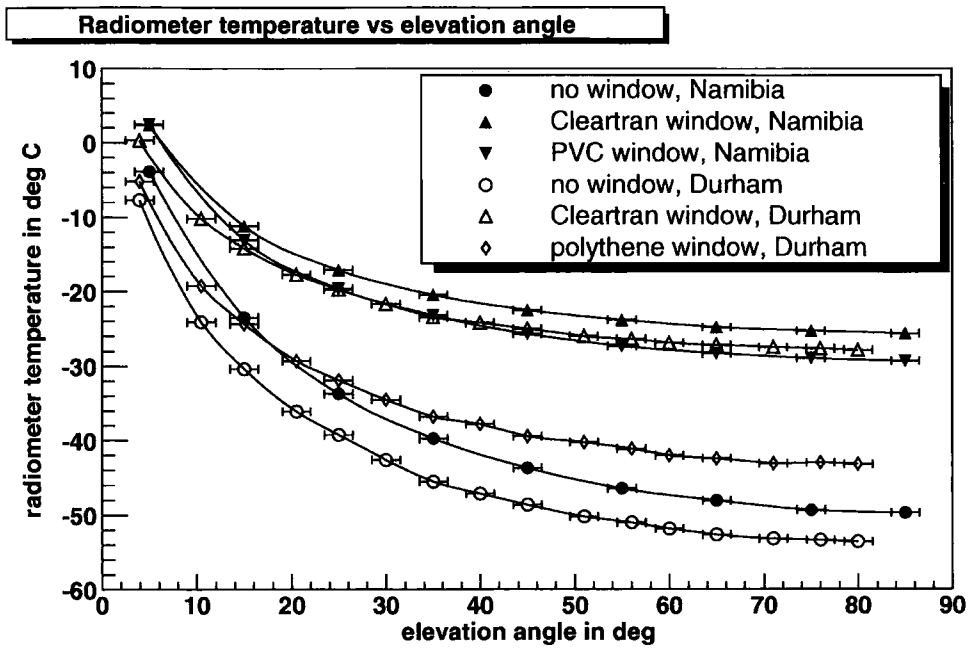

Figure 5.6: The relation between sky temperature and elevation angle of the radiometer with different winow materials. Ambient conditions in Namibia: nighttime, $T = 16°C$, rel. humidity 41%; Durham: afternoon, $T = 5°C$, rel. humidity $(70 \pm 10)\%$ [Gallou, 2004].

the one from Idso [1981] try to relate the infrared flux detected by the radiometer to the temperature and the water vapour pressure measured at ground level in a quantitative way. Indeed, we have measured such a correlation in our data (see chapter 7), but nevertheless this model is not satisfactory (as shown by Daniel [2002] and chapter 7) and a suitable one has yet to be found.

5.3.1 Zenith angle and window material dependencies

The temperature measured with the radiometer for a clear sky increases with the zenith angle due to a thicker section of the warm atmosphere being sampled [Buckley et al., 1999]. In figure 5.6 the zenith angle dependence for different window materials in front of the radiometer lens is shown. This window protects the lens of the radiometer from weather, but as it emits in the infrared, its influence on the measured value of the radiometer has to be considered. As one can see it not only increases the measured temperatures, but also alters the sensitivity $(T(\theta_{max}) - T(\theta_{min}))$. For this reason, the thin polythene film, whilst less robust than Cleartran^{TM}, is the chosen

material for the protective window.

5.4 Studies of the zenith angle dependence

No straightforward analytical expression exists for the zenith angle dependence of the cosmic ray telescope trigger rate. Experimenters usually use atmospheric simulations with packages like MODTRAN to cross-calibrate the telescope trigger rates at different elevations. Also very often a sec(Θ)-fit (Θ: zenith angle) is used for quick comparisons of gamma-ray data taken at different zenith-angles. Inspired by the results of Daniel [2002], that showed the superiority of a $\sec^n(\Theta)$-fit for IR radiometer data (with $\bar{n} = 0.32 \pm 0.01$ in [Daniel, 2002, chapter 6] for an urban north european climate) compared to a sec(Θ)-fit, further analysis of the zenith angle dependence seemed appropriate, concerning the differences in location, seasonal differences and night-to-night stability of this power law as the main determinant for the zenith angle dependence of the IR flux. The existing scanning radiometer data shall be analysed to determine the stability of the zenith angle dependence in the IR and to evaluate if correlation studies with telescope cosmic ray trigger rates could gain more insight into these relations, despite the different wavelength regimes.

5.4.1 Mathematical method

A flux calculated from the sky brightness temperature from the scanning radiometer dependent on the zenith angle of observation can be written as:

$$F(\Theta) = F_0 \sec^n(\Theta) \tag{5.3}$$

where F_0 is the flux at zenith and Θ the zenith angle. Transforming this to the logarithmic form, it becomes possible to use a simple first order polynomial fit (a.k.a. a linear fit) to fit the data:

$$\log\left(F\left(\Theta\right)\right) = n \log\left(sec\left(\Theta\right)\right) + \log(F_0) \tag{5.4}$$

that can be envisaged as:

$$f(x) = mx + b \tag{5.5}$$

where $log(F_0) \equiv b$ is the point of intercept of the logarithmic plot with the y-axis, corresponding to the flux at zenith, and $m \equiv n$ the slope of this graph, when plotted

against log(sec(Θ)), corresponding to the power index of the flux dependence.

5.4.2 Different observing modes

The scanning radiometer initially scanned the sky first in circles along the azimuth with the pan-unit and subsequent increases in elevation with the tilt-unit of the mount (see Figure 5.7). However, the load of the pan-and-tilt unit was close to its specifications, plus, in breach of these specifications, the steering unit proved not to be water-proof, which rendered the pan-tilt defunct due to the failure of a main integrated circuit component of the steering electronics after being in full-time operation until autumn 2003. Since then the SR, after some modification of the operational software, is operating in a pure zenith scanning mode (see Figure 5.8) while a new improved pan-tilt unit is currently commissioned.

However, for studies of the variability of the zenith angle dependence (V-ZAD), this is actually preferable, as the time between subsequent scans of the same elevation is shorter compared to the original mode, where all azimuth angles were scanned as well, resulting in a smaller probability for a changed sky-temperatue due to either fluctuations of air parcels or general temperature fluctuations.

5.4.3 Data analysis

Generating one profile

As previously shown, a radiometer is an excellent tool to detect clouds in the field of view. This feature of a radiometer, after being the main motive for its use, now becomes a nuisance, when it comes to study of V-ZAD, as it is compulsary to have a clear sky for obtaining sensible fits to the concurrent infrared ZAD. On a very clear cloudless day, even only one profile of one sky scan (without averaging over several scans) might result in a good fit like shown in figure 5.9. These kind of graphs are produced by interrupting the analysis loop over the data to begin a new profile measurement every time a full sky scan has been done twice, i.e. start observing at zenith, going to low elevations and returning back to the zenith. This results in having only two data points per zenith angle bin for the statistics of the fit; however, the fit works well if undisturbed by clouds in the field of view.

As soon as clouds are passing through the field of view of the instrument, noticeable for example through increased scatter in the measured sky temperature, the increased efficiency in blackbody radiation of these clouds immediately reduces

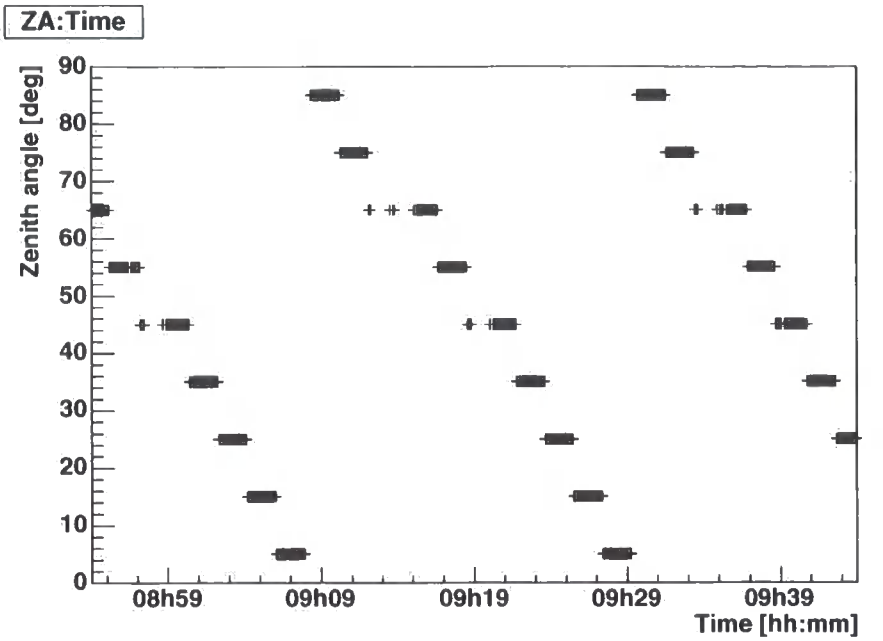

Figure 5.7: The original scanning pattern used by the scanning radiometer, as it was used to obtain the graphics in Figure 5.5. The points in the data looking different arise from collisions of remote steering commands with other remote procedure calls in early versions of the H.E.S.S. DAQ, resulting in the pan-tilt unit standing still for some time.

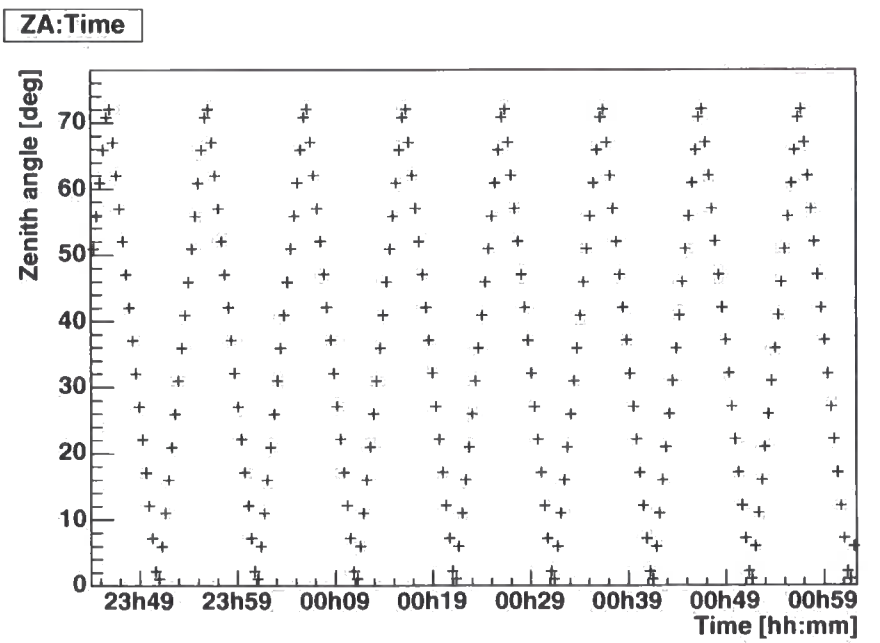

Figure 5.8: The scanning pattern used by the scanning radiometer, after the pan-unit became defunct.

significantly the quality of the fit results (as shown in Figure 5.10). Another difficulty that has to be considered when evaluating the later results, is the fact that the pan-tilt unit of the scanning radiometer on an irregular basis stops moving due to either timing problems with the RS232-commands or slipping drive disks. These times of missing data change the fit behaviour and increase the uncertainty for the obtained power indices during these times.

Errors

One has to note, that one measurement in this data means 'polling the radiometer for its current reading'. This value in turn is the result of thousands of measurements per second, providing an error of 0.5 K as given by the manufacturer. Following standard error propagation, this results in a temperature dependent error curve for the flux as shown in Figure 5.11. As this error is always smaller than 1% of the corresponding flux value, it has been neglected because the corresponding 'statistical' error for a particular zenith angle bin is mostly larger, considering that in the second observation mode only two measurements per profile are being taken. However, this 'statistical' error is, more accurately, a 'systematic' error caused by the fluctuations of the atmosphere *appearing* as a statistical error in between measurements of the same zenith angle.

Profiling over one day

Generating a profile every time a two-way sky scan has finished, the results of fitting these profiles with linear fits on log scales (yielding the power index and the zenith flux as described in sec. 5.4.1) can be displayed over time to see its development and to generate a mean value over time. The upper graph in figure 5.12 shows the development of the power index over the subsequent full profiles, i.e. over time. To create a value for one data run (which is normally equal to one day, providing no problems with the DAQ) for comparison between days, the lower graph shows how the power index values are spread assuming a Gaussian distribution. This assumption to have a Gaussian distribution for the power index was first considered to be a bold one, but having found a totally clear day with no clouds for full 24 hours (2004-02-05), comparison with other monitoring data (as shown in Figure 5.13) indicated, that the power index is not sensitive to changes in other monitoring

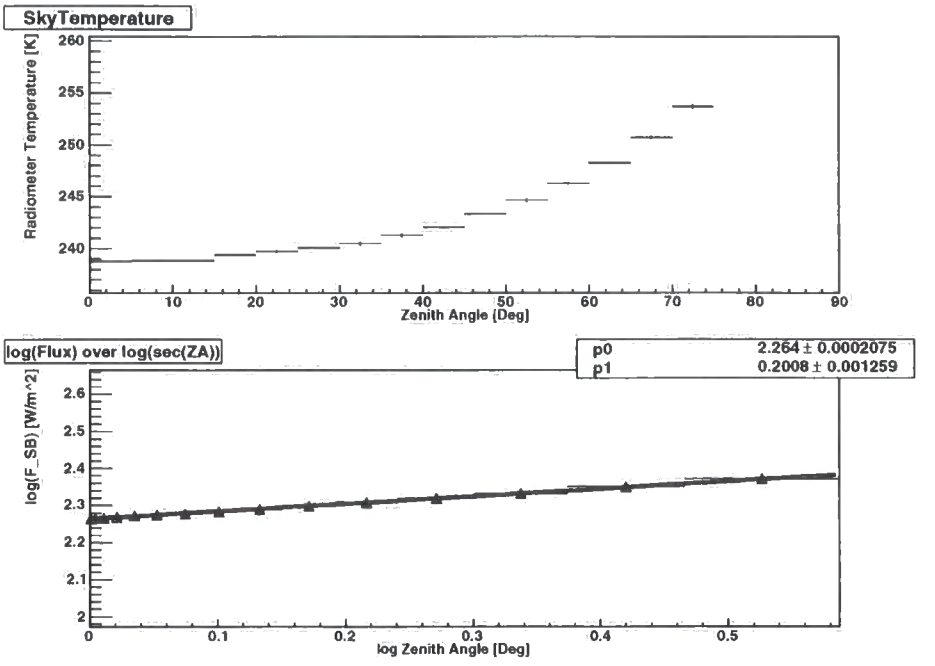

Figure 5.9: Scanning radiometer sky profile with only two measurements per zenith angle bin on a very clear day. Errors are shown, calculated from the mean value out of the two data points; horizontal error bar is the chosen bin width, as introduced by the observation mode. Upper figure: The raw sky-temperature radiometer data vs the zenith angle. Lower figure: A fit through the same data, transformed to $\log(\text{Flux}_{Stefan-Boltzman})$ vs $\log(1/\cos(\text{ZA}))$ (more details in the text).

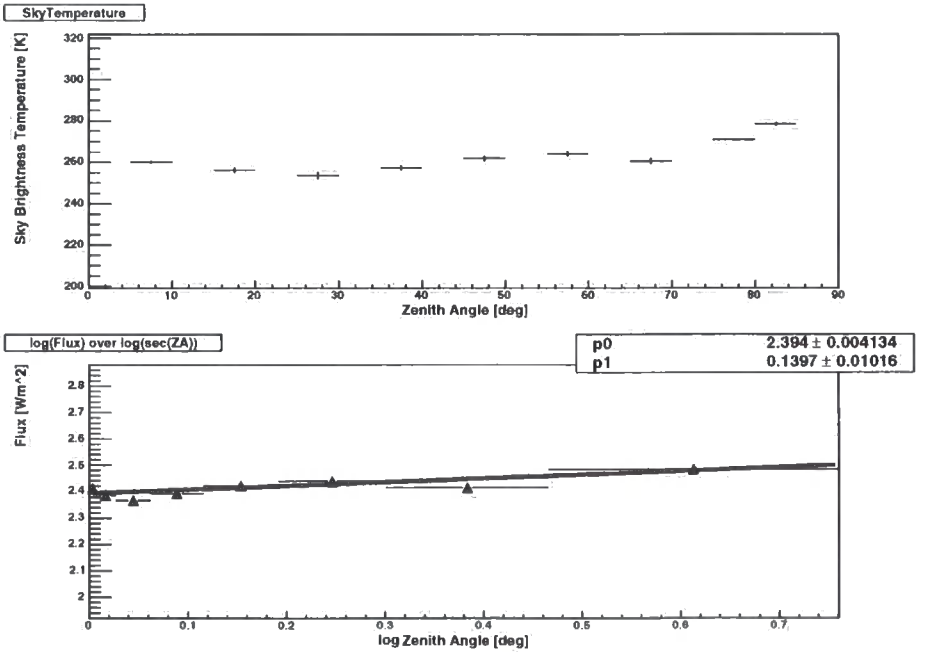

Figure 5.10: Sky profile with clouds in the field of view, resulting in a bad profile fit.

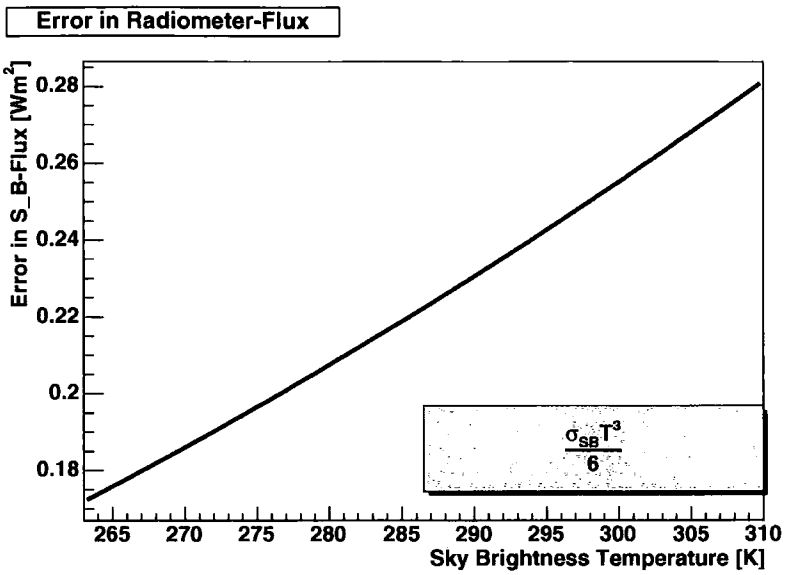

Figure 5.11: Errors in the calculated flux from radiometer measurements due to the instrument's systematic error of ± 0.5 K.

parameters, not even to an increased backscatter as measured by the Ceilometer[2] during the night hours of the same time interval.

Profiling over one month

Taking the mean and error of the Gaussian fit as data for the particular day, it is possible to scan all available scanning radiometer data to see how the power index develops from day to day. It turned out that to acquire an informative overview of the development of the power index of the sec(Θ)-fit only few months have enough usable data undisturbed from either DAQ upgrades causing data corruption or a too high level of cloud in the field of view of the scanning radiometer.

However, a few months of data could be analysed in a fruitful way, and the results are shown in figures 5.14 and 5.15. The data are quite scattered; however, as the errors of the Gaussian fits are not getting overwhelmingly large, and as it was shown before that the power index seems not to be sensitive to screen level parameters like humidities and temperature (in contrast to the zenith flux, which definitely is as Figure 5.13 shows), a careful consideration could indicate a different mean ZAD (see figures 5.16 and 5.17) for the two shown plots, possibly resulting

[2]The Ceilometer works at 905 nm, so at water vapour sensitive IR as the radiometer; however, this wavelength is NIR, compared to the radiometer's FIR operation range

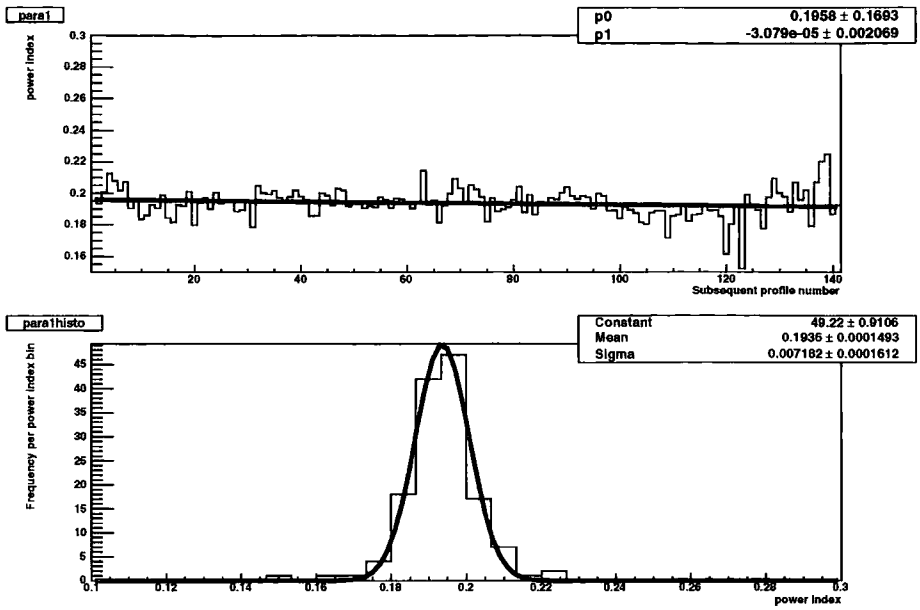

Figure 5.12: Upper graph: Development of the power index for the $\sec^n(\Theta)$-dependence over the time of one data run ($\sim$ 24 h, depending on data quality). The x-axis shows the subsequent profile number of full two-way sky scans. Lower graph: Projection of the upper graph, assuming a Gaussian distribution, in order to find a mean value of the power index for the data run (i.e. usually for one day).

from seasonal effects of the atmospheric structure.

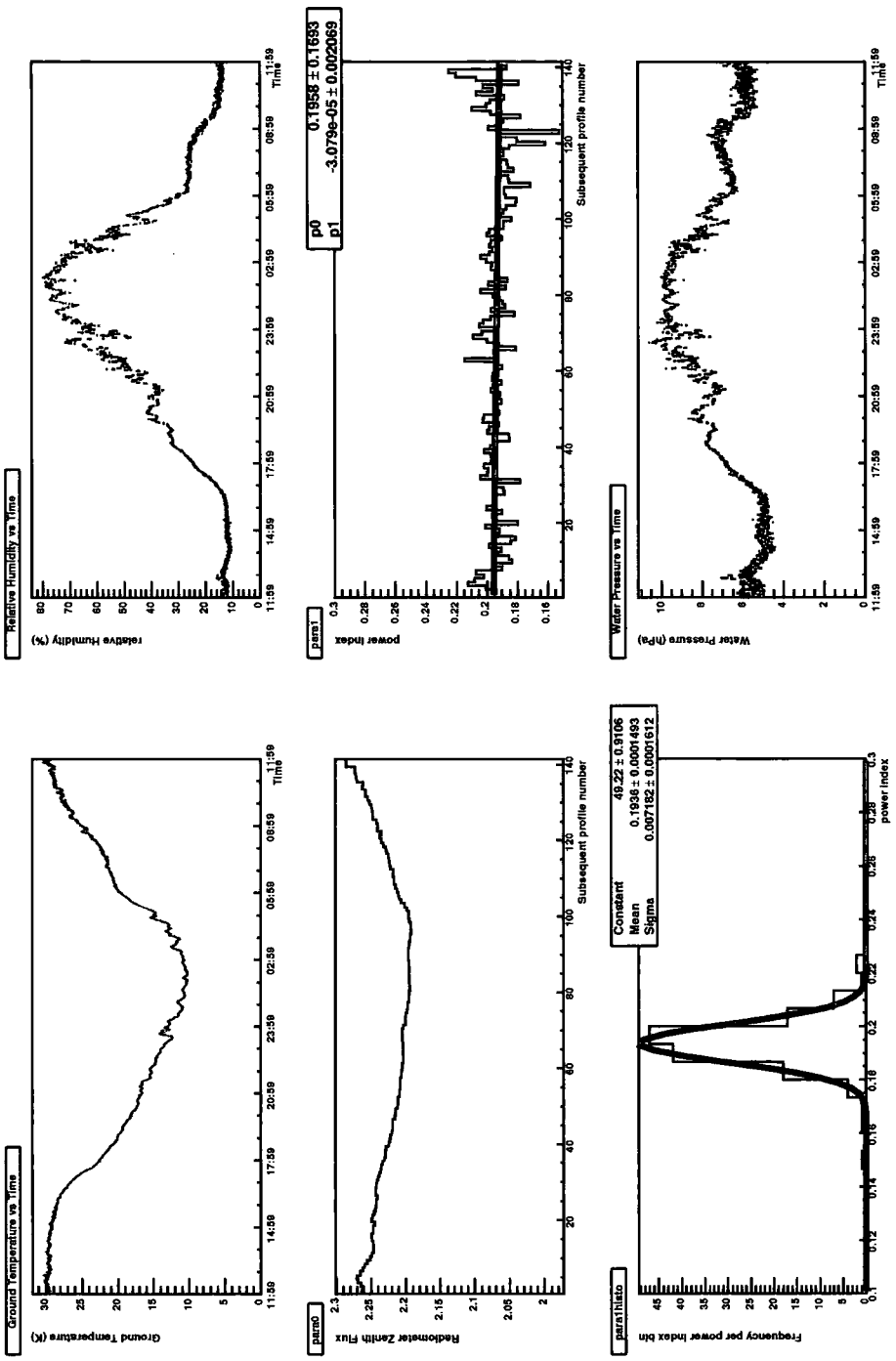

Figure 5.13: Overview of the time development of several monitoring parameters over one day. Remarkably, the power index (para1 graph) seems to be insensitive to the significant changes of the other parameters. The para1 graph shows the mean and spread of the power index, assuming a Gaussian distribution. Absolute humidity (indicated as 'water pressure') is calculated via temperature and relative humidity measurements as shown in sec. 5.2.

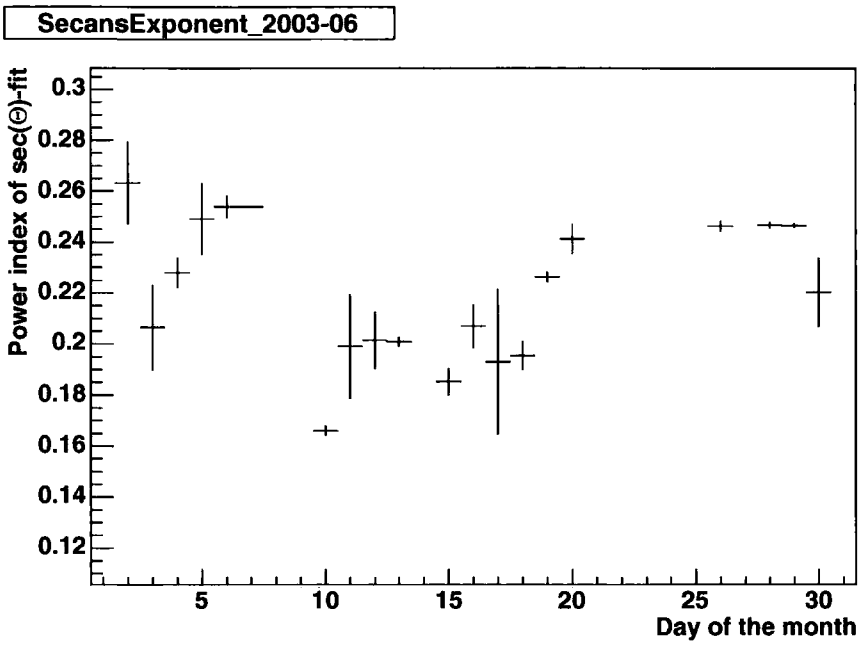

Figure 5.14: Development of the power index of the zenith angle dependence sec(Θ)-fit over the time of June, 2003. Note that June is local winter in Namibia, the time of clearest skies. Nevertheless, the ZAD seems to vary significantly.

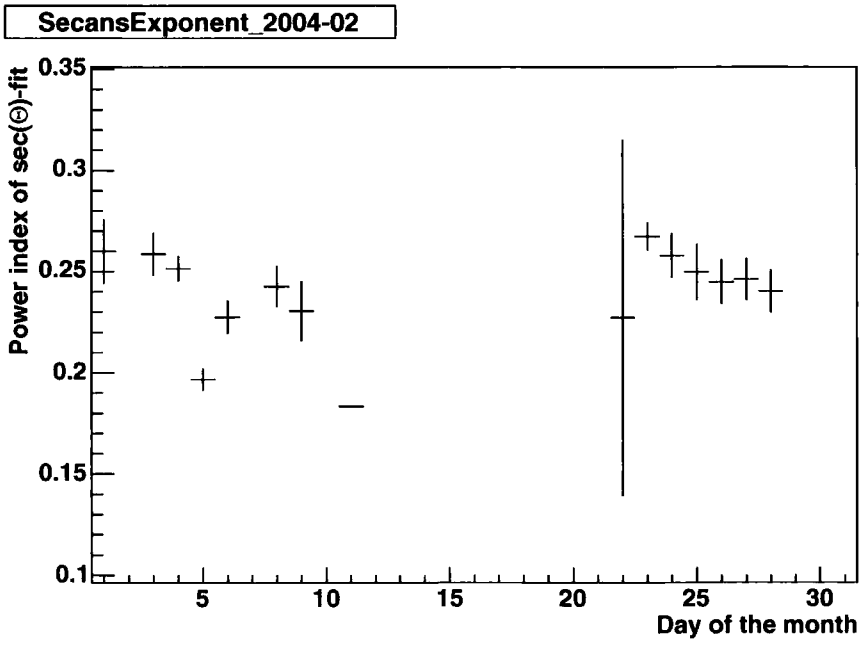

Figure 5.15: Same development as above for February, 2004.

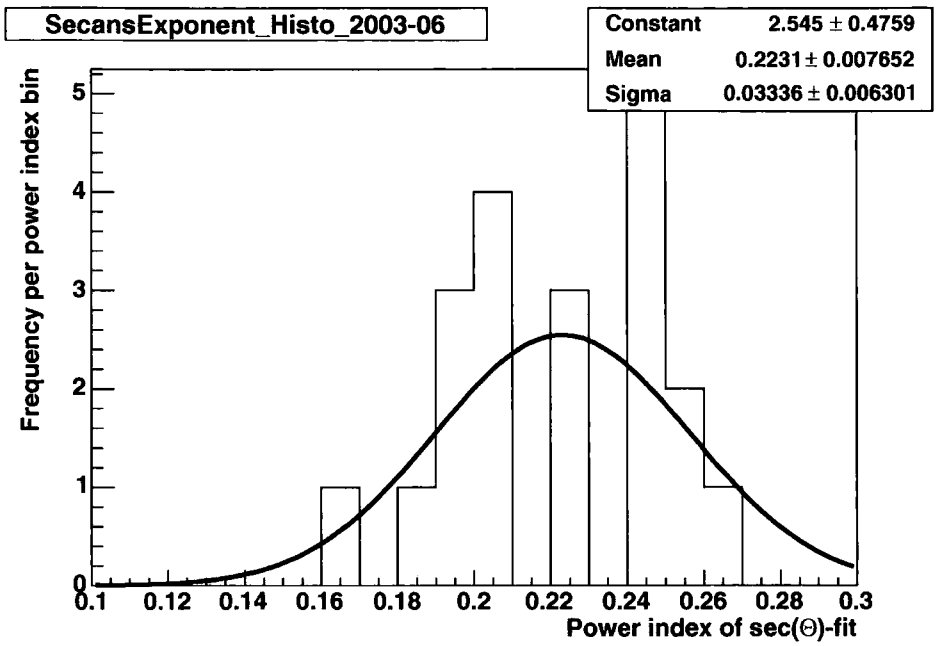

Figure 5.16: Histogram of the power indices in June, 2003, to find a mean value. Note that not much emphasis is placed on the validity of this value due to the scarcity and quality of the data.

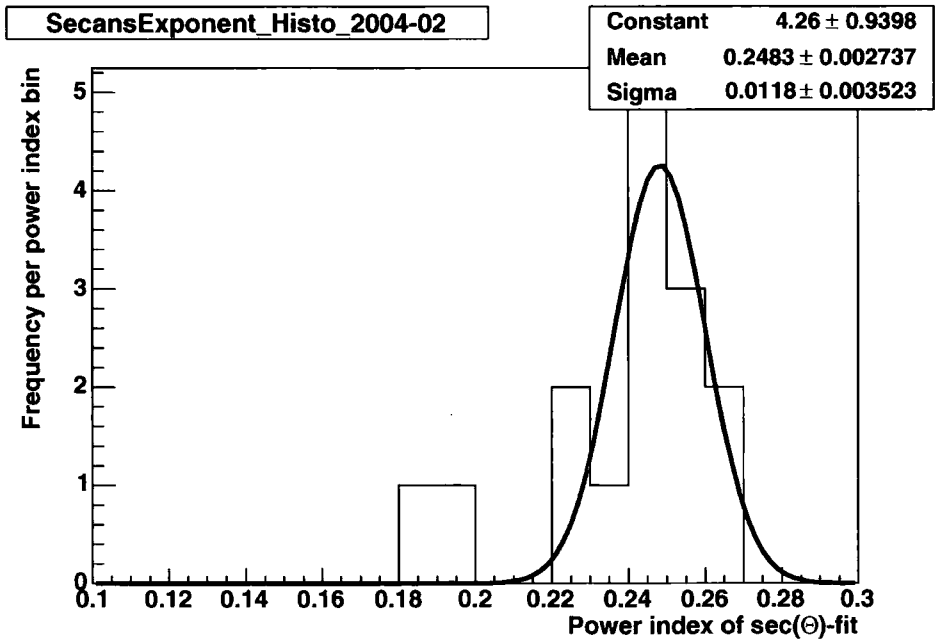

Figure 5.17: Same histogram as above for February, 2004.

Chapter 6

The Ceilometer

This chapter describes the Vaisala CT25K Ceilometer that we use at the H.E.S.S.-site as part of our atmospheric monitoring efforts. Section 6.1 describes the hardware contained in this commercially available LIDAR system and the basic principle of operation. In the following section 6.2 the LIDAR theory is described, with the standard solution for the LIDAR equation shown, known as *Klett inversion* after its inventor J. D. Klett [1981, 1985]. The numerical application of this solution is shown and problems with the current approach are described in the last section 6.5.

6.1 Introduction

Like a RADAR (RAdiowave Detection And Ranging), a LIDAR's (LIght Detection And Ranging) general concept consists of sending out electromagnetic waves and detecting the amplitude of the return pulse, that is backscattered from any object in the path, over time. The time dependence provides the distance to the backscattering object via the speed of light. The only difference of a LIDAR to a RADAR is the use of coherent laser light in near optical wavelengths compared to the radio waves used in a RADAR.

As the laser pulse traverses the sky, light will be backscattered with an amplitude depending on the current situation of the scattering volume. Some of the backscattered light reaches a photo-sensitive detector in the LIDAR and is digitised by an analogue to digital converter (ADC) system. Via the known speed of light and the measured arrival time of the backscatter signal, the height from which the photons have been backscattered, is determined.

Figure 6.1: Installed Ceilometer on the observatory site in Namibia. In the background the mast of the weather-station and its data-logger are visible.

6.1.1 Vaisala Ceilometer

The Vaisala CT25K Ceilometer (see Figure 6.1)is a commercial LIDAR that includes automated data analysis of the backscattered signal, automatically finds cloud signatures in the data and provides vertical visibility calculation. It uses light pulses at (905 ± 10)nm from a short-pulsed laser and the ADC in the CT25K is digitising every 100 nanoseconds and therefore providing a height resolution of 30 m.

The Ceilometer has been built with an eye-safe classification in mind, therefore the laser intensity is so low that the backscatter signal is smaller than the ambient noise; but, by counting statistics, it is possible to improve the signal to noise ratio. This is done by storing the backscattered profile over height in a circular buffer; for every height bin of 30 m there is one data slot in the buffer. The Ceilometer then, in its default setting, samples 2^{16} pulses this way, always adding the received light signal exactly over the previous bins so that the signal improves while the noise cancels out (see section 6.2).

This summative profile is then processed internally by a Vaisala copyright-protected algorithm to define the presence of clouds or other heavy absorbers of

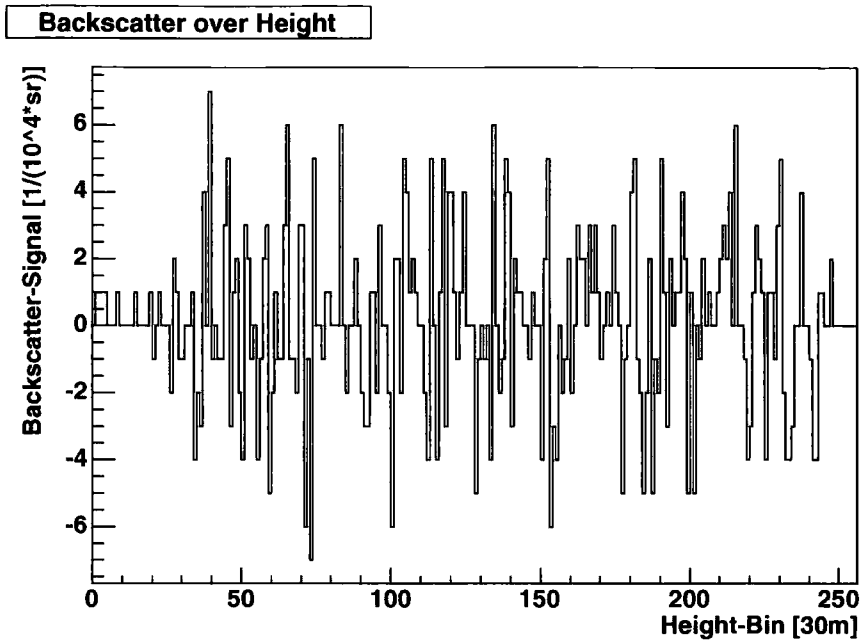

Figure 6.2: Raw result of sampling of 65k laser shots of the CT25K LIDAR Ceilometer

light, which is the main purpose of the Ceilometer. After the internal processing has finished, which takes about 15 seconds, an ASCII data message is produced, that is sent via RS232 to an RS232-Ethernet converter, similar to the one being described in chapter 4. This ethernet connection pushes the data to a data-collecting computer program to save the data in binary files for later analysis. For later reference, I will call one of these data blocks consisting of 2^{16} single measurements a *frame*.

An example of the raw data resulting after sampling of the roughly 65k shots can be seen in Figure 6.2. The technical details of the transmitter and receiver units can be found in the tables 6.1 and 6.2 respectively.

6.2 LIDAR theory

The general description of the instantaneous return signal strength is given as the LIDAR equation [Klett, 1981]

$$P(r) = E_0 \frac{c}{2} \frac{A}{z^2} \beta(r) e^{-2 \int_0^r \alpha(r')dr'} \tag{6.1}$$

where

Table 6.1: Transmitter details of the Vaisala CT25K Ceilometer LIDAR as taken from the manual [Vai, 2000]

Laser Source	Indium Gallium Arsenide (InGaAs) Diode Laser
Centre Wavelength	(905±5)nm at 25°C
Operating Mode	Pulsed
Nominal Pulse Energy	1.6 $\mu Ws \pm 20\%$ (factory adjustment)
Nominal Peak Power	16 W typical
Nominal Pulse Width	100 ns typical
Repetition Rate	5.57 kHz
Average Power	8.9 mW (full range measurement)
Max Irradiance	170 μW/cm^2 measured with 7 mm aperture
Laser Classification	Class 1
Laser Source Geometry	Five-stack, 0.4 mm^2
Beam Divergence	±0.53 mrad edge, ±0.75 mrad diagonal

Table 6.2: Details of receiver unit of Vaisala CT25K Ceilometer LIDAR, taken from manual [Vai, 2000]

Detector	Silicon Avalanche Photodiode (APD)
APD-characteristics	65 A/W Responsitivity at 905 nm
Surface Diameter	0.5 mm
Interference Filter	Centre wavelength 908 nm typical
50% Pass Band	35 nm at 890-925 typical
Transmissivity at 905 nm	80%typical, 70% minimum
Field-of-View divergence	±0.66 mrad

- $P(r)$ is the instantaneous power in Watts received from distance r,
- E_0 the effective pulse energy in Joules (taking all optical attenuation into account, measured by internal monitoring),
- c the speed of light,
- A the receiver aperture in $m^2 sr$,
- $\beta(r)$ the volume backscatter coefficient at distance r in $(m \cdot sr)^{-1}$ and
- $\int_0^r \alpha(r')dr'$ is also known as $\tau(r)$, the optical depth at r (see more in sec. 6.3). The factor 2 in front of the integral in the LIDAR equation accounts for the light travelling the same distance twice, out and back.

The term $e^{-\tau(r)}$ can also be written as a transmittance T:

$$T(r) = \frac{I(r)}{I_0} = e^{-\tau(r)}. \tag{6.2}$$

Usual simplifications consist of combining the instrumental factors into one value A', and multiplying the return power by r^2, as the $1/r^2$–weakening of the signal over distance is normally not of interest in LIDAR applications. This enables us to write the LIDAR equation in a simpler form as:

$$r^2 P(r) = A'\beta(r)T^2(r). \tag{6.3}$$

As $T(r)$ depends on the extinction $\alpha(r)$, this equation has more unknowns than measured parameters. To solve this problem, an auxiliary function $S(r)$ is usually added in the LIDAR literature (see e.g. the introduction of Filipčič [2003]) to get access to $\tau(r)$:

$$S(r) = ln\left(r^2 P(r)\right) = ln(A'\beta(r)) - 2\tau(r), \quad r > 0, \tag{6.4}$$

or, to get access to the extinction, the equation can be transformed into Bernoulli's differential equation (leaving out some r-dependencies for clarity):

$$\frac{dS(r)}{dr} = \frac{1}{\beta}\frac{d\beta}{dr} - 2\alpha. \tag{6.5}$$

Thanks to the self-monitoring system and internal pre-analysis of the Ceilometer, the data shown in Figure 6.2, taken from the data messages from the Ceilometer,

describes — according to the manufacturer — only the remaining dependence of backscatter and extinction, i.e.

$$\beta_{data} = \beta(r)T^2(r) \equiv \beta', \tag{6.6}$$

which shall be called *attenuated backscatter* for further reference and as seen in plots of Ceilometer data. Any further mention of backscatter data from the Ceilometer corresponds to this attenuated backscatter values (if not stated otherwise), that have to be inverted to obtain a transmission value.

6.3 Modelling opaque atmospheres

Many different ways exist to model opaque media, depending in what area of science it was required to be introduced and, more precisely, depending on the known parameters available. High energy physics for scattering experiments use e.g. cross-sections to *interpolate* from the inital and final beam intensity the number density of a medium to be tested. Astronomers, however, making 'educated guesses' about interfering media, often only need one parameter to measure the interfering media to *extrapolate* the inital light intensities from the estimated attenuation.

The *optical depth* gives a measure of how opaque a medium is to radiation that passes through it. It is measured along the vertical true (slant) *optical path* $\mathrm{d}r$, with the direction, in atmospheric science, upwards from the surface, so that

$$\mathrm{d}\tau \equiv \alpha\,\mathrm{d}r = \kappa\rho\,\mathrm{d}r \tag{6.7}$$

where α is the *extinction coefficient* [m^{-1}], κ the *opacity* [m^2/kg] and ρ the mass density of the medium [kg/m^3]. Introducing the *cross section* σ [m^2] and the number density n, $\mathrm{d}\tau$ can also be written as

$$\mathrm{d}\tau \equiv n\sigma\,\mathrm{d}r \tag{6.8}$$

so that

$$\tau = \int_0^r \alpha\,\mathrm{d}r' = N\sigma \tag{6.9}$$

where N is the *column density.*

For an isothermal atmosphere the barometric law gives us

$$\rho = \rho_0 e^{-z/H} \tag{6.10}$$

where ρ is the density at height z, ρ_0 the density at height $z = 0$ and H the pressure scale height, that is defined as

$$H = \frac{kT}{mg} \tag{6.11}$$

where k is the Boltzmann constant, T the ambient temperature, m the molecular mass and g the gravitational acceleration. If one measures along the direction determined by the vector of g, so for atmospheric scientists straight upwards, τ then can be developed to

$$\tau = \int_0^z \kappa\rho \, \mathrm{d}z = \kappa\rho_0 \int_0^z e^{-z'/H} \, \mathrm{d}z' = \kappa\rho H. \tag{6.12}$$

6.3.1 Aerosols

Aerosols are defined as the small (less than 10 micron diameter) fractions of particle size distributions produced by human and natural activity, small enough that, once airborne, an aerosol particle remains suspended in the atmosphere, at least for a time relevant for the problem under consideration. Sources include smokes, dusts, fogs, and precipitation. Normal atmospheric aerosol concentrations can range from less than 10 ccm^{-3} in very clear atmospheres to tens of thousands ccm^{-3} in smokes and dusts.

The ability to remain airborne depends on the size, shape, and specific gravity of the particle. The ability to scatter or absorb incident radiation on the other hand depends on particle size or diameter D relative to the illuminating wavelength λ and the chemical composition of the aerosol.

For $D/\lambda \ll 1$, Rayleigh scattering is the dominant factor for light scattering off aerosols[1]. Rayleigh scattering is essentially Thomson scattering off electrons bound in an atomic potential including the effects of resonances and phase coherence between multiple electrons. The Rayleigh scattering coefficent k_s, describing the amount of radiation scattered, and hence the intensity of scattered light, varies with

[1] Rayleigh scattering is also responsible for our blue sky

the wavelength of the incident light as

$$k_s = \frac{2\pi^5}{3} n \left(\frac{m^2 - 1}{m^2 + 2} \right)^2 \frac{d^6}{\lambda^4} \tag{6.13}$$

where n is the number of scattered particles with diameter d, and m the complex index of refraction (CIR). The aerosol CIR, which affects scatter and absorption properties, is dependent on chemical composition [Farmer, 2001a] and is described as

$$m = n + \mathrm{i}\kappa \tag{6.14}$$

where n is the well-known *refractive component* of the refractive index, and κ the *absorptive component* of the refractive index.

The extinction efficiency — the effective extinction area per physical cross-sectional area — typically peaks when $D/\lambda \sim 1$. Particles sizes much larger than one wavelength have an extinction efficiency that is asymptotic to a value of two [Farmer, 2001a]. Due to this, a particle can be considered 'small' at one wavelength, but 'large' at another, or, at the same wavelength, a small particle with diameter D at a particular wavelength has a scatter magnitude higher (towards all angles apart the near forward direction) than the scattering magnitude of a particle with a factor 50 larger physical diameter.

When $D/\lambda \gg 1$, the incident radiaton is scattered strongly in the forward direction. The formal solution to this electromagnetic wave scattering by homogenous spheres was first published almost simultaneously by Lorentz and Mie and shortly thereafter by Debye around 1908. The Lorentz-Mie scattering expresses the scatter magnitudes in terms of Legendre polynomials that are functions of the aerosol complex index of refraction, the ratio $\pi D/\lambda$ and scatter angles.

Extinction cross-section is the essential parameter defining the attenuation properties of aerosols resulting from scatter and absorption, so

$$\sigma_E = \sigma_S + \sigma_A \tag{6.15}$$

where σ_E is the extinction cross-section, σ_S the scatter cross-section, and σ_A the absorption cross-section. All cross-sections depend on wavelength λ and particle size diameter D.

Using Chylek's linear approximation to the extinction efficiency for particle size distributions between sizes much less than a wavelength to sizes roughly correspond-

ing to the peak in the extinction efficiency at $\pi D/\lambda \sim 1$, the mean extinction cross-section can be approximated by integration over the size distribution to

$$\bar{\sigma}_E(\lambda, D) \cong C_E \frac{\pi^2 \mu_3}{4\lambda} \tag{6.16}$$

where μ_3 is the third statistical moment of the size distribution [Chylek, 1978, Farmer, 2001a]. In the limit of $D \gg \lambda$, this cross-section is approximately

$$\hat{\sigma}_E \cong \frac{\pi}{2} D^2 \tag{6.17}$$

and integrated again over the size distribution, this gives a mean extinction cross-section for this limit as $\bar{\sigma}_E \cong \frac{\pi}{2}\mu_2$.

In low opacity atmospheres, the aforementioned extinction and the volume backscatter coefficient can be written as a sum of two independent terms, the molecular (Rayleigh) and aerosol (Mie) scattering or attenuation respectively:

$$\alpha(r) = \alpha_m(r) + \alpha_a(r) \tag{6.18}$$

$$\beta(r) = P_m(180°)\alpha_m(r) + P_a(180°)\alpha_a(r) \tag{6.19}$$

with α_m and α_a corresponding to the molecular and aerosol attenuation respectively and P_m and P_a the scattering phase functions for each case, determining in what direction the scatter is largest.

From the above considerations, it should be clear, that it is extremely useful to gain knowledge about the particle size distributions that lead actually to an increased backscatter on an astronomical observatory site. Knowing the particle size distributions and its statistical moments, one could set up a meaningful lidar simulation using the latter equations, with the Rayleigh scattering phase function being well understood and known empirical values for the phase functions of different particle size distributions. Efforts are currently underway of the Durham group to install aerosol sampling instruments.

6.4 Klett-Inversion

In his well known publications about stable analytical inversion solutions for the return power of a LIDAR system, Klett [1981, 1985] made the now widely used

assumption, that one can relate the backscatter and the extinction as:

$$\beta(r) \propto \alpha^k(r), \tag{6.20}$$

known now as the *LIDAR ratio*. This simple, and sometimes physically meaningful assumption enables the use of the existing analytical solution for eq. 6.5. However the direct application of the solution, called *forward inversion*, is numerically unstable, in some cases even singular, and highly sensitive to the signal-to-noise ratio (SNR). Klett reformulated the solution to avoid these problems into the so called *backward inversion*, where the inversion algorithm starts from the far point of the measured signal r_f and proceeds towards the near end:

$$\alpha(r;\alpha_f) = \frac{e^{S(r)/k}}{\frac{e^{S_f/k}}{\alpha_f} + \left(\frac{2}{k}\right)\int_r^{r_f} e^{S(r')/k}dr'}, \tag{6.21}$$

where $S_f = S(r_f)$, and $\alpha_f = \alpha(r_f)$ is an estimate(!, for further discussion on this see section 6.6) for the attenuation at the far end of the measured data set, which is determined by the size of the ring buffer memory of the detector unit (larger size $\rightarrow$ more time to wait for a signal) and the sensitivity of the receiver optics ($1/r^2$–decrease of signal). The unknown boundary attenuation α_f now carries all 'responsibility' for a stable solution for the reconstructed attenuation, or in other words, the reconstructed attenuation is still a one-parameter function of α_f. The increased stability of the backward inversion can now easily be understood in terms of the choice problem of α_f; the extinction at low heights will always be higher than at greater heights, simply because of higher number density of aerosols close to the ground. So, the choice of a realistic initial α for the inversion algorithm depends very much on the current atmospheric state. But at great heights, far away from the boundary layer around 1.5–2km, the atmosphere contains fewer and fewer aerosols, so that the extinction value will approach quickly the value for pure molecular scattering, which can be modelled easily with the Rayleigh theory. Therefore the choice of an initial value for α becomes less error-prone.

6.5 Numerical application of backward inversion

First we have to derive the connections between the inversion algorithm from eq. 6.21 on page 118 and the data we receive from the Ceilometer, for which I defined in eq. 6.6 on page 114: $\beta_{data} = \beta(r)T^2(r) \equiv \beta'$. To do that, let me first expand the auxiliary S-function from eq. 6.4 on page 113 a bit more (for clarity, I will omit all r-dependencies for now):

$$S = ln(r^2P) = ln(A'\beta) - 2\tau = ln(A') + ln(\beta) - 2\tau. \tag{6.22}$$

But from the manufacturer (as mentioned in eq. 6.6) we know that

$$ln(\beta) - 2\tau \equiv \ln(\beta'), \tag{6.23}$$

with β' being my shortcut for β_{data}.

So now we can insert our β' into the definition of the S-function:

$$S = ln(A') + ln(\beta) - 2\tau = ln(A') + ln(\beta'). \tag{6.24}$$

Taking the last equation into the natural exponential function:

$$e^S = A'\beta' \tag{6.25}$$

provides us with an essential part of the inversion formula of eq. 6.21, after we put it to the power of 1/k:

$$e^{S/k} = \left(e^S\right)^{1/k} = (A'\beta')^{1/k} \tag{6.26}$$

Using this nice simplification, eq. 6.21 can be transformed to

$$\alpha(r;\alpha_f) = \frac{(A'\beta')^{1/k}}{\frac{(A'\beta'_f)^{1/k}}{\alpha_f} + \left(\frac{2}{k}\right)\int_r^{r_f}(A'\beta')^{1/k}\mathrm{d}r'} \tag{6.27}$$

and as the instrumental factor A' does not depend on r, it cancels out and the previous equation becomes eventually

$$\alpha(r;\alpha_f) = \frac{(\beta')^{1/k}}{\frac{(\beta'_f)^{1/k}}{\alpha_f} + \left(\frac{2}{k}\right)\int_r^{r_f}(\beta')^{1/k}\mathrm{d}r'}, \tag{6.28}$$

our starting point for construction of the numerical solution of the inversion.

6.5.1 Numerics

For a numerical calculation of eq. 6.28 we first develop the integral in the denominator. And the simplest way to implement a numerical integral is the so called *Trapezoidal rule* [Press et al., 1986]:

$$\int_{x_1}^{x_2} f(x)dx = h\left[\frac{1}{2}f_1 + \frac{1}{2}f_2\right] + O\left(h^3 f''\right) \tag{6.29}$$

with h being the interval or difference in x between the two integral limits and f_1 and f_2 the value of the function at the integral limits x_1 and x_2 respectively.

If we now switch to index notation to indicate the relation to indices of data values in arrays and inserting the trapezoidal rule into eq. 6.28, it becomes

$$\alpha_i(i;\alpha_f) = \frac{(\beta_i')^{1/k}}{\frac{(\beta_f')^{1/k}}{\alpha_f} + \left(\frac{2}{k}\right)\left(\frac{\Delta h}{2}\right)\left[(\beta_i')^{1/k} + \left(\beta_f'\right)^{1/k}\right]}, \tag{6.30}$$

with Δh the interval between the two heights in between the integral shall be calculated, namely the height at position i and at the far point f.

As the extinction shall be calculated at all heights, the efficiency of the numerical integration would be higher, if it were possible to remember the result of the integration from the last calculated value and merely adding the next via the trapezoidal rule, instead of integrating over a bigger and bigger interval with the trapezoidal rule approximation. As shown in eq. 6.29, the error of the approximation goes with h^3, which is another motivation to keep h as small as possible at every application of the approximation.

It is possible to make further transformations to the last equation to enable the suggested procedure. As one can easily see, the inital value of the iteration of eq. 6.30 comes out as α_f, because Δh is zero at that moment (integration between identical heights).

Letting $k = 1$ for the moment and noting that Δh is the height difference between two digitised values, the next two values at the following lower heights (indicated

by r_{f-1} and r_{f-2} respectively) would come out as:

$$\alpha_{f-1} = \frac{\beta'_{f-1}}{\frac{\beta_f}{\alpha_f} - \Delta h\left[\beta_{f-1} + \beta_f\right]} \tag{6.31}$$

and

$$\begin{aligned}\alpha_{f-2} &= \frac{\beta'_{f-2}}{\frac{\beta_f}{\alpha_f} - 2\int_{r_{f-2}}^{r_f} \beta' \mathrm{d}r'} = \frac{\beta'_{f-2}}{\frac{\beta_f}{\alpha_f} - 2\left(\int_{r_{f-2}}^{r_{f-1}} \beta' \mathrm{d}r' + \int_{r_{f-1}}^{r_f} \beta' \mathrm{d}r'\right)} \\ &= \frac{\beta'_{f-2}}{\frac{\beta_f}{\alpha_f} - \Delta h\left[\beta_{f-1} + \beta_f\right] - \Delta h\left[\beta_{f-2} + \beta_{f-1}\right]}\end{aligned} \tag{6.32}$$

using the addition theorem for integrals in the last equation. Noticing the equality of the first two terms of the denominator in eq. 6.32 with the denominator of eq. 6.31, one can reposition terms in eq. 6.31,

$$\frac{\beta'_{f-1}}{\alpha_{f-1}} = \frac{\beta_f}{\alpha_f} - \Delta h\left[\beta_{f-1} + \beta_f\right], \tag{6.33}$$

to replace the first two terms in the denominator of eq. 6.32 and to introduce a recursive dependence to the last calculated value:

$$\alpha_{f-2} = \frac{\beta'_{f-2}}{\frac{\beta_{f-1}}{\alpha_{f-1}} - \Delta h\left[\beta_{f-2} + \beta_{f-1}\right]}. \tag{6.34}$$

Reintroduction of k and generalising provides us with the formula actually used in my software for the calculation of the extinction profile:

$$\alpha_{i-1} = \frac{\left(\beta'_{i-1}\right)^{1/k}}{\frac{\left(\beta'_i\right)^{1/k}}{\alpha_i} + \left(\frac{\Delta h}{k}\right)\left[\left(\beta'_{i-1}\right)^{1/k} + \left(\beta'_i\right)^{1/k}\right]}. \tag{6.35}$$

6.6 The far point problem

Usually the initial 'integration seed' value for α is being taken from simulation, as only Rayleigh scattering is assumed to be dominant at greater heights, the modelling of which is well understood. Figure 6.3 shows different optical depths (ODs) as calculated by the MODTRAN atmospheric simulation package [Berk et al., 1987](see

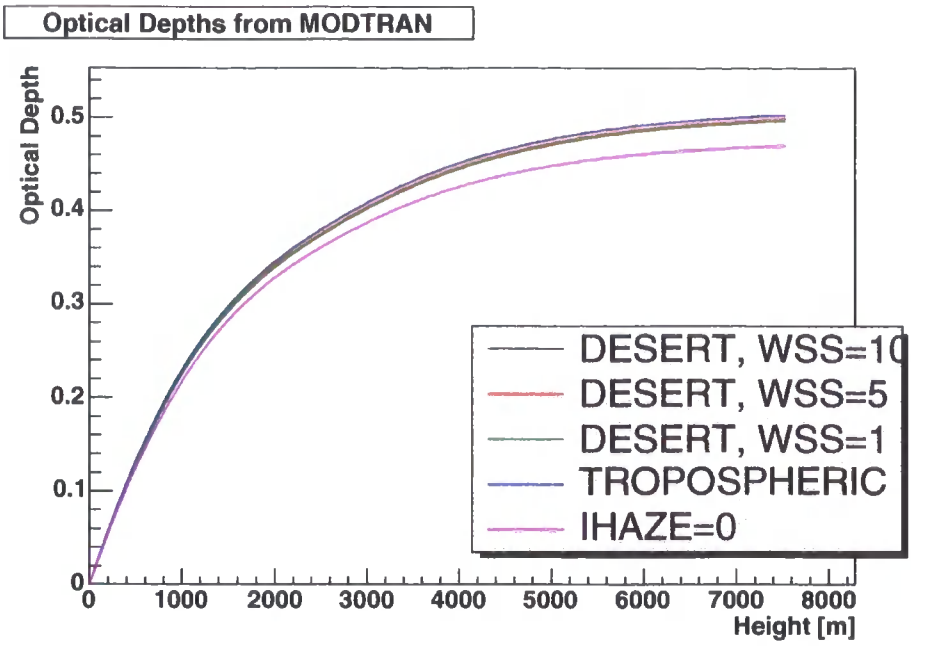

Figure 6.3: Optical depths between 900 and 910 nm for the range of the Ceilometer, calculated by the atmospheric simulation package MODTRAN. All graphs are simulated for a tropical atmosphere at 15° latitude north with different aerosols models, controlled by the parameter IHAZE. The tropical atmosphere proved to correlate best with radiosonde measurements taken at Windhoek, Namibia (as shown in [Nolan, 2002]). The 'tropospheric' IHAZE variant, shown with a blue line, covers almost exactly the DESERT variant at 10 m/s windspeed, 'shown' as a black line. Windspeeds vary from 0 to 5 m/s during 24 hours at the observatory, being very low at most nights and following closely the local ground level temperature (more detail in the text).

section 6.6.1).

6.6.1 MODTRAN

MODTRAN is a widely used atmospheric simulation package, that has proven to give good results for transmission calculations of different atmosphere regions on the world under different local conditions. High precision radiometers have been used to cross-check the results of the simulations and the results agree very well [Berk et al., 1987].

Parameters controllable in MODTRAN amount to the hundreds, but the most important are:

- the geographical position,
- the season of the year,
- a very detailed 'line of sight'-construction model, enabling the use for satellite detector simulations as well. In this, the height above ground and/or above sea level is controllable as well (a point of discussion below).
- an aerosol model, controlled with the parameter IHAZE, the influence of which is steerable again by other parameters like windspeed and/or relative humidity, depending in turn on the chosen IHAZE model,
- the wavelength range to be simulated,
- the gas component distribution of the air.

In standard mode, MODTRAN calculates a transmission value T for every wavelength- and line-of-sight-bin as chosen by the input parameters; this can be transformed to an extinction value for the Klett inversion.

As ODs are calculated from extinction $\alpha(r)$ by integration $\int_0^r \alpha(r')dr'$, yielding the optical path $\tau(r)$ until height r, it is important to note that — looking at the graphs of Figure 6.3 —, the largest differences between different aerosol models come from low heights where the aerosol layer is expected to be located. The strong gradient of all curves at lower heights indicate that the largest differences from height-to-height bin can be found at these heights, whereas at the last chosen height bins (in correspondence with the range of the Ceilometer) for all IHAZE aerosol models used in the graph, the very last extinction values are actually all the same ($\sim 3 \times 10^{-6}$ m^{-1}), with the differences only being remants of the integrated differences at lower heights.

6.6.2 Height correction

The usual way to display a sky profile of backscatter is return power P multiplied by squared distance (e.g. shown in equation 6.3), as the mere geometrical electromagnetic extinction over the squared distance is usually of no interest in LIDAR studies.

The Ceilometer supports two modes of manipulation of the user-accessable backscatter data (but that does not change internal calculations, e.g. the cloud detection algorithm) [Vaisala, priv.comm.]:

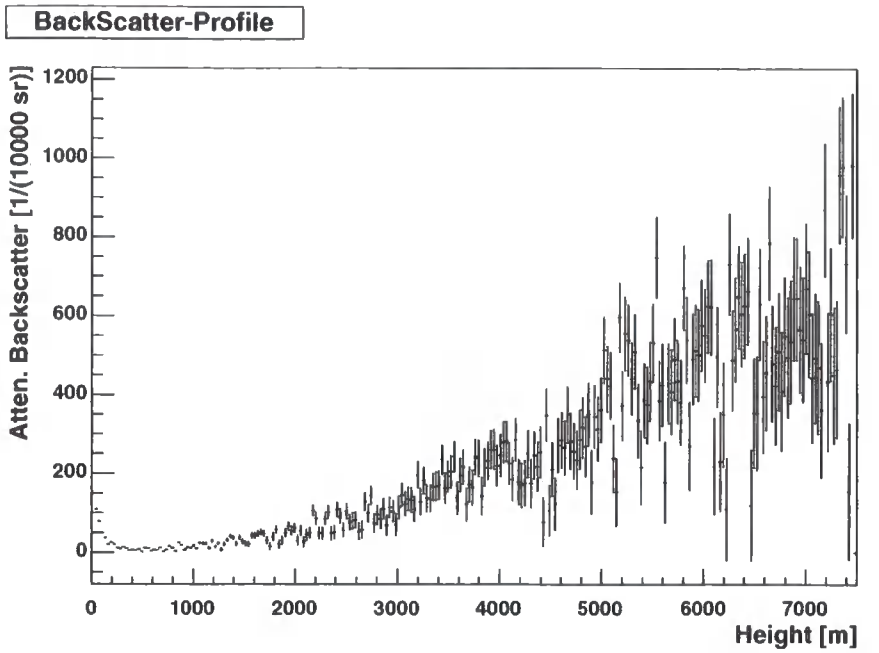

Figure 6.4: Sky profile of attenuated backscatter from May, the 10th, 2003, with height-correction switched on. This was a very clear day, as can be seen in the next graph. Note the increased artificial signal at heights greater than approx. 1000 m due to amplified noise.

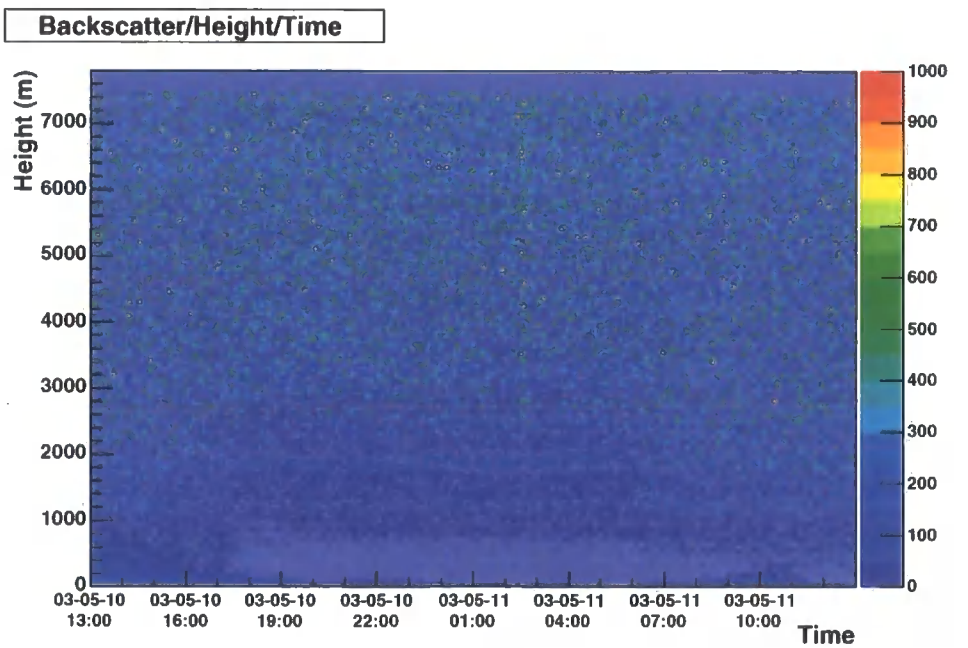

Figure 6.5: 2-dim atten. backscatter profile vs time and height from May, the 10th, 2003, with height-correction switched on. The backscatter (bs) values have been transformed for visual purposes using $bs \rightarrow 1000 \cdot \tanh(bs/1000)$ (as motivated by Holin et al. [2004]). This transformation ensures that occasional strong backscatter does not 'saturate' the graphs; that way the resolution in low backscatter regions is maintained. Note the wavy patterns during the night, when the sky was very clear. These patterns are presumably due to a fast-fourier cleaning (FFT) algorithm applied internally by the Ceilometer and out of our control.

1. Literature Standard, meaning it has been corrected by the squared distance. Disadvantage: If no backscatter signal can be detected, only noise will be scaled by the correction, resulting in a confusingly huge signal from greater heights.

2. Without height correction, resulting in a flat profile for greater heights in case of no detected backscatter. Disadvantage: If backscatter is detected, the Ceilometer strangely corrects in the height levels of and around to the detected backscatter (as controlled by the internal analysis electronics), but not up to the concerned height and as well not afterwards, resulting in a non-physical profile, that renders inversion algorithms to calculate a correct or meaningful transmission or optical depth impossible.

Although the height-corrected mode is the literature standard, Vaisala had decided to make the less noisy manipulation its default, for mere display resons. Even further, the manual neither mentions, that the height correction is performed in either cases up to the height of 1000m nor that the profile is only partly corrected in the noise-less mode [Vaisala, priv.comm.].

So, as the Ceilometer mainly was built with aerosol detection in urban areas and eye-safety in mind, the laser energy is so low, that no backscatter signal can be received from parcels of air as clean as above the observatory site in Namibia. As said before, if one would correct for the height in this low backscatter environment, all data is dominated by noise being scaled by the height correction as can be seen in figures 6.4 and 6.5, compared to the flat, not height-corrected, backscatter profile in figure 6.6.

6.7 Inversion attempts

During the early months of operation of the Ceilometer it was believed, that the Ceilometer data corresponds to backscatter values, not to attenuated backscatter values. These would be the results of an internal Klett inversion that is indeed happening during the internal data analysis for the cloud detection features of the Ceilometer. But the fact, that the actual 'raw' backscatter data are still attenuated backscatter data without the Klett inversion applied to it, remains to be found in the manual and only became known to us by private communications. In their defense, the reason why Vaisala decided to not apply the Klett inversion to

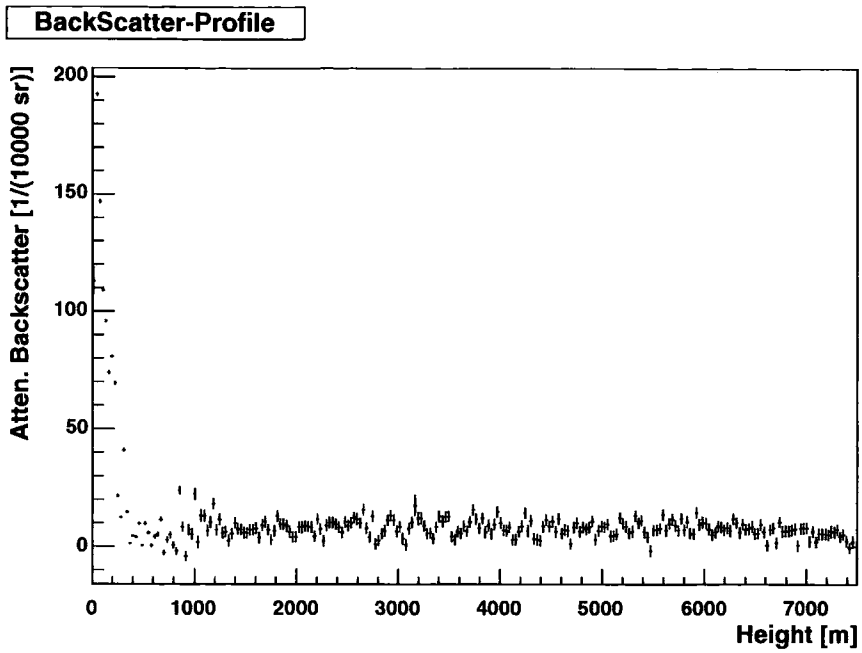

Figure 6.6: Sky profile of attenuated backscatter from May, the 26th, 2003, with height-correction switched off. This was a very clear day as well, not a single backscatter disturbance for 24 hours. Note that, due to the internal algorithms being confused by the too clear sky, the backscatter values just before 1000 m height scatter around zero, although this normally should be a region, where the signal-to-noise ratio is good enough to not confuse the measured data (which is why 1000 m is the limit up to Vaisala decided to height-correct any backscatter data). We can only presume, having no access to the physical return power values, that the laser power is just too low for these kind of perfect atmospheres (May until July have the clearest skies of all the year at the observatory site due to the local winter.

the user-accessable data is, according to private communication, 'because it is not scientifically unambiguous. It is, however, good enough to be the base for cloud detection.'

6.7.1 Strategy

Once it was realised, that a full Klett inversion could be tried with the Ceilometer data, though knowing that it will be difficult due to the low powered laser, considerable effort was spent to calculate physically meaningful transmission values, as these are the kind of data that would be implemented directly into the H.E.S.S. detector simulations, where atmospheric transmission tables are used to relate, e.g. the Hillas parameter *size* with an energy, according to zenith angle dependent simulated

transmission tables. Having input about the transmissive state of the atmosphere in parallel to observations could therefore be an invaluable tool to improve the energy resolution of the detector system.

As mentioned before, usually the 'seed' for a Klett inversion is taken from MODTRAN or other atmospheric simulations. However, because the laser signal is too weak to provide a good signal-to-noise ratio up to a height where the backscatter can safely be assumed to be dominated by Rayleigh scattering, the starting value for extinction from simulations is of no direct use for the height-corrected, noise-dominated data that were taken.

The next idea was to use the non-height-corrected mode of the Ceilometer to get rid of the noise for Klett inversions. Of course, now the signals after 1000 m, at least during clear nights, were merely fluctuations of the small electronic noise values, 'enriched' by an obvious FFT-cleaning, that is performed internally, indicated by wave-like patterns in the backscatter data on clear nights.

But part of the idea was to start a Klett inversion on the clearest nights one could find in the Ceilometer data, assuming that these days could serve as a lower limit of backscatter profiles, with the least amount of aerosols. The trick now would have been to perfom several Klett inversion on these clear days, using many different inital extinction values, and cross-calibrating the resulting transmissions over the height range of the Ceilometer with the transmission calculated by the MODTRAN simulation. That way it was thought to be possible to find an, albeit un-physical, starting extinction value. This value would be decades higher than the one calculated by MODTRAN, due to the too low power of the LIDAR laser, but hopefully at least stable over time and, more importantly, still valid on less clear nights.

The graphics of figure 6.7 summarises the (several weeks of) efforts that were spent on this idea. The procedure was also testing with different binnings as an attempt to reduce the impact of the fluctuations around zero presumably caused by the FFT-algorithm; negative values on the way down the sky profile (as can be seen in Figure 6.6) disturb quite significantly the way, the Klett integration proceeds. The dark line seen in the graphs is the Rayleigh scattering curve as calculated by MODTRAN for a 15° tropical profile without any aerosol attenuation. As one can see, the same level of optical depth and transmission can be matched with different extinction seed values, but obviously the shape of the optical depth profile is quite different to what one would expect. This is due to the lack of Rayleigh scattering, as this should create a shape similar to that in figure 6.8 (applying the proportionality-

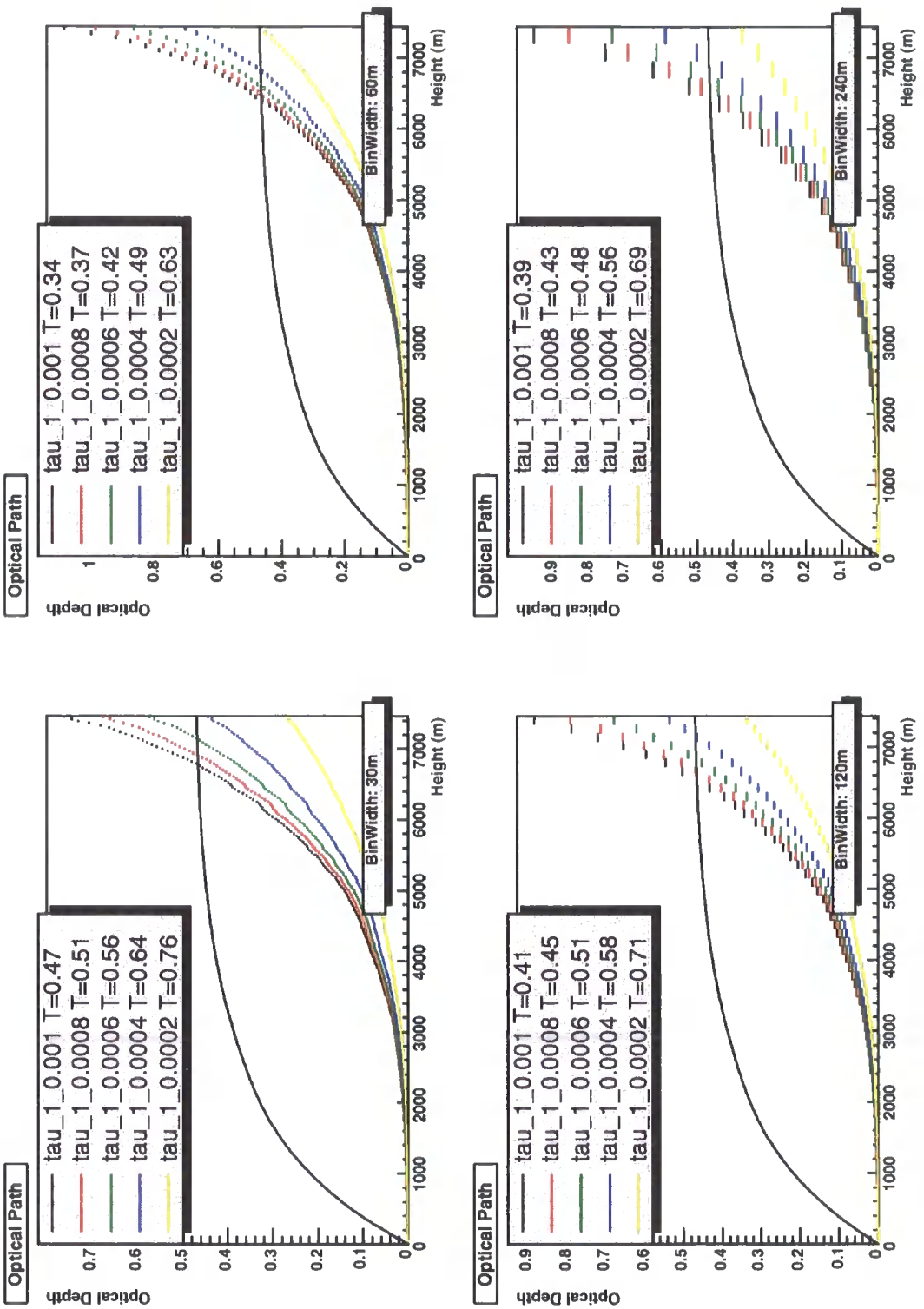

Figure 6.7: Graphic summarising the efforts to calculate optical depths and transmissions from the Ceilometer data. Please see text for details.

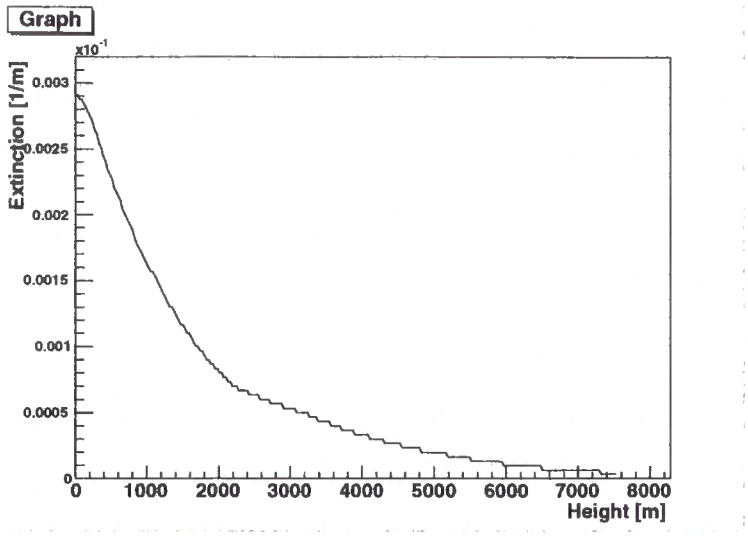

Figure 6.8: Extinction values calculated for each transmission value as given by MODTRAN for a 15° tropical north atmosphere without any aerosol attenuation (IHAZE=0)

assumption of Klett between the backscatter and the extinction).

Using this machine-dependent non-physical extinction 'seed' as a starting point for the Klett inversion, it might have been possible to calculate transmission values for the data on nights, where clearly absorption by aerosols occurs. However, after defining several machine-own α_f-values and trying to implement them on backscatter-rich data, no consistent behaviour could be found. Calculated time-profiles of transmission from Ceilometer data over days or weeks always break down into non-physical values, because the Klett inversion is corrupted by either too many negative values along the way of the integration down the sky or by a non-constant machine-dependent extinction seed, for which no relation to any environment parameter could be found. One has to note, regarding the former point, that one special feature of aerosol-laden lowered transmission events in the Namibian (or any desert sky for that matter) is the clarity at heights of the sky where no aerosols are located

It was tried to set negative values to zero, but this again renders unphysical results from the Klett inversion, when compared to MODTRAN simulations to find ranges of possible sky transmissions, using e.g. a high wind desert model. Also it was tried to start the Klett inversion in low height regions, where the signal-to-noise ratio seemed to be sufficient to generally cause a non-noise backscatter signal.

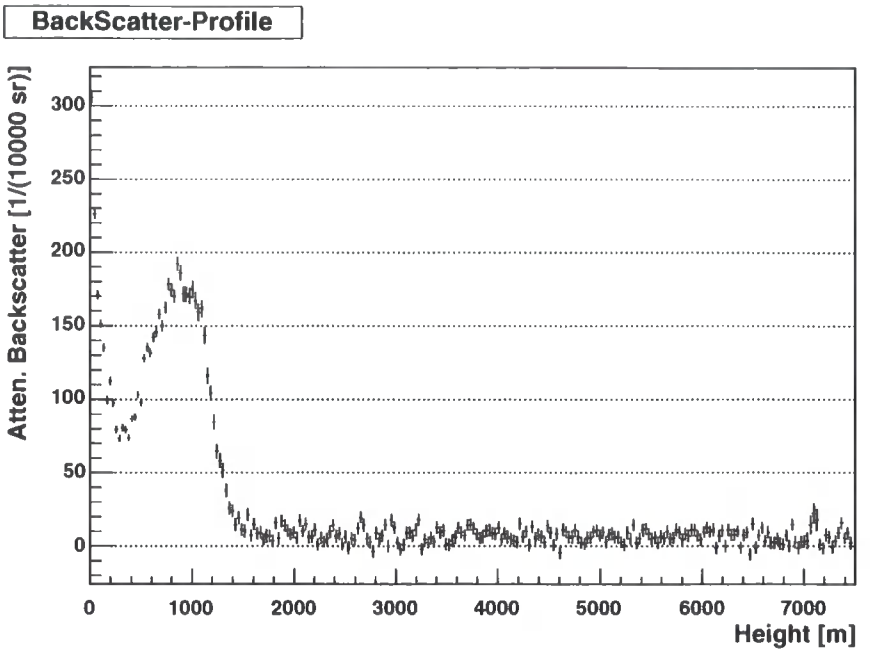

Figure 6.9: Backscatter profile from Septembter, the 6th, 2003. Note the flatness of signal above the aersol event. It prevents a proper Klett inversion, even though the overall transmission is significantly reduced by this dust cloud. Unfortunately, no observations were scheduled on this day.

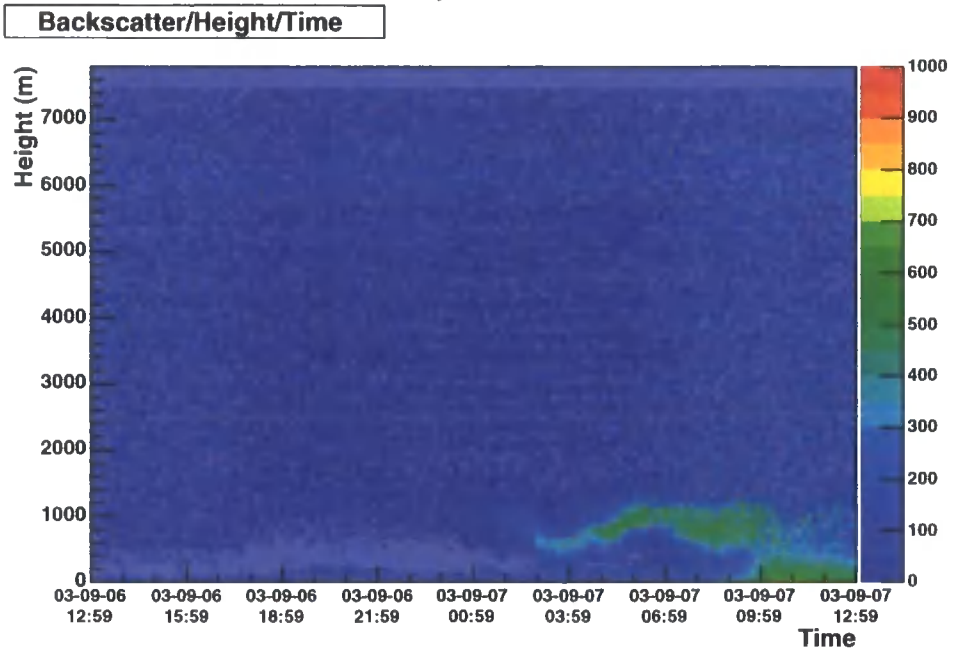

Figure 6.10: 2D backscatter profile from Septembter, the 6th, 2003.

However, aerosol layers have varying heights, therefore again no time-wise stability of relative transmission values could be achieved. These values would still have been only a relative indication of transmission and not an absolute one, because the scattering medium does not have to be the same at all times. Therefore using MODTRAN to calculate a seed value for the inversion becomes much more involved and needs further information about the dust distributions at the site to give a proficient extinction value at these lower heights (below 2 km), where the aerosol content can not be neglected.

As mentioned before, more monitoring devices are currently being commissioned to increase the knowledge about the scattering media, on days where the transmission is reduced by 'aerosol events' like that in Figure 6.10; these instruments include a dust distribution sampler and a transmissometer.

Currently, it has to be said, that it seems impossible to determine physical transmission or optical depth values with the Ceilometer[2].

Concluding, one should mention, that still the Ceilometer remains a valuable source of information concerning correlations of the mere raw attenuated backscatter data with the telescope cosmic ray trigger rate, a widely used independent means to evaluate the sky quality. The next chapter will now talk about preliminary results from these correlation studies using, amongst others, the integrated backscatter up to the trustworthy height of 1 km as a measure of aerosol content.

[2]Although the author has one more idea to increase the usability of the Ceilometer, see the Discussion chapter

Chapter 7

Data analysis

This chapter shows some of the results achieved by studying correlations between different atmosphere parameters themselves, but also in comparison with telescope trigger rates.

7.1 Attenuation event

During a multi-wavelength campaign in August 2004 (the H.E.S.S. observation period P2004-08) PKS 2155–304 , a blazar at redshift z=0.117, was observed; this source was first discovered in VHE γ-rays by the Durham group [Chadwick et al., 1999] and has been verified by H.E.S.S. [Aharonian et al., 2005]. Starting at around the middle of the observation period, significant changes in the sky quality (visible by eye during day and night through reduced visibility) had a remarkable impact on the observed cosmic ray trigger rates.

Multi-wavelength campaigns are especially important to study wavelength-dependent energy distributions in the observed fluxes to determine which processes contribute how much to the bolometric luminosity of the observed object. In the case of PKS 2155–304 expected source variability over time makes it especially important to know quantitatively how much, especially non-constant, attenuation of Cherenkov light takes place, and how much this reduces the sensitivity of the detector. For this reason, the data from this campaign has been chosen to serve as an example of current efforts to combine data from all available monitoring devices to study the correlations between atmospheric parameters with telescope data. Another advantage of starting such studies with an object having coordinates like PKS 2155-304 is the complete zenith angle coverage when observed by H.E.S.S. (23°S) which helps

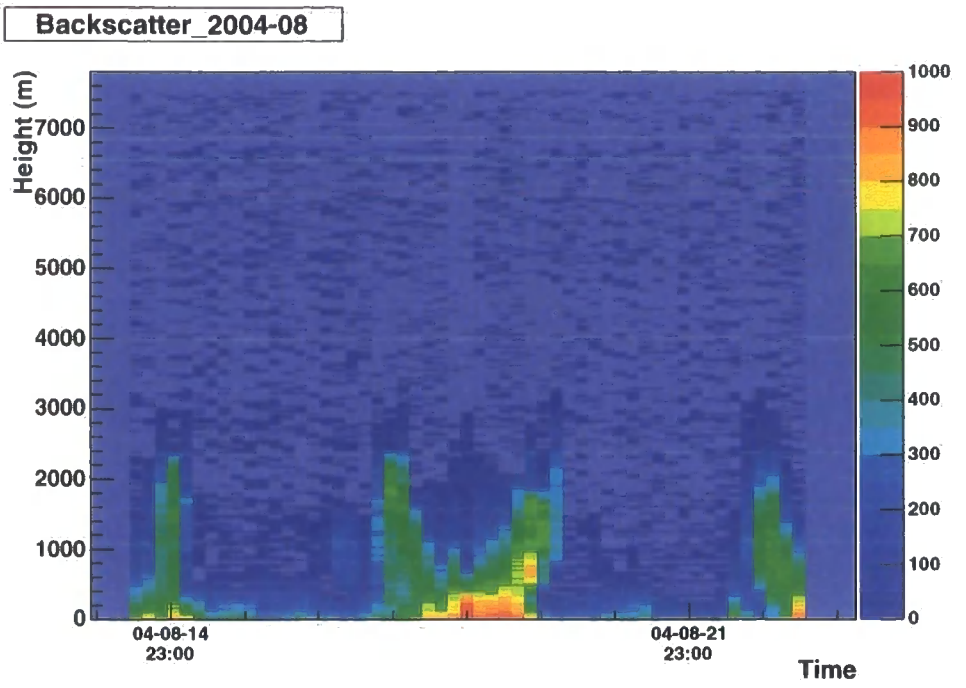

Figure 7.1: Backscatter over height and time for one week during the multi-wavelength campaign of PKS 2155–304 in the H.E.S.S. period P2004-08. Note the remarkable fast changes from large values of backscatter to very low values within one day after several days of reduced sky quality. As August is local winter at the observatory, the general quality (without temporal disturbances) is very high, therefore the days with good quality show some of the lowest backscatter values of the year! (This data is the combination of sequential 24 hour data runs)

the fitting procedures for data cleaning.

Two remarkable facts about the desert winter sky are that, firstly, the quality can change very quickly from very clear to heavily attenuating by temporarily intercepting layers of aerosols, and secondly, that even when at some heights strong attenuation occurs, other heights could be so clear, that the Ceilometer creates again noisy FFT-cleaned wavy patterns; in other words, disturbances are always well separated in time and space during the clear winter nights. This pattern changes during the summer time, when the sky can sometimes stay 'murky' for several days. The fact that very clean intervals are interspersed even amongst the attenuation event does help the correlation studies (see section 7.1.1).

Note that the internal Ceilometer analysis is specialised for estimates on backscatter values 'behind' layers of strong attenuation (a standard analysis problem of LIDAR data), as it has been built especially for reliable cloud height detection

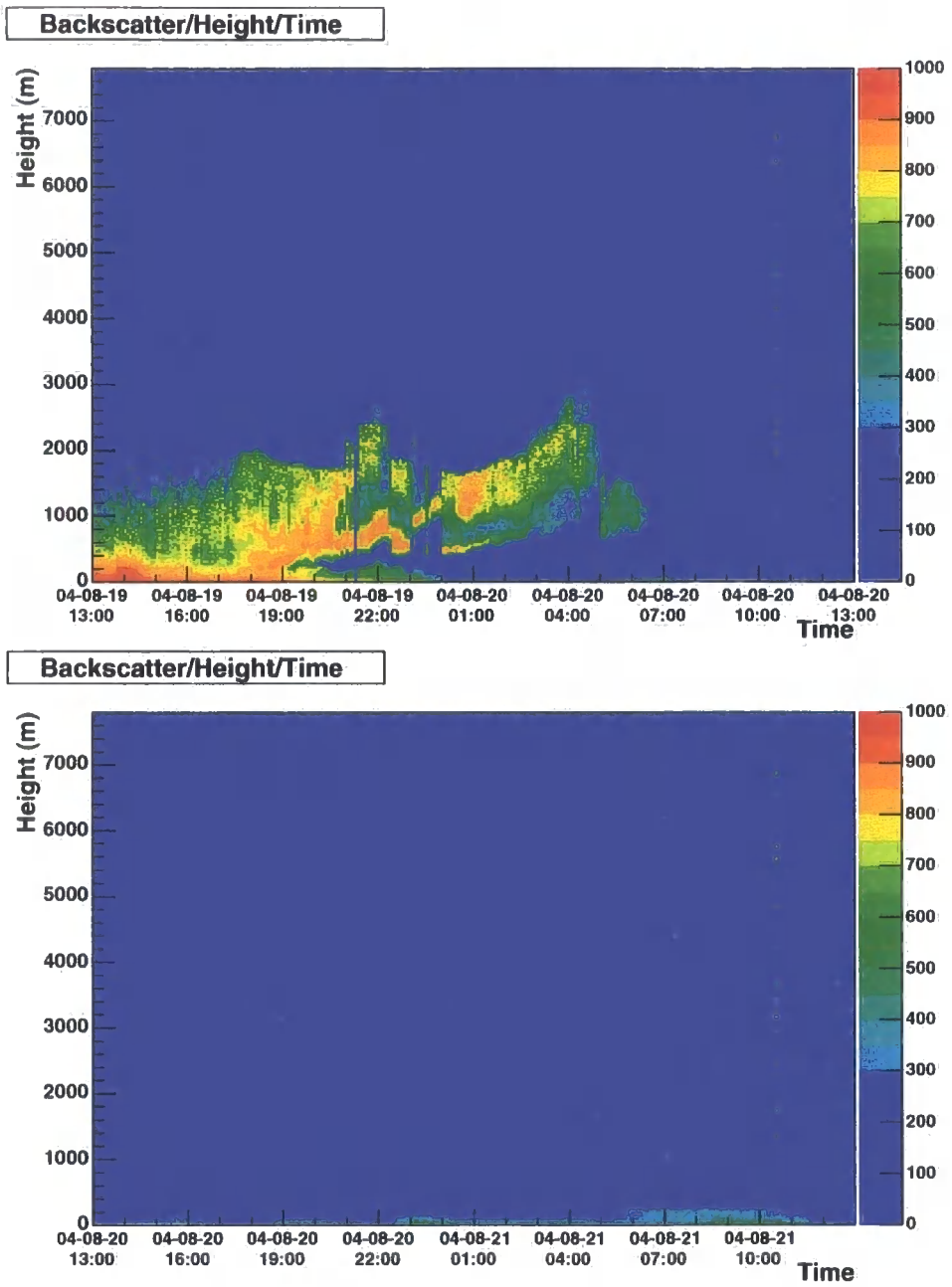

Figure 7.2: 24 hours of backscatter (colour) data vs height vs time for days 2004-08-19 and -20. The visible vertical slicing is produced by changes in the tilt angle (observing zenith-angle) of the Ceilometer when it is being repointed towards a different source. Different zenith angles correspond to different sample depths and most probably to a different height distribution of the current aerosol disturbance. During the night, the Ceilometer is under the same run-control as the telescopes; after astronomical dawn the Ceilometer returns back to constant zenith observation.

and visibility measurements on airports. How exactly this is achieved remains unknown because of the Ceilometer's commercially protected algorithms. However, it is known that only one constant of proportionality of the undetermined backscatter-to-extinction ratio is assumed, and that the resulting calculated extinction profile is evaluated whether it represents a cloud or not (private communication with Vaisala). Figure 7.1 shows how fast days of good and bad sky quality can change within a few days. Figure 7.2 shows these changes within two subsequent days and within these days even on timescales of hours.

Aerosol cloud layer definition

Figures 7.3 and 7.4 show an (until now) unique incidence of sharpness of the layer definition of an aerosol cloud on day 2004-08-17; almost undermining the height resolution of 30 m, the cloud stops so abruptly in height, that first a hardware error was held responsible for this effect. But on a closer inspection, the structure of the cloud can be followed to greater heights, only at much lower backscatter values. It was then considered, that maybe the tanh-transformation (as mentioned in caption 6.5) enhances the visual appearances of this cut-off due to the strong gradient of the tanh-function at roughly half-point of the normalization parameter (1000 is used, the maximal transformed backscatter function values at cut-off height lie around 400, see 7.3). But comparison with plots of un-transformed backscatter data show the same sharpness at the ridge of the aerosol cloud. Additionally, before and after this particular day, no other suspicious results were found, therefore it has to be concluded that this incidence is probably 'real' despite its digital appearance.

7.1.1 Preselected data-set

Data from clear nights with low Cherenkov light attenuation and therefore high cosmic ray trigger rates can be used to define reference values for atmospheric parameters, against which the nights with high attenuation can be measured. Because the atmospheric density profile changes during the year due to seasonal effects, the fact that the high-attenuation event has interspersed low attenuation intervals is especially useful to create a more comparable 'clean' data-set. Reference values from clean data sets of previous observation periods would have included a bias due to the seasonal differences in the averages of temperature, relative humidity, wind speeds and the consequently different density profile of the atmosphere (see below in this

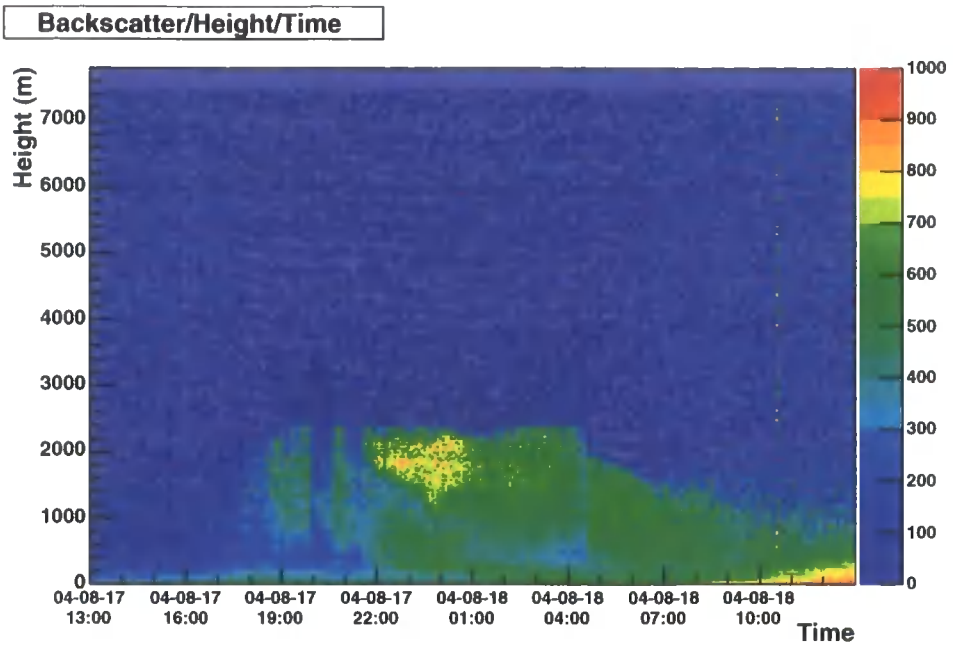

Figure 7.3: Backscatter over height and time for 2004-08-17. Remarkable here is the very abrupt stop of the aerosol layer, that first was believed to be a hardware failure. But on a closer inspection it can be seen that the aerosol cloud actually continues smoothly to greater heights, but with a much reduced backscatter value. Additionally, before and after this extraordinary signal, no other suspicious results were found from the Ceilometer, therefore this signal is probably real, provided no internal temporal weakness lead to this effect. See also picture below and more details in the text.

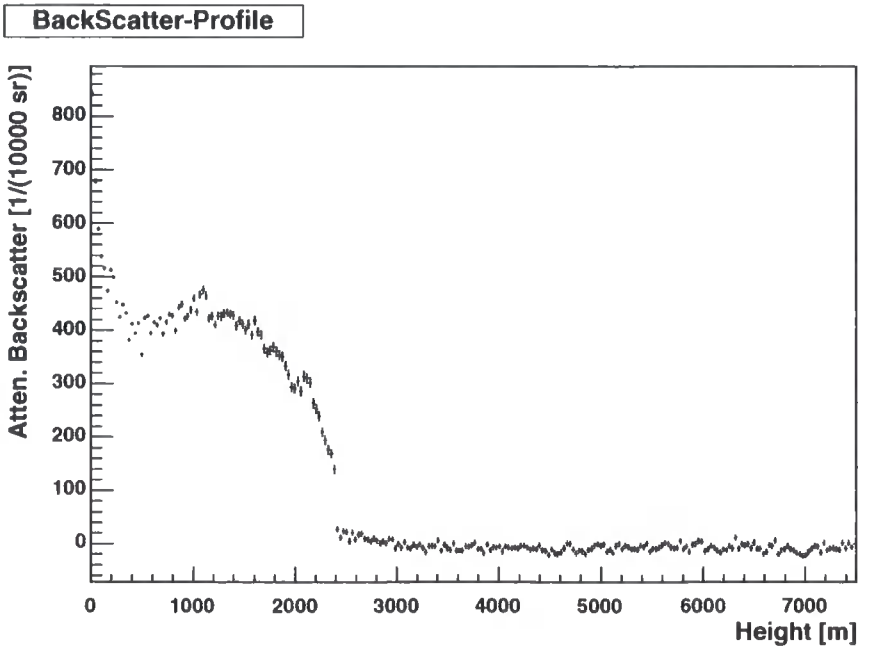

Figure 7.4: In this 24 hour average of the backscatter profile (a projection of the upper graph on the y-axis, the colour axis from above is now on the y-axis, not using the aforementioned tanh-transformation) the sharp edge that prevailed through several hours can be seen very clearly, although the temporal average smoothed it out.

section).

Standard methods for preselection of good data from clear nights include cutting on the standard deviation (SD) of radiometer temperatures to exclude any water vapour clouds in the field of view. However, relying purely on radiometer-SD cuts can fail when dealing with dust clouds in low humidity environments, because how the water vapour will react with prevalent dust to build larger globules with increased Mie scattering depends on the exact chemical properties of the aerosol. It can therefore happen that almost no change in radiometer temperature is seen, while the telescope trigger rate is reduced dramatically due to attenuation by dry dust clouds.

However, when looking at all PKS 2155-304 data of the August period, one can easily can make out different envelopes in the cosmic ray trigger rate vs zenith angle distribution, as shown in figure 7.5. A pre-cleaned dataset can now be created by loosely cutting around the upper envelope of this distribution.

Using the experiences gained by studying the zenith angle dependency with the scanning radiometer and 24 hour data, the question had to be answered how this would compare to observational run-data, taken only during the night. Figure 7.6 compares the power-sec-fit with the standard cos-fit that is usually applied to telescope trigger rate data to correct for the zenith-angle dependence. The power-sec shows a slightly better χ^2/ndf (number of degrees of freedom), but the difference seems only to be of relevance at higher zenith angles (emphasis on 'seems'!).

Now it has to be noted that, although profile histograms can be helpful to do standard averaging of repeated measurements, it implies a loss of information regarding the shape of the original distribution of values. Without looking at a graph of all values of trigger rates vs zenith angle it would not have been possible to recognize the envelopes of different distributions to construct a cleaned data set. Doing the same for the radiometer data, it was found that even with this already cleaned data set, there seems to be a residual lower limit envelope for the flux values (see Figure 7.7), with the fluxes sporadically fluctuating to higher values, presumably due to bubbles of warmer air. Obviously this doesn't mean that this could be directly related to fluctuations in the cosmic ray trigger rate (UV vs IR), but it seemed to be worthwhile to check how the rate vs zenith angle relation would change, if envelope cuts on radiometer fluxes would be introduced on an already cleaned data set.

Applying this radiometer flux cut by requiring that the measured flux value stays within 2.5% of the envelope function, the χ^2/ndf of the rate vs zenith angle

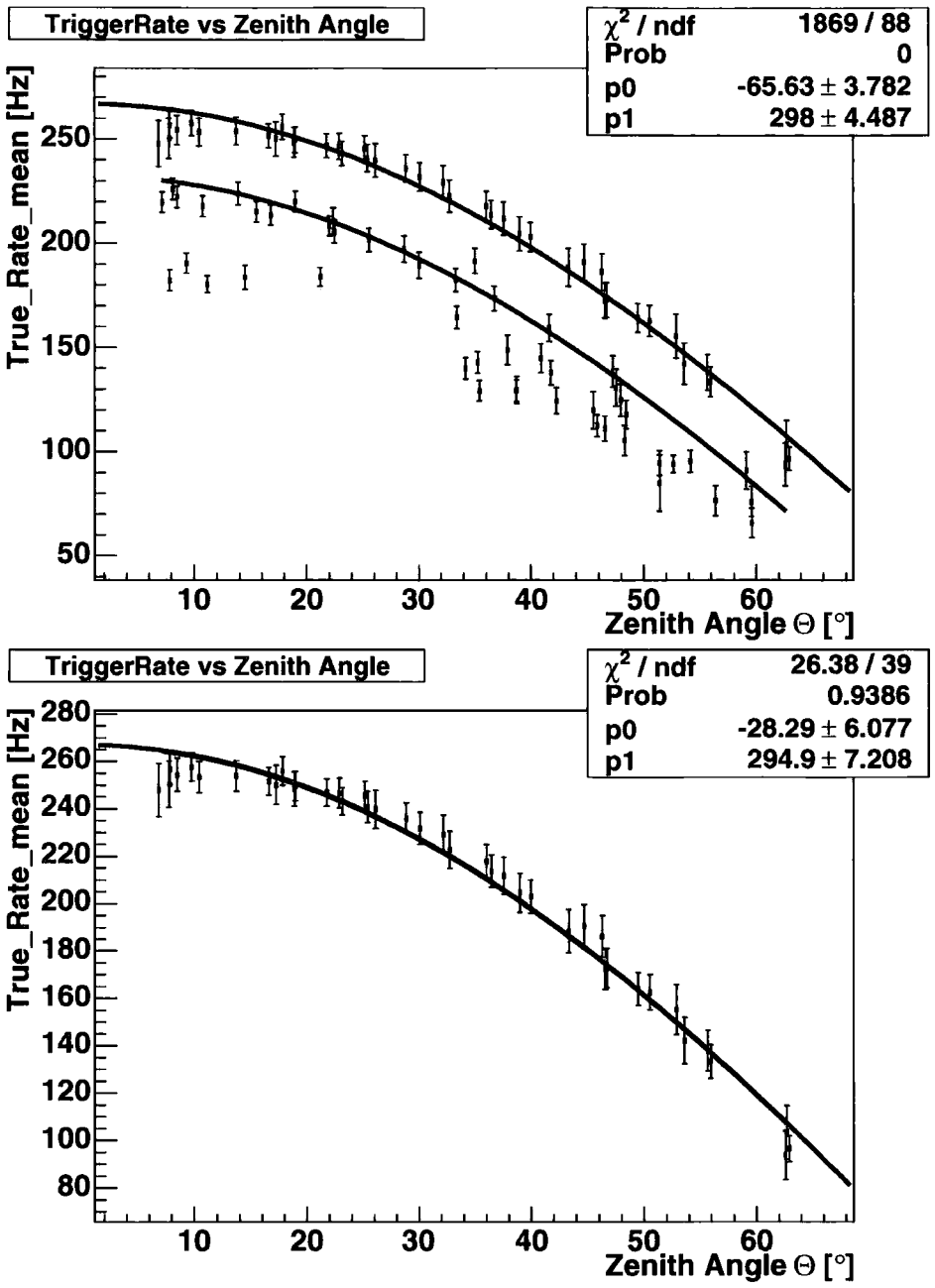

Figure 7.5: Telescope trigger rate vs mean zenith angle for all PKS 2155-304 observation runs in the period P2004-08. Vertical error bars are the standard deviation of the dead time corrected (therefore called 'true rate') telescope trigger rate over one run of the standard observation length of 28 min. Note the different populations resulting from totally different sky clarity states. The upper graph's fit is used as a pre-selective data-cut to create a cleaner training sample as shown in the lower graph.

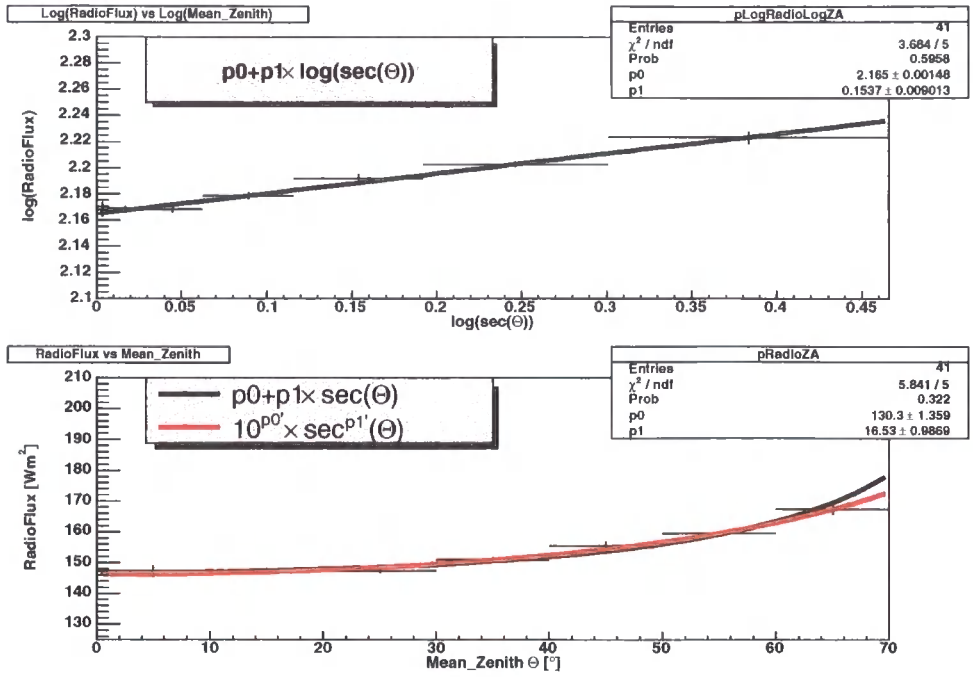

Figure 7.6: Upper graph: Profile histogram of the mean over the radiometer fluxes for the four telescope radiometers for the runs of the pre-cleaned data set. Bins are non-equidistant according to the weighting created by log(sec). The error in y is the error on the mean of the average radiometer flux over the particular log(sec(Θ)). Fitting is applied as described in sec. 5.4. Lower graph: The resulting parameters of the upper graph's fit are drawn in comparison with a standard sec-fit. Only the higher zenith angles show any relevant difference in the quality of the fit (more details in the text).

fit improved slightly (see Figure 7.8) from a corresponding probability of $\sim$ 93% to $\sim$ 98% by losing the lower trigger rate fluctuations that appeared at low zenith angles in Figure 7.5. Importantly, this was achieved without cutting harder on an ideal expectation on the rate vs zenith angle relationship, but by cutting on radiometer data, which yields therefore a 'blind' method for data cleaning by a second instrument. Using this radiometer cut might be a helpful tool in times where no clean data can be found in a set of data with a lot of fluctuation of trigger rates.

But as mentioned before, the application of radiometer cuts is not straightforward, because during the year the atmosphere layering and the average temperature of the lower atmosphere change, which will influence the radiometer data. This can be seen in figures 7.9 and 7.10. Whereas in July a new lower envelope function can

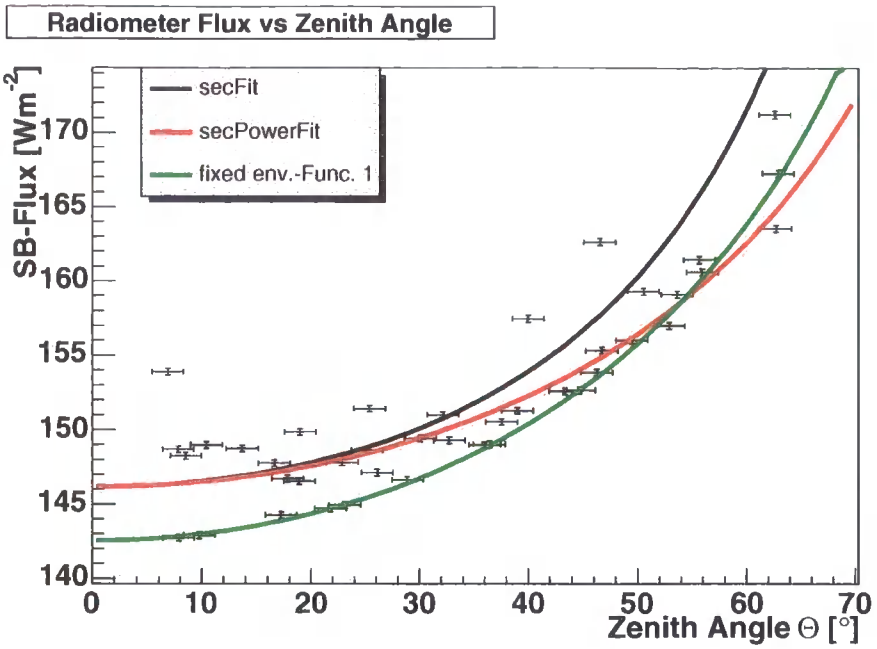

Figure 7.7: Scatter graph of radiometer fluxes for the cleaned PKS 2155-304 data set vs zenith angle. By not using a profile histogram the difference in the power-sec-fit and the standard sec-fit becomes more evident. However, this graph shows that a fit through averages of zenith angle bins makes no sense, because the distribution per zenith angle bin does not seem to be Gaussian, but instead cut off by a functional form well fitted with a standard sec-fit shown by the green curve. Note also, that the black coloured standard sec-fit through all the data is of the right shape and merely shifted straight upwards compared to the envelope fit, indicating that a sec-fit might eventually be the better choice for radiometer fluxes, reflecting more closely the optimum minimal zenith angle fluxes for the current season.

be found, in June, where the average temperatures are lowest, a population at higher radiometer fluxes seems to dominate. These effects are currently under study.

7.1.2 Corrected trigger rate vs Ceilometer

With the fit-function for the rate vs zenith angle relation, it is now possible to correct the trigger rate for the zenith angle change and compare this with the measured backscatter data from the Ceilometer. As mentioned before, it would have been optimal to compare trigger rates with optical depths calculated from the Ceilometer's data but without that, we still can study correlations between the trigger rate and the backscatter data itself.

As it has been described in chapter 6, data have been taken in two different

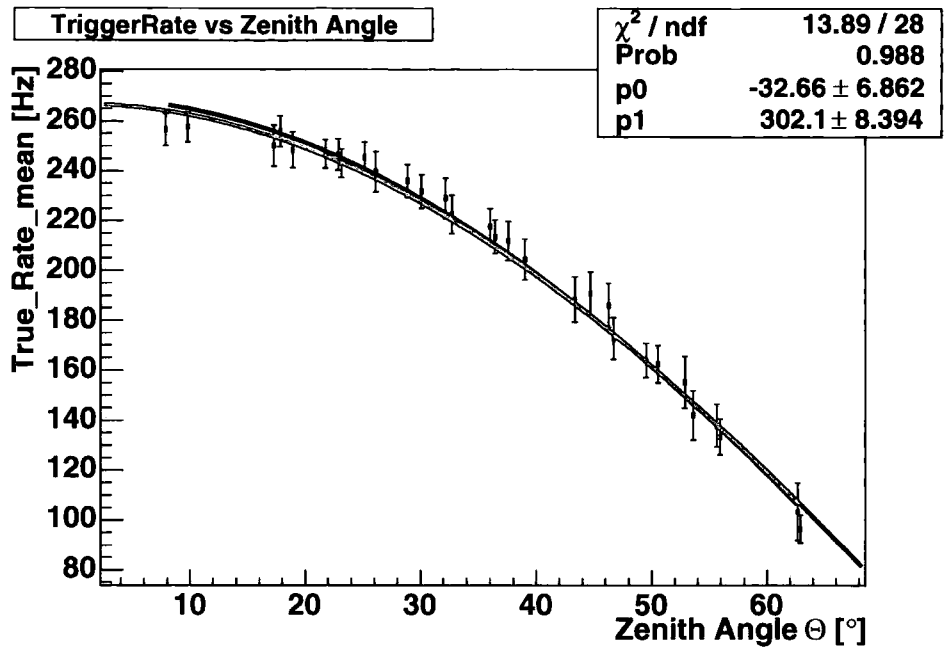

Figure 7.8: Dead time corrected true rate vs zenith angle. The green curve shows the fit-function before cutting the data set further by using the envelope function on radiometer fluxes. The resulting χ^2/ndf from this new fit improves slightly by losing the trigger rate reductions at low zenith angles that were apparent before the radiometer flux cut was used.

modes, one correcting for the $1/r^2$ reduction of backscatter signal but thereby mostly scaling up noise due to the very clear skies at the observatory site, and the other mode not correcting for the height, including the two problems that up to the height of 1000 m the data is still height-corrected, and above this height, the data is only height-corrected when the Ceilometer defines a signal as valid backscatter; even then only the data from the height bins where backscatter has been detected will be corrected.

These difficulties lead to the decision to use the integrated backscatter up to the height of 990 m (30 m bins!) as a main measure of the backscatter, because this value can be used disregarding the current observing mode of the Ceilometer, as the height correction will always be done. Correlating the zenith angle and dead time corrected telescope trigger rate with this Backscatter990-value is shown in figure 7.11. A general trend can be seen, but not clear enough to create any predictions from it. This is due to the fact that aerosol events often reach greater heights than 990 m. This part of the backscatter is of course missing in the correlation and explains the big scatter

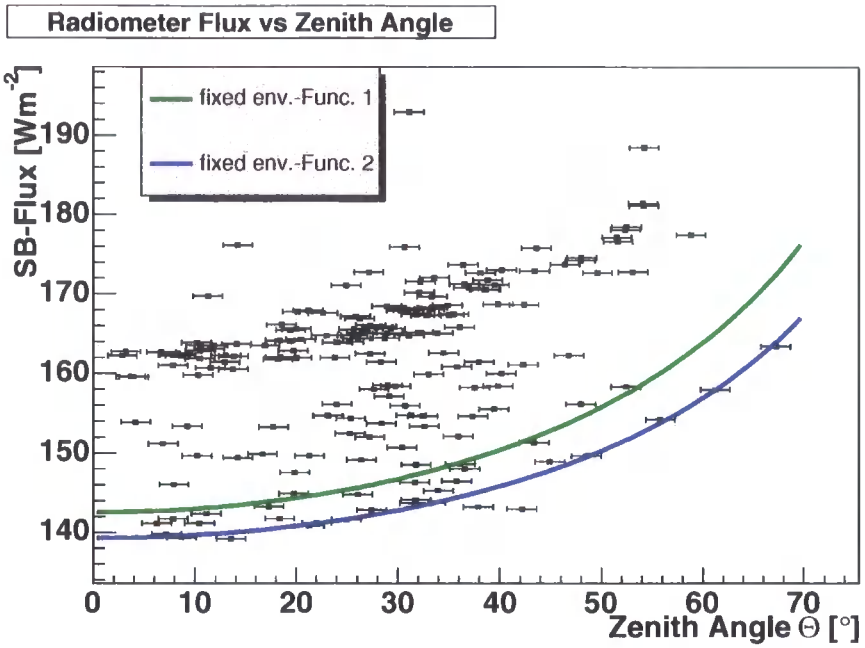

Figure 7.9: Radiometer flux distribution for all data taken in P2004-07. The green curve shows the radiometer envelope function for August, the blue curve shows the best lower envelope fit for this data of July. Because July is on average colder than August, the lower envelope can now be drawn at lower fluxes. Interestingly there is also indication of a reappearing upper envelope.

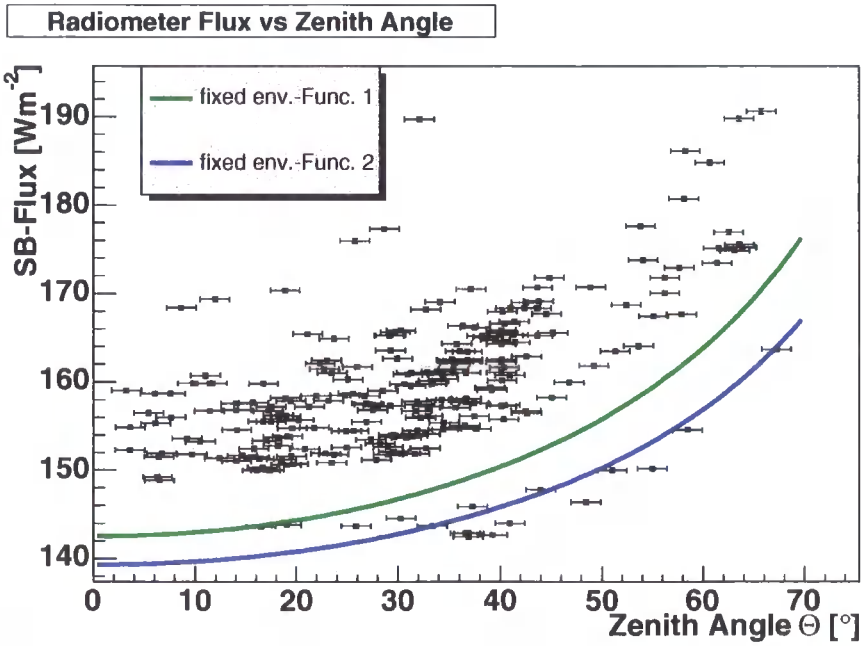

Figure 7.10: Radiometer flux distribution for all data taken in P2004-06. The green curve shows the radiometer envelope function for August, the blue curve shows the best lower envelope fit for this data of July. Here the situation is not so clear anymore. Although June's average screen level air temperature was colder than July and August (as it should be being the central winter month), the lower envelope seems to be the exception with a population at higher flux levels the rule. Correlation studies with data from the weather-station and the Ceilometer are underway.

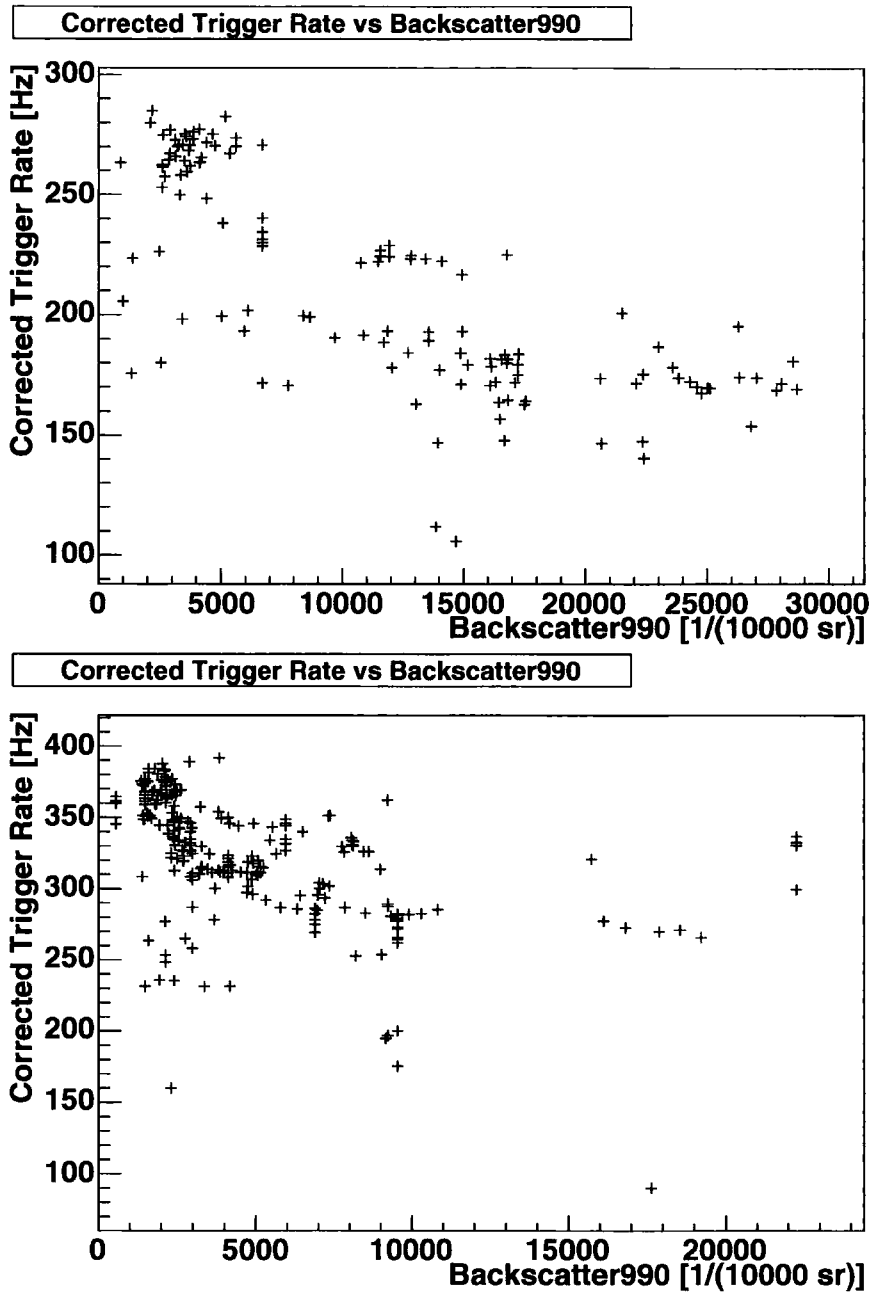

Figure 7.11: Correlation between zenith angle corrected telescope trigger rate and integrated backscatter up to 990 m. Upper graph: for all PKS 2155-304 data of observation period P2004-08. Lower graph: for all observations between April and July (incl.)

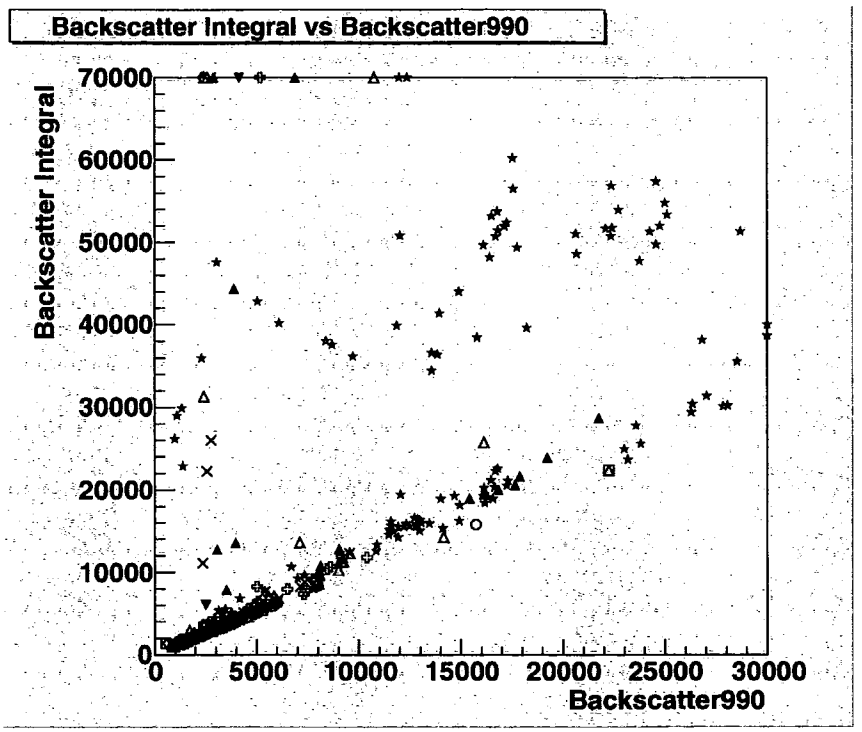

Figure 7.12: Correlation between the integrated backscatter up to the height where significant backscatter can be measured (different with every run) with the currently used backscatter990 value that only integrates up to 990 m. The correlation is good, unless the aerosol layer reaches greater heights than 990 m. At that point, backscatter990 can not increase anymore, but the flexible integral measures up to the point, where the backscatter signal becomes insignificant (Source: [Gallou, 2004]).

of the data. There is currently work in progress to change the analysis software, such that it can find the maximum height of significant backscatter and integrate this to a valid backscatter measure, so that all relevant parts of attenuating backscatter will be incorporated. This is possible because, as said before, the Ceilometer will height-correct above 1000 m in any observation mode, if significant backscatter occurs uninterrupted in height above the 1000 m limit. Preliminary results of this work can be seen in figure 7.12, correlating this new maximised backscatter integral with the currently used backscatter990. It becomes clear that, as long as the aerosol layer is within the integration limit of 990 m the correlation between these two values is very good, and as soon as the aerosol cloud reaches over that height (as in the case of the PKS 2155-304 data), the total backscatter value increases while the backscatter990 value can not increase anymore as already accounted for by its

integration. This work seems to be promising and will be continued until a better LIDAR system will be installed (see chapter 8).

Chapter 8

Discussion and future

8.1 Discussion

8.1.1 Flatfielding

The first target of this thesis project was the construction of a calibration light source for the flatfielding of the first H.E.S.S. telescope. The existing working designs of these kind of modules (short UV-laser pulse transported via optical fibre to a diffuser) had to be improved in terms of the distance over which the short light pulse had to be transported and in terms of remote controllability. This was first mainly a problem of finding the fibre cable providing the best compromise between light attenuation and pulse distortion. Being under time pressure of the construction schedule for the first H.E.S.S. telescope, because the fibres had to be integrated in the cable chains of the telescope that can not easily be opened once closed, it started to look like that, to achieve the required amount of light to illuminate the dynamic range of the H.E.S.S. camera, a huge compromise in pulse time width would be required. However, a better fibre cable was found, so that all design goals of the flatfielding module could be met.

The other main thing the author had to work on for this part of the thesis was the remote control of the whole module. For this, the author had the challenging but very worthwhile opportunity to gain knowledge about socket programming within computer networks.

Concluding regarding this first part of the thesis project, it can be said that, despite the fact, that the optical part of the system had been rendered obsolete quite soon after commissioning of the first H.E.S.S. telescope by the rapid development

in the market of UV LEDs, it was part of the early design definition to achieve operation fast and as good as possible, as it would have been a major impediment for the first telescope to be operated without a flatfielding light source. This target has been met and important knowledge gained from the early operation of the first telescope went directly into the development of the subsequent H.E.S.S. cameras.

8.2 Atmospheric monitoring and future activities

As with all hardware development during the commissioning of large international projects, often one's schedule has to succumb to other developments with higher priorities. So was the stable operation of the H.E.S.S. cameras an obvious priority that brought many changes in the design of the data acqusition. These changes in turn forced a constant watch and re-development of parts of the software framework of many parts of the atmospheric monitoring devices and development was often interrupted because important steps had to be done first by other parties being busy with higher priority work. In the first year of operation of the installed atmospheric monitoring devices, this resulted in a lot of data corruption, but eventually a sufficiently stable state was reached and all devices were being read out constantly and without much interruption.

A considerable effort has been spent by the author to generate a software framework for the analysis of data from the atmospheric monitoring devices that can be used by any member of the collaboration without knowing any details of the devices themselves. One of the last important achievements was software that is able to automatically generate data sets that combine all atmospheric monitoring and relevant telescope data for an observed astronomical object from the observation database with raw data not yet integrated in this database, performing the transition from run-related data to object-related time dependent data.

The weatherstation and radiometers provide excellent and flawless services, especially the radiometers once more have proven to be a valuable tool for data quality evaluation. Furthermore, as shown in chapter 7, after some further studies it will be possible to use the radiometer data for improved data cleaning. These studies should aim for the search of correlations between general atmosphere parameters like temperature and humidity and the position of the clearly visible envelope around the scattered plots of radiometer flux vs zenith angle. Exploring this further, more precise statements about the seasonal development of the atmosphere structure can

be made and could possibly lead to a best-envelope fit for each month, so that it becomes easier to evaluate the quality of observational data.

8.2.1 Ceilometer

The idea to purchase a rugged and fully designed LIDAR was well motivated by the ease of maintenance and reduced costs compared to flexible but fully controllable designs, let alone compared to the (manpower-)costs for developing a LIDAR system on our own. Also, compared to a LIDAR operating in the UV, a low-powered LIDAR operating in the IR has the advantage of firstly being eye-safe and, secondly, a camera-safe operation at all times, as the PMTs of the H.E.S.S. cameras are practically blind in the IR. This makes operation procedures very easy; the Ceilometer is simply in 24 hour operation. Compared to that UV LIDAR systems have to be carefully integrated into an observation schedule, as PMTs under high voltage can easily be destroyed by accidentally scattered UV laser radiation.

It was the goal to measure the transmission in the IR and use simulations from MODTRAN to extrapolate from these transmissions down to the UV region. But to achieve this, the power of the IR beam should have been high enough to excite Rayleigh scattering, otherwise a comparison with sky profiles from simulations becomes impossible, simply because no reliable transmission values could be created by the Klett inversion of the attenuated backscatter data.

Very frustrating was the fact that, only after many months of operation and subsequent questioning of the manufacturer about the exact physical nature of the raw data from the Ceilometer it was found out that this data was actually not being 'Klett-inverted' but still attenuated backscatter, a fact that contradicts statements of the manual.

The author's conclusion about the purchase of the Ceilometer as a LIDAR system would be, that it was definitely worth a try considering the up to a factor 4 reduced costs of purchase and ruggedness of the machine, fully designed for outdoor operation. Also the fact that all machine-related factors of the LIDAR equation have been dealt with internally is a great simplification in the analysis process. But at the end, the disadvantages of, first, having no control about the algorithms performed on the raw returned light power, and secondly, not sufficient laser power even at a wavelength far away from the really relevant UV wavelength regime reduce the scientific output of the Ceilometer to a minimum. The laser power is unfortunately too low to perfom the Klett inversion, also caused by the 'too-perfect' skies at the

site of the H.E.S.S. observatory. One tactic that still could be tried and only came as an idea during write-up of this thesis, is to define the Ceilometer data as pure aerosol data and assume that no Rayleigh at all is seen by it. Defining it that strictly would enable Rayleigh scattering profile to be taken from MODTRAN calculations and place it underneath the backscatter data from the Ceilometer data, so that the combined data might enable a stable Klett inversion. The author believes that this idea is very worthwhile to follow up.

On the other hand the Ceilometer has proven the usefulness of an aerosol detector, especially in the dry dusty areas that are otherwise ideal for the imaging atmospheric Cherenkov technique. It could be shown that aerosol events are easily detected with the Ceilometer and the data shows some correlation with the simultaneously greatly reduced telescope trigger rates of the H.E.S.S. telescope system. Also, the information about the position of aerosol layers provided by a simple system like ours is already used to improve the absorption tables from MODTRAN simulations and thereby calculate changes in the energy threshold of the detector system. Now that funding is available for a flexible LIDAR system in the UV, soon transmissions will be able to calculated directly for the relevant wavelengths in the UV, greatly reducing the efforts needed by extrapolations via atmospheric simulations.

Bibliography

F. Aharonian, A. Akhperjanian, M. Beilicke, K. Bernlöhr, H. Börst, H. Bojahr, O. Bolz, T. Coarasa, J. Contreras, J. Cortina, S. Denninghoff, V. Fonseca, M. Girma, N. Götting, G. Heinzelmann, G. Hermann, A. Heusler, W. Hofmann, D. Horns, I. Jung, R. Kankanyan, M. Kestel, J. Kettler, A. Kohnle, A. Konopelko, H. Kornmeyer, D. Kranich, H. Krawczynski, H. Lampeitl, M. Lopez, E. Lorenz, F. Lucarelli, N. Magnussen, O. Mang, H. Meyer, M. Milite, R. Mirzoyan, A. Moralejo, E. Ona, M. Panter, A. Plyasheshnikov, J. Prahl, G. Pühlhofer, G. Rauterberg, R. Reyes, W. Rhode, J. Ripken, A. Röhring, G. P. Rowell, V. Sahakian, M. Samorski, M. Schilling, F. Schröder, M. Siems, D. Sobzynska, W. Stamm, M. Tluczykont, H. J. Völk, C. A. Wiedner, W. Wittek, Y. Uchiyama, T. Takahashi, and HEGRA Collaboration.
An unidentified TeV source in the vicinity of Cygnus OB2.
Astropart. Phys., 393:L37–L40, October 2002.

F. Aharonian, A. G. Akhperjanian, K.-M. Aye, A. R. Bazer-Bachi, M. Beilicke, W. Benbow, D. Berge, P. Berghaus, K. Bernlöhr, O. Bolz, C. Boisson, C. Borgmeier, F. Breitling, A. M. Brown, J. Bussons Gordo, P. M. Chadwick, V. R. Chitnis, L.-M. Chounet, R. Cornils, L. Costamante, B. Degrange, A. Djannati-Ataï, L. O. Drury, T. Ergin, P. Espigat, F. Feinstein, P. Fleury, G. Fontaine, S. Funk, Y. A. Gallant, B. Giebels, S. Gillessen, P. Goret, J. Guy, C. Hadjichristidis, M. Hauser, G. Heinzelmann, G. Henri, G. Hermann, J. A. Hinton, W. Hofmann, M. Holleran, D. Horns, O. C. de Jager, Jung I., B. Khélifi, N. Komin, A. Konopelko, I. J. Latham, R. Le Gallou, M. Lemoine, A. Lemière, N. Leroy, T. Lohse, A. Marcowith, C. Masterson, T. J. L. McComb, M. de Naurois, S. J. Nolan, A. Noutsos, K. J. Orford, J. L. Osborne, M. Ouchrif, M. Panter, G. Pelletier, S. Pita, M. Pohl, G. Pühlhofer, M. Punch, B. C. Raubenheimer, M. Raue, J. Raux, S. M. Rayner, I. Redondo, A. Reimer, O. Reimer, J. Ripken, M. Rivoal,

L. Rob, L. Rolland, G. Rowell, V. Sahakian, L. Saugé, S. Schlenker, R. Schlickeiser, C. Schuster, U. Schwanke, M. Siewert, H. Sol, R. Steenkamp, C. Stegmann, J.-P. Tavernet, C. G. Théoret, M. Tluczykont, D. J. van der Walt, G. Vasileiadis, P. Vincent, B. Visser, H. J. Völk, and S. J. Wagner.
H.E.S.S. observations of PKS 2155-304.
Astronomy & Astrophysics, 430:865–875, February 2005.

F. A. Aharonian and A. M. Atoyan.
A model of pulsed gamma radiation from the X-ray binary Hercules X-1/HZ Herculis.
Ap. J., 381:220, 1991.

F. A. Aharonian et al.
The temporal characteristics of the TeV gamma-radiation from Mkn 501 in 1997.
Astronomy & Astrophysics, 342:69–86, 1999.

F. A. Aharonian, A. K. Konopelko, H. J. Völk, and H. Quintana.
5@5 - a 5 GeV energy threshold array of imaging atmospheric Cherenkov telescopes at 5 km altitude.
Astroparticle Physics, 15:335–356, August 2001.

F. A. Aharonian and the H.E.S.S. collaboration.
Calibration of cameras of the H.E.S.S. detector.
Astroparticle Physics, 22(2):109–125, November 2004a.

F. A. Aharonian and the H.E.S.S. collaboration.
High energy particle acceleration in the shell of a supernova remnant.
Nature, 432:75–77, 2004b.

F. A. Aharonian and the H.E.S.S. collaboration.
Very high energy gamma rays from the direction of Sagittarius A*.
Astronomy & Astrophysics, 425:L13–L17, 2004c.

K.-M. Aye et al.
A novel alternative to UV-lasers used in flat-fielding VHE γ-ray telescopes.
In *Proc. 28th Int. Cosmic Ray Conference*, pages 2975–2978, 2003.

M. Beilicke and the H.E.S.S. collaboration.

Discovery of an unidentified Tev source in the field of view of PSR B1259-63 with H.E.S.S.
In *2nd Int. Symp. on High Energy Gamma Ray Astronomy.* APS Conf. Proc., 2004.

A. Berk, L. S. Bernstein, and D. C. Robertson.
MODTRAN: A moderate resolution model for LOWTRAN.
Space Science Instrumentation, July 1987.

K. Bernlöhr, O. Carrol, R. Cornils, S. Elfahem, P. Espigat, S. Gillessen, G. Heinzelmann, G. Hermann, W. Hofmann, D. Horns, I. Jung, R. Kankanyan, A. Katona, B. Khelifi, H. Krawczynski, M. Panter, M. Punch, S. Rayner, G. Rowell, M. Tluczykont, and R. van Staa.
The optical system of the H.E.S.S. imaging atmospheric Cherenkov telescopes. Part I: layout and components of the system.
Astroparticle Physics, 20:111–128, November 2003.

Konrad Bernlöhr.
Impact of atmospheric parameters on the atmospheric Cherenkov technique.
Astroparticle Physics, 12:255–268, 2000.

Bicron Organics.
`http://www.detectors.saint-gobain.com/Media/Documents/S0000000000000000003/p%dsbc418_420_422.pdf`, 2003.
accessed 13/09/2004.

P. L. Biermann.
The cosmic ray spectrum between 10^4 GeV and 3 x 10^9 GeV.
Astronomy & Astrophysics, 271:649, 1993.

C. Borgmeier et al.
The central data acquisition system of the H.E.S.S. telescope system.
In *Proc. 28th Int. Cosmic Ray Conference*, pages 2891–2894, 2003.

Buckley et al.
Measurement of sky clarity using MIR radiometers as an adjunct to atmospheric Cerenkov radiation measurements.
Experimental Astronomy, 9:237–249, 1999.

Campbell Scientific.
`http://www.campbellsci.com/wstatns.html`, 2003.
accessed 01/08/2003.

M. F. Cawley, D. J. Fegan, K. Harris, P. W. Kwok, A. M. Hillas, R. C. Lamb, M. J. Lang, D. A. Lewis, D. Macomb, P. T. Reynolds, D. J. Schmid, G. Vacanti, and T. C. Weekes.
A high resolution imaging detector for TeV gamma-ray astronomy.
Experimental Astronomy, 1:173–193, 1990.

P. M. Chadwick, K. Lyons, T. J. L. McComb, K. J. Orford, J. L. Osborne, S. M. Rayner, S. E. Shaw, K. E. Turver, and G. J. Wieczorek.
Very High Energy Gamma Rays from PKS 2155-304.
Astrophysical Journal, 513:161–167, March 1999.

Philip A. Charles and Frederick D. Seward.
Exploring the X-ray Universe.
Cambridge University Press, 1995.

K. S. Cheng, C. Ho, and M. Ruderman.
Energetic radiation from rapidly spinning pulsars. I - Outer magnetosphere gaps. II - VELA and Crab.
Astrophysical Journal, 300:500–539, January 1986.

Petr Chylek.
Extinction and liquid water content of fogs.
J. Atmos. Sci., 35:296–300, 1978.

G. Cocconi.
An air shower telescope and the detection of 10^{12} eV photon sources.
In *Moscow Cosmic Ray Conference, Volume II: Extensive Air Showers and Cascades Process*, pages 309–+, 1960.

R. Cornils et al.
Mirror alignment and performance of the optical system of the H.E.S.S. imaging atmospheric Cherenkov telescopes.
In *Proc. 28th Int. Cosmic Ray Conference*, pages 2875–2878, 2003.

Michael Kevin Daniel.

The attenuation of atmospheric Cerenkov photons.
PhD thesis, University of Durham, September 2002.

J. K. Daugherty and A. K. Harding.
Polar CAP models of gamma-ray pulsars: Emision from single poles of nearly aligned rotators.
Astrophysical Journal, 429:325–330, July 1994.

J. M. Davies and E. S. Cotton.
Design of the quartermaster solar furnace.
Journal of Solar Energy, 1(2 and 3):16–22, 1957.

L. O'C. Drury, F. A. Aharonian, and H. J. Völk.
GeV/TeV gamma-ray emission from dense molecular clouds overtaken by supernova shells.
Astronomy & Astrophysics, 271:645, 1994.

W. Michael Farmer.
The Atmospheric Filter, Volume 1, Sources.
JCD Publishing, 2001a.

W. Michael Farmer.
The Atmospheric Filter, Volume 2, Effects.
JCD Publishing, 2001b.

David J. Fegan.
γ/hadron separation at TeV energies.
J. Phys. G: Nucl. Part. Phys., 23:1013–1060, 1997.

Enrico Fermi.
On the origin of the cosmic radiation.
Physical Review, 75:1169–1174, 1949.

A. Filipčič.
Scanning lidar based atmospheric monitoring for fluorescence detectors of cosmic showers.
Astroparticle Physics, 2003.

Juhan Frank, Andrew King, and Derek Raine.
Accretion Power in Astrophysics.

Cambridge Astrophysics Series. Cambridge University Press, second edition, 1992.

S. Funk, J. Hinton, G. Hermann, D. Berge, K. Bernlöhr, W. Hofmann, P. Nayman, F. Toussenel, and P. Vincent.
The Central Trigger System of the H.E.S.S. Telescope Array.
In *AIP Conf. Proc. 745: High Energy Gamma-Ray Astronomy*, pages 753–757, February 2005.

Roland Le Gallou, 2004.
Priv. comm.

S. Gillessen et al.
Arcsecond level pointing of the H.E.S.S. telescopes.
In *Proc. 28th Int. Cosmic Ray Conference*, pages 2899–2902, 2003.

G. M. Haller and B. A. Wooley.
SLAC-PUB-6402, 1993.

Carole Haswell.
Active Galaxies.
The Open University, 2002.

HEGRA Collaboration, A. Konopelko, M. Hemberger, F. Aharonian, A. Daum, W. Hofmann, C. Köhler, H. Krawczynski, H. J. Völk, A. Akhperjanian, J. Barrio, K. Bernlöhr, H. Bojahr, J. Contreras, J. Cortina, T. Deckers, S. Denninghoff, J. Fernandez, V. Fonseca, J. Gonzalez, V. Haustein, G. Heinzelmann, G. Hermann, M. Hess, A. Heusler, H. Hohl, I. Holl, D. Horns, R. Kankanian, M. Kestel, J. Kettler, O. Kirstein, H. Kornmayer, D. Kranich, H. Lampeitl, A. Lindner, E. Lorenz, N. Magnussen, H. Meyer, R. Mirzoyan, H. Möller, A. Moralejo, L. Padilla, M. Panter, D. Petry, R. Plaga, A. Plyasheshnikov, J. Prahl, C. Prosch, G. Pühlhofer, G. Rauterberg, W. Rhode, A. Röhring, V. Sahakian, M. Samorski, J. Sanchez, D. Schmele, F. Schroeder, W. Stamm, B. Wiebel-Sooth, C. A. Wiedner, M. Willmer, and H. Wirth.
Performance of the stereoscopic system of the HEGRA imaging air Čerenkov telescopes: Monte Carlo simulations and observations.
Astroparticle Physics, 10:275–289, May 1999.

W. Heitler.
Quantum Theory of Radiation.

Oxford: Clarendon Press, 3rd edition, 1954.

Heitronics.
Prospekt KT19 Serie, 2003.
pdf Document (German), accessed on 01/08/2003.

A. M. Hillas.
Differences between Gamma-Ray and Hadronic Showers.
Space Science Reviews, 75:17–30, January 1996.

A. M. Hillas, C. W. Akerlof, S. D. Biller, J. H. Buckley, D. A. Carter-Lewis, M. Catanese, M. F. Cawley, D. J. Fegan, J. P. Finley, J. A. Gaidos, F. Krennrich, R. C. Lamb, M. J. Lang, G. Mohanty, M. Punch, P. T. Reynolds, A. J. Rodgers, H. J. Rose, A. C. Rovero, M. S. Schubnell, G. H. Sembroski, G. Vacanti, T. C. Weekes, M. West, and J. Zweerink.
The Spectrum of TeV Gamma Rays from the Crab Nebula.
Ap. J., 503:744–+, August 1998.

J. A. Hinton.
The status of the H.E.S.S. project.
New Astron.Rev. 48 (2004) 331-337, 48:331–337, 2004.

Hubert Holin, Marcel Zephoris, Franck Lavie, and Janne Räsänen.
Mixing layer height determination by means of a modified ceilometer.
volume P4. American Meteorological Society Annual Meeting, January 2004.
Conference poster.

D. Horns, F. A. Aharonian, and L. Costamante.
TeV observations of H1426+428 with HEGRA.
New Astronomy Review, 48:387–390, April 2004.

S. B. Idso.
A set of equations for full spectrum and 8- to 14-μm thermal radiation from cloudless skies.
Water Resources Research, 17:295–304, 1981.

M. P. Kertzman and G. H. Sembroski.
Computer simulation methods for investigating the detection characteristics of TeV air Cherenkov telescopes.
Nucl. Instrum. Methods Phys. Res. A, 343:629–643, 1994.

B. Khélifi, N. Komin, T. Lohse, C. Masterson, S. Schlenker, F. Schmidt, U. Schwanke, C. Stegmann, and Hess Collaboration.
Search for TeV Emission from the Direction of the Vela and PSR B1706-44 Pulsars with the H.E.S.S. Experiment.
In *AIP Conf. Proc. 745: High Energy Gamma-Ray Astronomy*, pages 335–340, February 2005.

J. G. Kirk and R. O. Dendy.
Shock acceleration of cosmic rays - a critical review.
J. Phys. G: Nuclear Part. Phys., 27:1589–1595, 2001.

J. D. Klett.
Stable analytical inversion solution for processing lidar returns.
Applied Optics, 20(2):211, 1981.

J. D. Klett.
Lidar inversion with variable backscatter/extinction ratios.
Applied Optics, 24:1638–1643, 1985.

Andreas Koch and Antje Kohnle.
Quantum and collection efficiency measurments of the photonis xp2960 photomultipliers.
Internal H.E.S.S. note, Mar 2001.

H. Krawczynski, S. B. Hughes, D. Horan, F. Aharonian, M. F. Aller, H. Aller, P. Boltwood, J. Buckley, P. Coppi, G. Fossati, N. Götting, J. Holder, D. Horns, O. M. Kurtanidze, A. P. Marscher, M. Nikolashvili, R. A. Remillard, A. Sadun, and M. Schröder.
Multiwavelength Observations of Strong Flares from the TeV Blazar 1ES 1959+650.
Astrophysical Journal, 601:151–164, January 2004.

H. Krawczynski and the H.E.S.S. collaboration.
HESS - A System of Imaging Atmospheric Cherenkov Telescopes for Stereoscopic Air Shower Observations in the >50 GeV Energy Range.
Bulletin of the American Astronomical Society, 31:727–+, April 1999.

H. Kubo, A. Asahara, G. V. Bicknell, R. W. Clay, Y. Doi, P. G. Edwards, R. Enomoto, S. Gunji, S. Hara, T. Hara, T. Hattori, S. Hayashi, C. Itoh,

S. Kabuki, F. Kajino, H. Katagiri, A. Kawachi, T. Kifune, L. T. Ksenofontov, T. Kurihara, R. Kurosaka, J. Kushida, Y. Matsubara, Y. Miyashita, Y. Mizumoto, M. Mori, H. Moro, H. Muraishi, Y. Muraki, T. Naito, T. Nakase, D. Nishida, K. Nishijima, M. Ohishi, K. Okumura, J. R. Patterson, R. J. Protheroe, N. Sakamoto, K. Sakurazawa, D. L. Swaby, T. Tanimori, H. Tanimura, G. Thornton, F. Tokanai, K. Tsuchiya, T. Uchida, S. Watanabe, T. Yamaoka, S. Yanagita, T. Yoshida, and T. Yoshikoshi.
Status of the CANGAROO-III project.
New Astronomy Review, 48:323–329, April 2004.

A. Lemière and Hess Collaboration.
AGN Observations with HESS.
In *AIP Conf. Proc. 745: High Energy Gamma-Ray Astronomy*, pages 443–448, February 2005.

M. S. Longair.
High Energy Astrophysics Volume 1: Particles, photons and their detection.
Cambridge University Press, second edition, 1992.

Malcolm S. Longair.
High Energy Astrophysics Volume 2: Stars, the Galaxy and the Interstellar Medium.
Cambridge University Press, second edition, 1994.

C. Masterson, W. Benbow, S. Funk, S. Gillessen, and Hess Collaboration.
Observations of the Crab nebula with H.E.S.S.
In *AIP Conf. Proc. 745: High Energy Gamma-Ray Astronomy*, pages 617–621, February 2005.

R. Mirzoyan and E. Lorenz, December 1994.
and references therein.

Phillip Morrison.
Unknown title.
Nuovo Cimento, 7:858, 1958.

I. I. Neshpor, A. A. Stepanian, V. P. Fomin, S. A. Gerasimov, B. M. Vladimirskii, and I. L. Ziskin.
On the periodical very high energy gamma-ray emission from Cyg X-3.

Astrophysics and Space Science, 61:349–355, April 1979.

Sam J. Nolan.
Simulation Studies of the Imaging Atmospheric Cherenkov Technique using the Durham Mark 6 and H.E.S.S. Stand-Alone Telescopes.
PhD thesis, University of Durham, September 2002.

R. A. Ong.
Very high energy gamma-ray astronomy.
Physics Reports, 305:93–202, 1998.

Rene A. Ong.
The Status of VHE Astronomy.
astro-ph/0304336 v3, 2003.

Photonics.
Photonics Design & Applications Handbook, 2000.
Photonics Directory Book 3, ISSN 1044-1425.

Photonis.
`http://www.photonis.com/editeuronline/Photonis/PAGES/product_range/photomult%ipliers/photomultiplier_tubes.htm`, 2003.
accessed on 10/08/2003.

W. H. Press et al.
Numerical Recipes, chapter 4, page 105.
Cambridge University Press, 1986.
eq. 4.1.3.

I. Robson.
Active Galactic Nuclei.
Wilson-Praxis Publisher, 1996.

ROTSE.
Robotic optical transient search experiment, 2004.
URL `http://www.rotse.net/`.
URL for Namibian ROTSE telescope: `http://www.rotse.net/r3csta.html`, last accessed 17/09/2004.

Gavin Rowell, Hendrik Krawczynski, Werner Hofmann, and Michael Panter.
Test mesurements of H.E.S.S. mirrors ii.
Internal H.E.S.S. note, Sep 2000.

S. Schlenker, M. Beilicke, B. Khelifi, C. Masterson, M. de Naurois, L. Rolland, and Hess Collaboration.
Discovery of the Binary Pulsar PSR B1259-63 in VHE Gamma Rays.
In *AIP Conf. Proc. 745: High Energy Gamma-Ray Astronomy*, pages 341–346, February 2005.

Spectra Physics.
VSL-337ND-S Nitrogen Laser.
`http://www.spectra-physics.com/com/cda/product/detail/1,1055,11538,00.html`, 2001.
accessed 13/09/2004.

Ceilometer CT25K User's Guide.
Vaisala Oyj, 2000.
URL `http://www.vaisala.com`.

P. Vincent et al.
Performance of the H.E.S.S. cameras.
In *Proc. 28th Int. Cosmic Ray Conference*, pages 2887–2890, 2003.

H. J. Völk.
The nonthermal energy content and gamma ray emission of starburst galaxies and clusters of galaxies.
Space Science Reviews, 75:21, 1996.

T. C. Weekes.
Very high energy gamma ray astronomy.
Physics Reports, 160(1-2):1–121, March 1988.

T. C. Weekes.
Very High Energy Gamma-Ray Astronomy.
Institute of Physics Publishing, 2003.

T. C. Weekes, H. Badran, S. D. Biller, I. Bond, S. Bradbury, J. Buckley, D. Carter-Lewis, M. Catanese, S. Criswell, W. Cui, P. Dowkontt, C. Duke, D. J. Fegan,

J. Finley, L. Fortson, J. Gaidos, G. H. Gillanders, J. Grindlay, T. A. Hall, K. Harris, A. M. Hillas, P. Kaaret, M. Kertzman, D. Kieda, F. Krennrich, M. J. Lang, S. LeBohec, R. Lessard, J. Lloyd-Evans, J. Knapp, B. McKernan, J. McEnery, P. Moriarty, D. Muller, P. Ogden, R. Ong, D. Petry, J. Quinn, N. W. Reay, P. T. Reynolds, J. Rose, M. Salamon, G. Sembroski, R. Sidwell, P. Slane, N. Stanton, S. P. Swordy, V. V. Vassiliev, and S. P. Wakely.
VERITAS: the Very Energetic Radiation Imaging Telescope Array System.
Astroparticle Physics, 17:221–243, May 2002.